ABSTRACT

Title of dissertation: INVESTIGATION OF IRON-BASED AND TOPOLOGICAL SUPERCONDUCTORS VIA POINT-CONTACT SPECTROSCOPY

Steven Ziemak, Doctor of Philosophy, 2015

Dissertation directed by: Professor Johnpierre Paglione
Department of Physics

I report results of point-contact spectroscopy (PCS) measurements preformed on a variety of superconductors which are predicted to exhibit unconventional Cooper pairing mechanisms. Point-contact spectra of the iron pnictide $BaFe_{1-x}Pt_xAs_2$ are consistent with a two-gap isotropic s-wave model. This conclusion is supported by previously published results from thermal conductivity, angle-resolved photoemission spectroscopy (ARPES), and Raman spectroscopy, which confirm a lack of nodes in the order parameter and the presence of a gap of magnitude 3 meV. Conductivity spectra were also measured for the half-Heusler materials YPtBi and LuPdBi using the soft point contact method. I argue that the repeated observation of a single peak in dI/dV at zero bias is not consistent with a conventional s-wave model. Based on attempts to fit my data to the Blonder-Tinkham-Klapwijk theory and comparison to previous experimental and theoretical work, I conclude that my results are most consistent with a model of triplet Cooper pairs and an order parameter with an odd-parity component.

INVESTIGATION OF IRON-BASED AND TOPOLOGICAL SUPERCONDUCTORS VIA POINT-CONTACT SPECTROSCOPY

by

Steven Ziemak

Dissertation submitted to the Faculty of the Graduate School of the
University of Maryland, College Park in partial fulfillment
of the requirements for the degree of
Doctor of Philosophy
2015

Advisory Committee:
Professor Johnpierre Paglione, Chair/Advisor
Professor Richard Greene
Professor Ichiro Takeuchi
Professor Frederick Wellstood
Professor Steven Anlage

Foreword

The results of my work have contributed to the following published works, with the publications that have portions represented in this thesis indicated with an asterisk.

*Steven Ziemak, K. Kirshenbaum, S. R. Saha, R. Hu, J.-Ph. Reid, R. Gordon, L. Taillefer, D. Evtushinsky, S. Thirupathaiah, B. Büchner, S. V. Borisenko, A. Ignatov, D. Kolchmeyer, G. Blumberg, and J. Paglione, **Isotropic multi-gap superconductivity in $BaFe_{1.9}Pt_{0.1}As_2$ from thermal transport and spectroscopic measurements**. Superconductor Science and Technology **28**, 014004 (2014).

Xiaohang Zhang, N. P. Butch, P. Syers, S. Ziemak, Richard L. Greene, and Johnpierre Paglione, **Hybridization, Inter-Ion Correlation, and Surface States in the Kondo Insulator SmB_6**. Physical Review X **3**, 011011 (2013).

Kevin Kirshenbaum, S. R. Saha, S. Ziemak, T. Drye, and J. Paglione, **Universal pair-breaking in transition-metal-substituted iron-pnictide superconductors**. Physical Review B **86**, 140505 (2012).

S. R. Saha, N. P. Butch, T. Drye, J. Magill, S. Ziemak, K. Kirshenbaum, P. Y. Zavalij, J. W. Lynn, and J. Paglione, **Structural collapse and superconductivity in rare-earth-doped $CaFe_2As_2$**. Physical Review B **85**, 024525 (2012).

The results presented in Chapter 5 are currently in the pre-publication stage and will likely be submitted for publication soon pending other experimental results.

Dedication

To JP for showing me the way, and to Cait for her endless support, patience, and encouragement.

Acknowledgments

This thesis is the result of a massive collaboration that has taken place over the course of the last five-plus years. It was completed with the assistance of dozens of colleagues not just at the University of Maryland, but at universities and institutions around the world. I would like to take a moment to thank everyone who helped make this work a reality.

First, I'd like to thank my advisor Johnpierre Paglione, who has guided me through the whole process. As a fellow graduate of an Engineering Physics program, JP sought me out and invited me to work with his group before I'd even finished my undergraduate degree. I am grateful to him for giving me the opportunity to work in such an interesting field and for generally being a great advisor to work for.

Next, I'd like to acknowledge all of the current and former postdoctoral researchers and research scientists who have helped me throughout the years. I would especially like to thank Xiaohang Zhang for teaching me almost everything I know about the point-contact spectroscopy technique. From preparing samples to performing measurements and analyzing data, he helped me out every step of the way. Xiaohang was also responsible, along with Dr. Richard Greene and the rest of his research group, for building the needle-anvil point-contact probes and Labview programs that I have used in my research. Their hard work truly laid the foundation for my work, and these contributions are greatly appreciated. I'd also like to thank Shanta Saha, Kui Jin, Rongwei Hu, Xiangfeng Wang, and Yeping Jiang for their assistance with my experiments.

I would also like to acknowledge the contributions of Professors Richard Greene and Ichiro Takeuchi for their valuable discussions on my results, as well as the CNAM technical staff, Brian Straughn and Doug Benson, for keeping our labs running smoothly.

I have also had the pleasure of working with some very talented graduate students who have helped me along the way: Kevin Kirshenbaum, Tyler Drye, Paul Syers, Richard Suchoski, and more recently, Renxiong Wang and Connor Roncaioli. I'd like to thank all of them for their support and assistance in the lab, to congratulate those of them who have already graduated, and to wish the best of luck to those who haven't yet.

In addition to my colleagues in College Park, several other collaborators helped make this work possible. Many thanks to the research groups of Louis Taillefer, Sergey Borisenko, and Girsh Blumberg for their contributions to my first and only first author paper. I'd also like to thank Dr. Laura Greene and her group at the University of Illinois for hosting me for another collaborative research project. It was a great opportunity to work with some of the world's foremost experts on the technique my thesis is based on.

Finally, I'd like to thank the people closest to me who have kept me sane throughout the past five and a half years. Thanks to my parents for always being there to commiserate on the ups and downs of the Ph.D. process and to my brother Chris for supporting me as he made his own way through college. Last, but certainly not least, I'd like to thank my wife Caitlin. I will be forever grateful to her for her unwavering support and encouragement while I finished my education. Perhaps more

than anyone else, all of this would not have been possible without her.

Table of Contents

List of Figures

Chapter 1: Iron-Based Superconductors

1.1 History

Superconductivity was first observed in mercury in 1911 by Dutch physicist Heike Kamerlingh Onnes [1]. Not coincidentally, Onnes was also the first to produce liquid helium, which was necessary at the time to achieve the extremely low temperatures required to enter the superconducting state [1]. In the following four decades higher transition temperatures were found in various metallic elements and alloys, but the physical mechanism that was causing the phenomenon was not well understood.

The situation changed in 1957 when John Bardeen, Leon Cooper, and John Schrieffer published what has come to be known as the BCS theory [2–4]. The principle insight of the theory is that superconductivity results when electrons in a material form quasiparticles known as Cooper pairs. Whereas electrons are fermions, which are subject to the Pauli exclusion principle, Cooper pairs are bosons, meaning they can collect in the same low energy ground state that is the superconducting state. The theory posits that electrons that would normally repel each other due to the Coulomb interaction can form attractive pairs with the assistance of phonons, i.e., quantized lattice vibrations. The distortions that phonons generate in a crystal lattice result in centers of positive charge, which can attract two electrons and cause them

to pair. BCS theory has proven quite successful in describing and predicting physical, electronic, and magnetic properties observed in many superconducting materials. However, in other materials, especially high-temperature superconductors, the theory falls short.

For the first two decades of the BCS theory's existence superconductivity was believed by many to have a finite limit with transition temperatures above about 30 K forbidden [5]. This view was proven to be wrong in 1986 when a copper oxide-based ceramic material was discovered with a T_c of 35 K [6]. Further study of these new cuprate superconductors led to even higher transition temperatures, and the current record for a material at atmospheric pressure stands at 133 K for $HgBa_2Ca_2Cu_3O_x$ [7], though higher transition temperatures up to 150 K have been measured under hydrostatic pressure [8]. Recently other classes of unconventional superconductors (so called because they do not seem to obey the conventional BCS theory) have been discovered [9]. One of the more notable groups of compounds is known as iron pnictides, with pnictides referring to group 15 on the periodic table primarily phosphorus, arsenic, and antimony. These materials are notable because they are able to superconduct despite containing elements with large magnetic moments. It was widely believed that high-temperature superconductors would not contain magnetic elements such as iron because magnetic fields are known to suppress superconductivity. These materials are one of the main topics of my thesis, and I discuss their electronic structure and magnetic properties in greater detail in later sections.

1.2 Gap Structure and Pairing Symmetry

An important property associated with a superconductor's pairing mechanism is the superconducting order parameter, denoted as Δ_k because it is a function of the electronic wave vector $\mathbf{k}$. Δ_k is a complex quantity with units of energy whose magnitude represents the strength of the energy gap as a function of direction in momentum space, the energy gap being the difference in energy between the ground state, i.e. the condensate of Cooper pairs, and the excited state of quasiparticles. The order parameter describes how strongly two electrons are bound in a Cooper pair due to interaction with a pairing boson field. For BCS superconductors that boson is a phonon. For unconventional superconductors like iron pnictides it has yet to be definitively proven what the pairing boson is. More generally, the order parameter can be said to represent the macroscopic wave function of the Cooper pairs [10].

While the magnitude of the order parameter is important, its phase is critical in determining the fundamental nature of a materials electronic structure. The sign of Δ on each of the conducting bands of a structure with multiple bands and the potential presence of a sign change in Δ within a single band lead to different types of symmetries in the order parameter, also known as pairing symmetries.

Determining the symmetry of the order parameter is potentially useful for understanding the mechanism of superconductivity in these materials, which is one of the goals of my research. The physical process by which electrons in a BCS superconductor interact with phonons to form Cooper pairs is well understood [2–4]. Since an analogous description does not yet exist for the iron pnictides, more information

about the gap structure could prove useful in determining the pairing mechanism [11]. Several theories of pairing mechanisms have been proposed, and these theories predict different pairing symmetries and conditions on the order parameter. Thus, investigating this aspect of electronic structure provides a way of verifying theories of Cooper pair formation and represents another step towards understanding the fundamental nature of the superconducting state in these materials.

As I discuss in Chapter 2, the iron pnictides are layered materials with most electron transport occurring in two dimensions. Thus, I only consider gap structures for two-dimensional materials. For the simplest case of a single-band superconductor in two dimensions with a perfectly circular Fermi surface, there are two primary options for pairing symmetries. The simplest is *s*-wave symmetry, pictured in Fig. 1.1a. This isotropic order parameter represents the highest possible symmetry, with the pairing symmetry matching that of the underlying Fermi surface. It has been proven that *s*-wave symmetry is required for BCS superconductors, which typically have a single band in their electronic structure [5]. Another single-band possibility is known as *d*-wave symmetry (Figure 1.1b). In this case, the phase of Δ has a sinusoidal dependence on angle in the k_x-k_y plane. Due to this anisotropy, *d*-wave pairing has a lower rotational symmetry than *s*-wave. Because of this sinusoidally varying phase there are directions in momentum space where Δ is positive, directions where it is negative, and specific directions where $\Delta = 0$, that is, the gap disappears. These points are known as nodes in the order parameter.

When additional bands are considered, which is necessary given the multi-band structure that has been observed for pnictides, more complex pairing symmetries

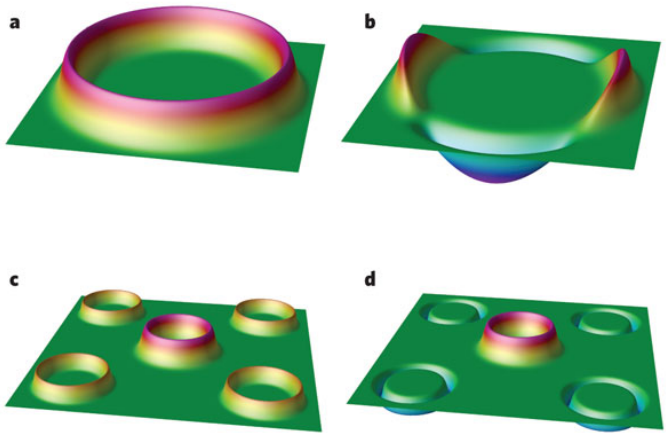

Figure 1.1: Plots of Δ vs. k_x and k_y for various two-dimensional pairing symmetries. a. Single band s-wave. b. Single-band d-wave. c. Two-band s_{++}-wave. d. Two-band $s_{\pm}$-wave. (Adapted from Ref. [12].)

become possible. For two bands, each with s-wave pairing, there are two possibilities depending on the relative signs of the s-waves on each band. If Δ has the same sign on each band the result is known as s_{++} (Fig. 1.1c). If Δ has a sign change between bands the pairing symmetry is called an s_{+-} (Fig. 1.1d). Note that these two-band models have four-fold rotational symmetry. This is a consequence of the pnictides tetragonal crystal structure, which will be detailed in the next section. A general rule is that a materials Fermi surface tends to reflect the symmetry of its crystal structure. The order parameter may have the same symmetry as the Fermi surface (as seen in an s-wave) or a lower symmetry (as with d-waves and other possible symmetries).

Currently the s_{+-}wave is considered the leading candidate for the pairing symmetry of the 122 iron pnictides [11]. Unfortunately, based on the evidence available this has not been proven definitively. One possible complication, the potential pres-

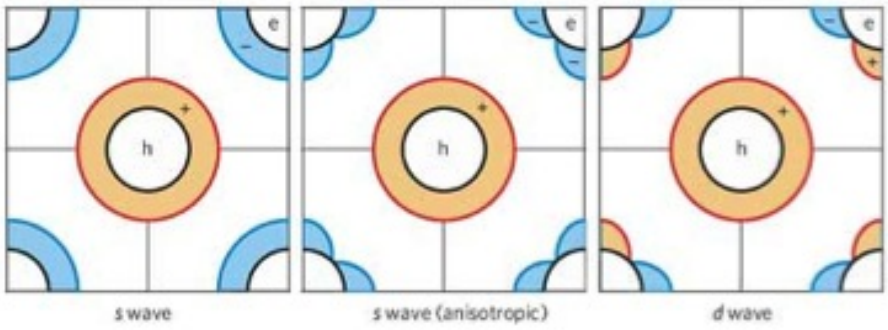

Figure 1.2: Most likely pairing symmetries for 122 iron pnictides: isotropic $s_{\pm}$-wave (left), anisotropic $s_{\pm}$-wave, and d-wave (right). (From Ref. [11].)

ence of accidental nodes, is illustrated in Fig. 1.2.

Figure 1.2 shows three possible pairing symmetries superimposed on a two-dimensional cross-section of the Fermi surface. Though they appear different, the isotropic and anisotropic s_{+-}-wave (i.e., s_{+-} without and with nodes) are fundamentally the same symmetry because they both have four-fold rotational symmetry in the k_x-k_y plane. Similar nodes are also seen in the d-wave case, which has a lower two-fold symmetry. If the true pairing symmetry were an anisotropic s_{+-}-wave, it would be difficult to discern from a d-wave based on their similarities. Experimental techniques exist that detect the presence of nodes or a sign change in the order parameter; however, it would still be challenging to distinguish anisotropic s-wave symmetry from d-wave. The approach I used to differentiate anisotropic s_{+-}- from d-wave is point-contact spectroscopy, which is discussed in Chapter 4.

1.3 122 Iron Pnictides

1.3.1 Crystal Structure

The crystal structure of the iron pnictide superconductors has been well characterized by x-ray diffraction and neutron diffraction. Such analysis has revealed several common characteristics of compounds in the pnictide family. Each compound features a tetragonal unit cell with a distinct layered structure, which explains the materials quasi two-dimensional electronic properties [11]. Common to all of the iron pnictides are Fe-As (or Fe-P, etc.) layers consisting of a square lattice of Fe atoms with As atoms forming separate square lattices above and below the Fe plane and forming bonds such that each Fe atom is tetrahedrally coordinated. For all iron pnictides except the binary compound FeAs, these Fe-As layers are separated by spacing layers containing atoms such as oxygen, fluorine, alkaline earth metals, and rare earth elements. Unit cells illustrating five of the best-characterized iron pnictide compounds are shown in Fig. 1.3.

The first of the group to be discovered [9] was the LaFeAsO structure (fourth from the left in Figure 1.3a). In these materials the spacer layer between Fe-As layers is similarly structured, with a square lattice of oxygen and/or fluorine atoms tetrahedrally coordinated to square lattices of a metallic element (usually rare earth elements such as La or alkaline earth elements like Sr) above and below the plane. This structure is noted for exhibiting the highest transition temperature observed for iron pnictides, 55 K [13].

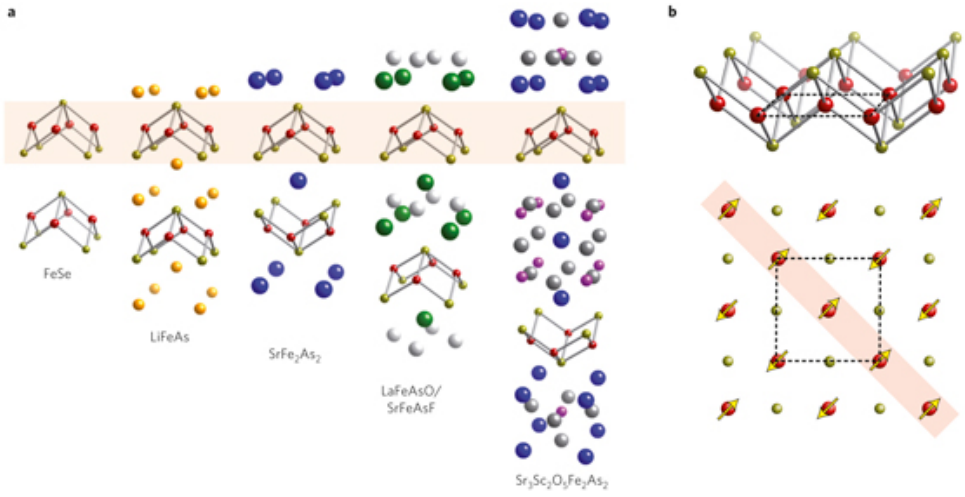

Figure 1.3: a. Unit cells of five of the compounds in the iron pnictide family. b. Closer view of the common Fe-As layers showing the plane of Fe atoms (red) with As atoms (yellow) above and below. (From Ref. [11].)

Of particular interest for my thesis is the $SrFe_2As_2$ structure, the third from the left in Figure 1.3a. This compound and its derivatives are known collectively as 122s (based on the subscripts in their chemical formulas). The 122 unit cell is a body-centered tetragonal lattice with space group I4/mmm. Coordination numbers for each atom present are 8 for Sr (bonds to 8 As atoms), 4 for Fe (bonds to 4 As atoms), and 8 for As (bonds to 4 Fe atoms and 4 Sr atoms). Based on the elements present and simple electron counting the valences of each element should be Sr^{2+}, Fe^{2+}, and As^{3-}.

One set of quantities that is frequently used to characterize 122 compounds is their lattice parameters, i.e., the dimensions of their unit cells. For pure $SrFe_2As_2$ these values are approximately $a = 3.9$ Å and $c = 12.2$ Å as determined by x-ray diffraction [14, 15]. In many experiments different elements are substituted for Sr,

Fe, and/or As. For most of these cases the measured unit cell dimensions behave according to Vegards Law, the principle that lattice parameters should change linearly with the atomic percentage of a substituted element in a solid solution [14–18].

1.3.2 Chemical Substitution and Superconductivity

One of the most notable features of the 122 iron-based superconductors is that superconductivity is not observed in the parent compounds (e.g. $SrFe_2As_2$) under normal conditions. Rather, superconductivity must be induced by either chemical substitution or the application of hydrostatic pressure. As the atomic percentage of a substituted element or the applied pressure is increased from zero, the electronic and magnetic properties of the material change dramatically. These effects can be summarized in a phase diagram, with temperature as a function of either the amount of the doping element or applied pressure. The diagram reveals the regions where different phases are observed and the temperatures at which physical and/or electronic phase transitions occur.

As an example, consider the platinum-substituted system $SrFe_{2-x}Pt_xAs_2$, where x is used to denote the amount of substituted platinum (x = 0 means pure $SrFe_2As_2$, x = 0.1 means 5% of the Fe has been replaced with Pt, etc.) [15]. Single crystals were grown for compounds with Pt concentrations ranging from x = 0 to x = 0.36. Wavelength dispersive x-ray spectroscopy (WDS) was used to measure the precise amounts of Pt in each sample, as well as to verify the expected stoichiometry.

Electrical resistance was measured as a function of temperature for crystals of

each Pt concentration. This was accomplished by attaching gold wires to the crystals with silver paint in the standard four-point probe layout and applying AC current over a range of temperatures in a Quantum Design Physical Property Measurement System (PPMS). The resistances measured were then converted to resistivities using the known physical dimensions of each crystal. The results of these measurements can be seen in Fig. 1.4 (top left) with the resistivity curves for each concentration offset for clarity.

The most striking feature of these curves is the abrupt drop in resistivity at low temperatures for x = 0.09 to x = 0.27. This is the characteristic zero resistance indicating superconductivity. This drop is not observed in the lower concentrations (x = 0 and 0.035) as well as the highest concentration x = 0.36. The resistivity curves also indicate the position of two other transitions. The first is a structural transition from a tetragonal lattice to an orthorhombic lattice, indicated by a kink in $\rho(T)$ for the x = 0 and 0.035 or a minimum in $\rho(T)$ for x = 0.09 to 0.13. It has been shown that the 122 materials exhibit this relaxing of bonds in one of the tetragonal a-directions in order to reduce the magnetic frustration associated with magnetic ordering, and that this structural transition manifests itself as a minimum in $\rho(T)$. The final noteworthy feature of the resistivity curves is the points of inflection seen in the curves up to x = 0.13. Such an inflection point has been shown occur at the Néel temperature, the point where the iron sublattice shifts from a paramagnetic state to an ordered antiferromagnetic state. The minima and points of inflection in the resistivity curves were determined precisely by plotting $d\rho(T)/dT$, shown in Fig. 1.4 (bottom left), and locating the points where the derivative was zero or reached a

maximum. Note that the width of these $d\rho(T)/dT$ peaks was estimated as the error in the Néel temperatures.

The temperatures at which these transitions occurred were used to create the phase diagram seen on the right side of Fig. 1.4. Phase diagrams of this form have been observed for substitution of several different transition metal elements at the Fe site (e.g., $BaFe_{2-x}Pt_xAs_2$) [19], as well as for substitution of alkali metals or rare-earth elements at the alkaline earth metal site (e.g., $Ba_{1-x}K_xFe_2As_2$) [20] and for substitution at the pnictide site (e.g., $BaFe_2As_{2-x}P_x$) [22]. All of these diagrams share two common phase regions. One is the superconducting dome, the finite range of concentrations of the substituted element where T_c rises, reaches a peak value, and then falls off. The other is a region of magnetic ordering (either antiferromagnetic or spin density wave, two similar states which will be discussed later), which also coincides with a structural transition from a tetragonal lattice to an orthorhombic lattice. These two transitions tend to occur at or near the same temperature.

The generally accepted explanation for this behavior is that the magnetic ordering in the Fe sublattice causes magnetic frustration [11]. That is, it is energetically favorable for each Fe up spin (up meaning a spin pointing in the [110] direction) to be surrounded by neighboring down spins, but this is forbidden by the geometry of the lattice. Thus, the lattice expands slightly in one direction to relieve this frustration by separating neighboring spins that point in the same direction.

Several attempts have been made to compare the effects of different substituted elements in order to draw more general conclusions about how these impurities change the electronic structure. Figure 1.5 shows the superconducting dome portions of the

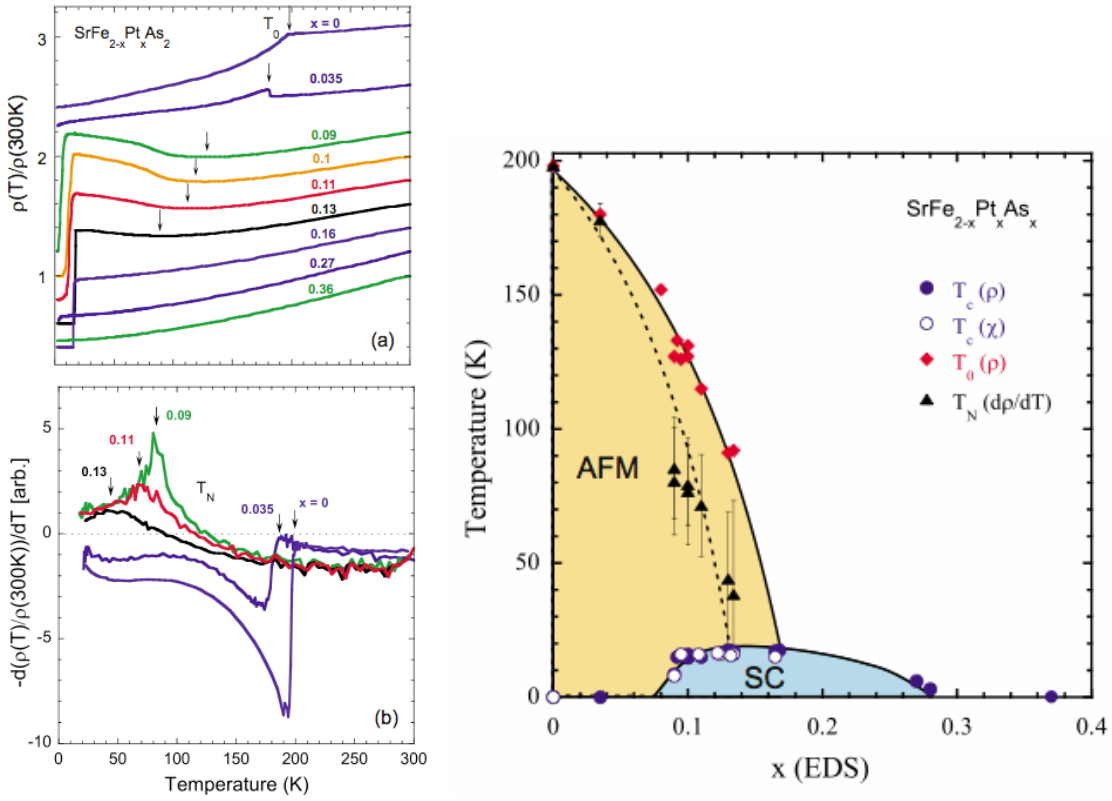

Figure 1.4: Restivity curves for several samples of $SrFe_{2-x}Pt_xAs_2$ for a range of x values (top left), the smoothed derivative curves -$d\rho/dT$ for selected values of x to determine minima and points of inflection in $\rho(T)$ curves (bottom left) and the phase diagram that was generated from these curves (right). In the phase diagram key, $T_c(\rho)$ and $T_c(\chi)$ are the transition temperatures as determined from resistivity data and magnetic susceptibility data, respectively; T_0 is the temperature of the tetragonal to orthorhombic structural transition; and T_N is the Néel temperature, where the magnetic transition was observed. (From Ref. [15].)

phase diagrams for five crystal systems of the form $SrFe_{2-x}M_xAs_2$, where M is a transition metal in column 9 or 10 of the periodic table [15, 16, 23, 24]. Based on the SC domes for Co, Ni, Rh, and Pd one might conclude that the maximum T_c and the concentration at which it will occur can be predicted using a simple electron counting picture. Co and Rh both have one more 3d electron than Fe, and their domes peak at approximately x = 0.3 and T_c = 20 K. Ni and Pd have two more 3d electrons than Fe, and their domes peak around x = 0.15 and T_c = 10 K. By adding twice as many valence electrons per atom, only half the amount of the doping element is needed to achieve the same effect, and all substituted elements in the same column of the periodic table should behave in the same way.

This trend was complicated by the addition of $SrFe_{2-x}Pt_xAs_2$, the most recent system out of the five to be characterized, to the plot (also shown in Figure 1.5). The Pt dome is noticeably wider than that of Ni and Pd, and it has a maximum at around 18 K, much higher than Ni and Pd, though at around the same Pt concentration (about x = 0.15) [15]. This anomaly illustrates one of the main difficulties with understanding the effects of chemical doping and other factors: accurately predicting transition temperatures for new superconductors is nearly impossible, especially considering that the exact mechanism for Cooper pair formation is still unknown for this class of materials. It is widely assumed that scattering of conduction electrons (within bands and between bands in the Fermi surface) plays a major role [11], but a comprehensive model for predicting T_c remains elusive.

The two methods of inducing superconductivity, chemical substitution and hydrostatic pressure, though quite different experimentally, both serve to apply pressure

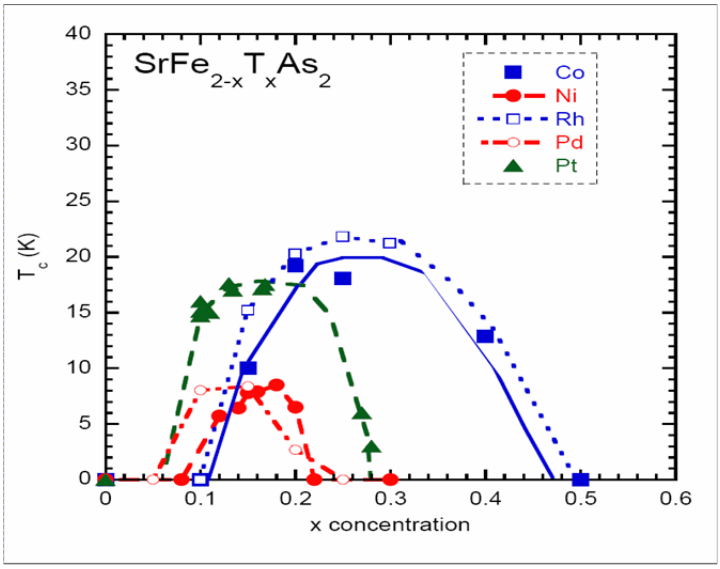

Figure 1.5: Phase diagram showing detail of the superconducting domes for single crystals of $SrFe_2As_2$ with different transition metal substitutions at the Fe site.

to the crystal lattice. With hydrostatic pressure, physical pressure compresses the lattice from all sides and pushes atoms together reducing bond lengths and changing the size of the unit cell. In the case of chemical substitution, systematically replacing one type of atom in the lattice for another with a different atomic radius also applies pressure and has a similar effect on bond lengths and unit cell dimensions. Experimental evidence for a wide range of compounds has shown that chemical substitution and hydrostatic pressure have very similar effects on the electronic properties of 122 materials [11]. Figure 1.6 compares several phase diagrams for $BaFe_2As_2$ with the x-axis representing either chemical substitution or hydrostatic pressure.

The similarities between the phase diagrams in Figure 1.6 suggest that the same phenomenon is inducing magnetic order and superconductivity. Clearly, increasing

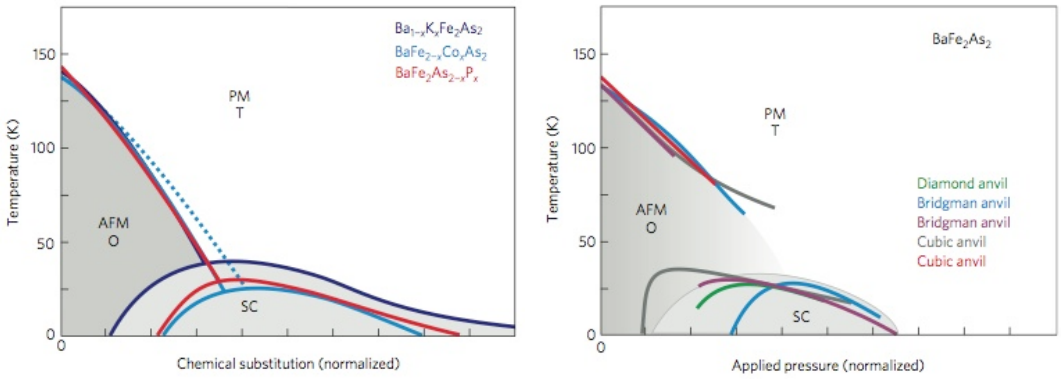

Figure 1.6: Comparison of phase diagrams for $BaFe_2As_2$ with different chemical substitutions (left) and different types of hydrostatic pressure cells (right). The chemical substitution and pressure axes have been normalized so that the antiferromagnetic transitions overlap. (From Ref. [11].)

the concentration of a substituted atom causes an increase in chemical pressure in the same way that a pressure cell applies physical pressure. Furthermore, this suggests that charge doping may not play a major role since hole doping ($Ba_{1-x}K_xFe_2As_2$), electron doping ($BaFe_{2-x}Co_xAs_2$), and isovalent substitution ($BaFe_2As_{2-x}P_x$) seem to have similar effects. If this is the case, the primary effect of substituted elements may be to simply change the lattice parameters and bonding structure, which in turn could change the band structure and Fermi surface in such a way that superconductivity is energetically favorable. The true challenge, then, is to determine exactly how chemical substitution affects the electronic structure and how it can be optimized to create better superconductors with higher transition temperatures.

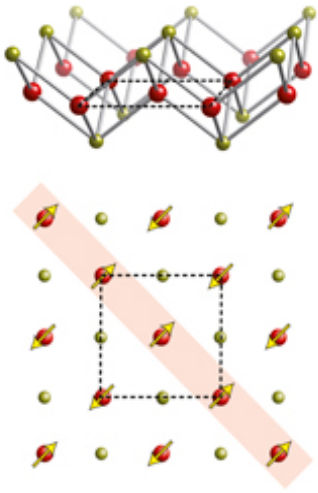

Figure 1.7: Stripe ordering in the Fe-As layer of a pnictide superconductor with one stripe highlighted. Fe atoms are in red; As atoms above and below the Fe plane are in yellow. Dotted line shows redrawing of primitive unit cell when AFM ordering is taken into account. (From Ref. [11].)

1.3.3 Magnetic Properties

As I mentioned previously, some form of magnetic ordering occurs in all Fe-based 122 materials at low temperatures. This is usually in the form of antiferromagnetic (AFM) or spin density wave (SDW) ordering, which are fundamentally very similar. Both entail a spatial modulation of the direction of spins of Fe atoms within the Fe-As planes. The form of AFM ordering seen in many 122s, known as stripe ordering, is shown in Fig. 1.7.

As the name suggests, lines of adjacent atoms with the same spin are present (ordering along the $[1\bar{1}0]$ direction), with atoms on neighboring stripes (separated by a translation along the [110] direction) having spins in the opposite direction. That

is, the lattice exhibits ferromagnetic ordering in one direction and antiferromagnetic ordering in another. This lattice of atomic spins changes the size of the primitive unit cell to the configuration shown in Figure 1.7 with two iron atoms per layer instead of one. This change in lattice size results in a folding of the Fermi surface resulting in the positioning of the electron pockets at $(\pm\pi, \pm\pi)$ in the Brillouin zone.

SDW ordering in these materials looks very similar, but the spatial period between neighboring up spins in the [110] direction is greater. If one imagines the angle of the Fe spins as sinusoidally varying in the [110] direction, the period of this sinusoid is exactly two interatomic distances for AFM. For SDW the period is different, and it is not necessarily an integer number of interatomic distances - this case is known as an incommensurate SDW. Experimentally, neutron diffraction can be used to differentiate between AFM, SDW, and other forms of magnetic ordering [25–29].

One of the most fundamental properties of a material in the superconducting state is perfect diamagnetism. As a superconductor is cooled below its critical temperature, it expels all external magnetic fields such that its volume-normalized magnetic susceptibility drops to a value of $4\pi\chi$ = -1 [5]. This property is quite useful in both verifying T_c values and for determining the superconducting volume fraction of a sample. For a sample that is composed of only a single fully superconducting phase, one would expect the volume-normalized susceptibility to approach -1 at low temperatures and low applied fields. If, however, the entire sample did not enter the SC state or it contains non-superconducting impurity phases, the low temperature susceptibility will reflect this. As a simple example, for a superconducting sample with 50% of its volume composed of a paramagnetic impurity phase $4\pi\chi$ will ap-

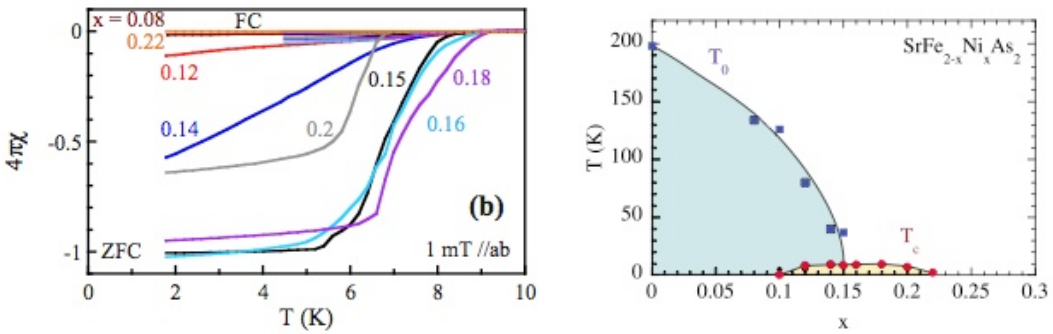

Figure 1.8: Magnetic susceptibility vs. temperature for $SrFe_{2-x}Ni_xAs_2$ samples with the labelled values of Ni concentration x (left) and the phase diagram for the system (right). (From Ref. [16].)

proach -0.5 at low temperatures, a reflection of the average susceptibilities of all of the phases in the sample.

Examples of such susceptibility vs. temperature curves are shown in Fig. 1.8 for samples in the $SrFe_{2-x}Ni_xAs_2$ system with several different concentrations of Ni [16]. The phase diagram for the system is also shown for comparison. Note that concentrations at the middle of the superconducting dome (x = 0.15, 0.16, 0.18) show full diamagnetic screening at low temperatures, while concentrations closer to the edge of the dome have SC volume fractions of less than 100%. As expected, Ni concentrations outside the dome show no diamagnetism.

1.3.4 Fermi Surfaces and Pairing Mechanisms

The highly layered crystal structure of the 122s iron pnictides suggests that conduction should be more favorable in the *ab* plane of the crystal lattice. Thus, these materials ought to have a quasi two-dimensional Fermi surface. This has been con-

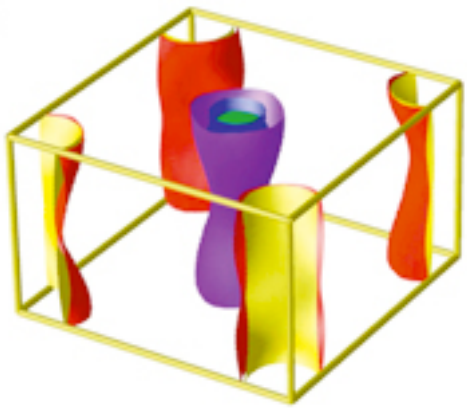

Figure 1.9: Fermi surface of $SrFe_{2-x}Co_xAs_2$ mapped out using density functional theory calculations. Different colors correspond to separate sheets in the FS as a result of multiple bands crossing the Fermi energy. (From Ref. [30].)

firmed by angle-resolved photoemission spectroscopy (ARPES) measurements that reveal the Fermi surface to have roughly cylindrical surfaces [31–34]. Note that for a three-dimensional free electron gas the Fermi surface is spherical, reflecting the isotropy of the system. Likewise, for a two-dimensional conducting surface the Fermi surface is circular in the plane of conduction. The Fermi surfaces measured for 122 materials are not completely cylindrical, as shown in the model in Figure 1.9. This suggests some interlayer conduction, but for my purposes the assumption of a 2D Fermi surface is a good one. Another notable feature of the Fermi surface is the presence of multiple bands. The ARPES data confirm the presence of a hole-like pocket centered at the Γ point in the Brillouin zone and an electron-like pocket centered at the M point, and other experimental results are consistent with a two-band material [31–34].

Based on analysis of Fermi surfaces and the measured effects of elemental sub-

stitution, one can extract information about the possible mechanisms of Cooper pair formation in the iron pnictides. Several studies have shown that superconductivity in these materials does not appear to be purely phonon-mediated. Calculations of electron-phonon coupling strength have failed to account for the high T_c values that have been observed [35]. Studies of the isotope effect in some 1111 and 122 pnictides have shown some electron-phonon interaction - replacing elements in a BCS superconductor with heavier isotopes should decrease T_c by altering the frequency of lattice vibrations [36] - but the effect are small, suggesting that other factors influence pairing.

It has been suggested that magnetic fluctuations could be driving Cooper pairing in the pnictides, a theory that is supported by several observations. One is the presence of nesting vectors in the Fermi surface. In theoretical 122 Fermi surfaces, such as Figure 1.10, as well as in experimentally observed ones the hole and electron pockets have matching shapes. Thus, they can be connected by a scattering momentum vector, known as a nesting vector, as shown in Figure 1.10.

The direction of this nesting vector in momentum space is identical to that of the ordering vector (in real space) of the spin density wave state. The strong connection between magnetic ordering and Fermi surface structure suggests there could also be a link between magnetism and superconductivity. That is, Fermi surface nesting may lead to multiple ordered states: the magnetically ordered spin density wave and the superconducting state [11].

Several experiments have supported the connections between Fermi surface structure, magnetic ordering, and superconductivity. According to density functional

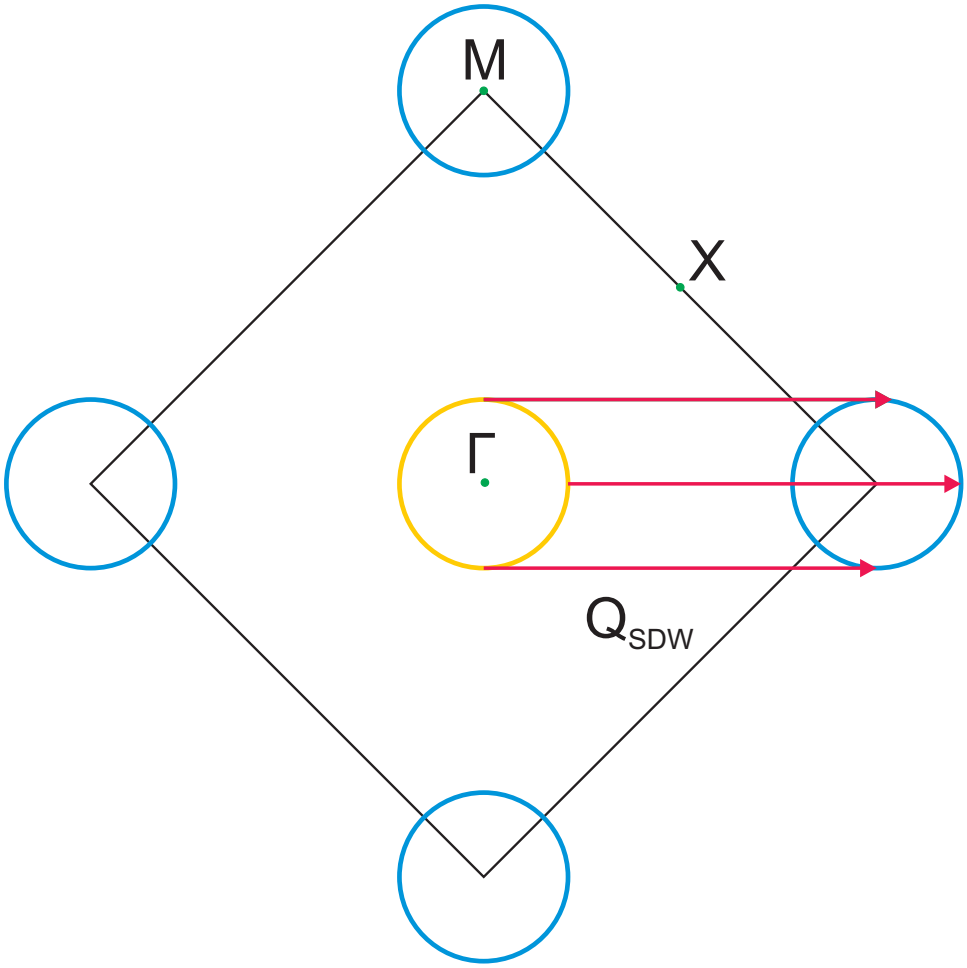

Figure 1.10: Cross-section of 122 Fermi surface showing the nesting vector Q_{SDW} connecting electron and hole pockets. This scattering vector in momentum space matches the ordering vector of the spin density wave state in real space and suggests a connection between magnetic order and superconducting order.

theory calculations, doping pnictides with holes or electrons can change the size of hole and electron pockets on the Fermi surface and possibly disrupt nesting [37]. Electronic structure is also significantly influenced by small changes in crystal structure, including lattice parameters and bond angles [38, 39]. These factors all underline the effects of chemical substitution, which provides charge doping (for most substituted elements) and changes lattice parameters and bond angles. An additional link between interband scattering and superconductivity has been established for optimally doped 122 pnictides suggesting that transition temperature is tied directly to a scattering rate determined using Abrikosov-Gorkov theory. [48] Finally, as I discussed above, superconductivity emerges in the 122 pnictides upon suppression of magnetic order. The combination of these factors strengthens the case for a model of Cooper pairing that is at least partially mediated by magnetic fluctuations.

1.4 Experimental Work on 122 Gap Structure

This section provides a brief summary of some of the experimental work that has been done since the discovery of the 122 iron pnictides to determine their gap structure and pairing symmetry. I provide a description of the experimental details of these techniques is provided in Chapter 3, while Chapter 4 summarizes the results of our experiments using these four methods.

Point-contact spectroscopy (PCS), also known as quasiparticle scattering spectroscopy, is a versatile technique that can reveal information about the electronic structure of a a superconductor. Measurements of electrical conductance vs. DC bias

voltage across a normal metal/superconductor junction provide an indirect probe of density of states. In principle, by fitting such data to the Blonder-Tinkham-Klapwijk (BTK) theory [40] one can determine the of gap size(s) as well as pairing symmetry. [41]

PCS measurements on various doped FeSC systems have resulted in widely varying conclusions about their pairing symmetries, at times contradicting the results from other measurement techniques. Point-contact measurements in the Andreev reflection regime have shown evidence for a two-gap structure in $Ba_{1-x}K_xFe_2As_2$ (Refs. [42, 43]), while $BaFe_{2-x}Co_xAs_2$ spectra have been fit to both one- and two-gap s-wave models depending on the study and even the fitted features in a single spectrum [41, 42] (*i.e.* inclusion or exclusion of zero-bias or higher bias features). Fig. 1.11 shows an example of point-contact spectra measured on $BaFe_2As_2$ crystals with either K or Co substitution. For each curve the data have been fit to the BTK theory, which will be discussed in detail in Section 3.2, to determine the gap size(s). Finally, PCS measurements of $BaFe_{2-x}Ni_xAs_2$ have been used to argue for a two-gap s-wave structure at low Ni concentrations with nodes or deep minima emergent above optimal doping. [44]

Thermal conductivity measurements provide a powerful probe of electronic excitations in the zero temperature limit, when phonons have been frozen out. In a conducting solid at low temperatures, the temperature dependence of thermal conductivity κ can be modeled as $\kappa(T) = aT + bT^{\alpha}$, where the T-linear term aT represents the electronic contribution to heat conduction, while the T^{α} term represents the phonon contribution, where $2 \leq \alpha \leq 3$. By measuring κ/T in the zero temperature

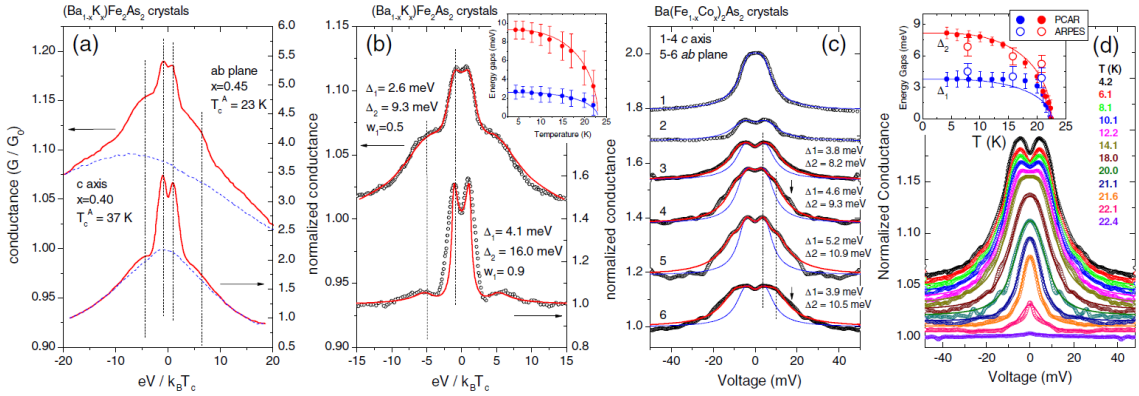

Figure 1.11: Conductance vs. bias voltage spectra for different substituted 122 iron pnictides. (a) Measured dI/dV vs. V_{bias} spectra for $Ba_{1-x}K_xFe_2As_2$. (b) The same curves from (a) after normalization to remove background conductance. Red lines represent fit curves, and the inset shows the evolution of the size of the two observed SC gaps as a function of temperature up to T_c. (c) Similar dI/dV spectra for multiple $BaFe_{2-x}Co_xAs_2$ crystals with different fit curves representing either a one-gap fit (blue lines) or two-gap fit (red lines). (d) Conductance spectra for a single sample measured over a wide range of temperatures. The inset shows the two gap sizes as extracted from fit curves as a function of temperature. (From Ref. [41].)

limit the electron contribution can be isolated, given by $a \equiv \kappa_0/T$. It has been shown that the presence or absence of this residual thermal conductivity at zero magnetic field and its evolution in field can reveal the presence or absence of nodes or zeroes in the SC order parameter and provide additional information about gap structure. [45] For example, in the d-wave cuprate superconductors κ_0/T is nonzero at zero magnetic field. [46] The presence of this same residual thermal conductivity has also been used as evidence for nodal s-wave or d-wave pairing in FeSCs such as $BaFe_{2-x}Co_xAs_2$ citeReid064501 and KFe_2As_2 [48]. Figure 1.12 shows an example of measured κ/T vs. T^2 data for $BaFe_{2-x}Co_xAs_2$ crystals with a range of Co concentrations.

Conversely, the absence of this residual term has been taken as evidence for a nodeless s-wave gap structure in the 18 K superconductor LiFeAs (Ref. [49]). As a function of magnetic field, the evolution of κ_0/T can provide further information about energy scale anisotropies or the presence of multiple gaps with different energy scales, and has been used to differentiate between s-wave superconductors with a single gap (or gaps of equal magnitude on multiple Fermi surface (FS) pockets) and those with multiple gaps of significantly different sizes, *e.g.* differentiating doubly-gapped $NbSe_2$ from single-gap V_3Si [50].

Angle-resolved photoemission spectroscopy (ARPES) is another technique that can provide information about the magnitude of the gap in different directions. In the case of 122 FeSCs, previous work has found two nodeless and nearly isotropic gaps of different sizes on various FS pockets in $Ba_{1-x}K_xFe_2As_2$ [31]. ARPES measurements on $BaFe_{2-x}Co_xAs_2$ have shown evidence for hole pockets disappearing upon increasing Co substitution [32], while a separate study focusing on gap structure [51] observed

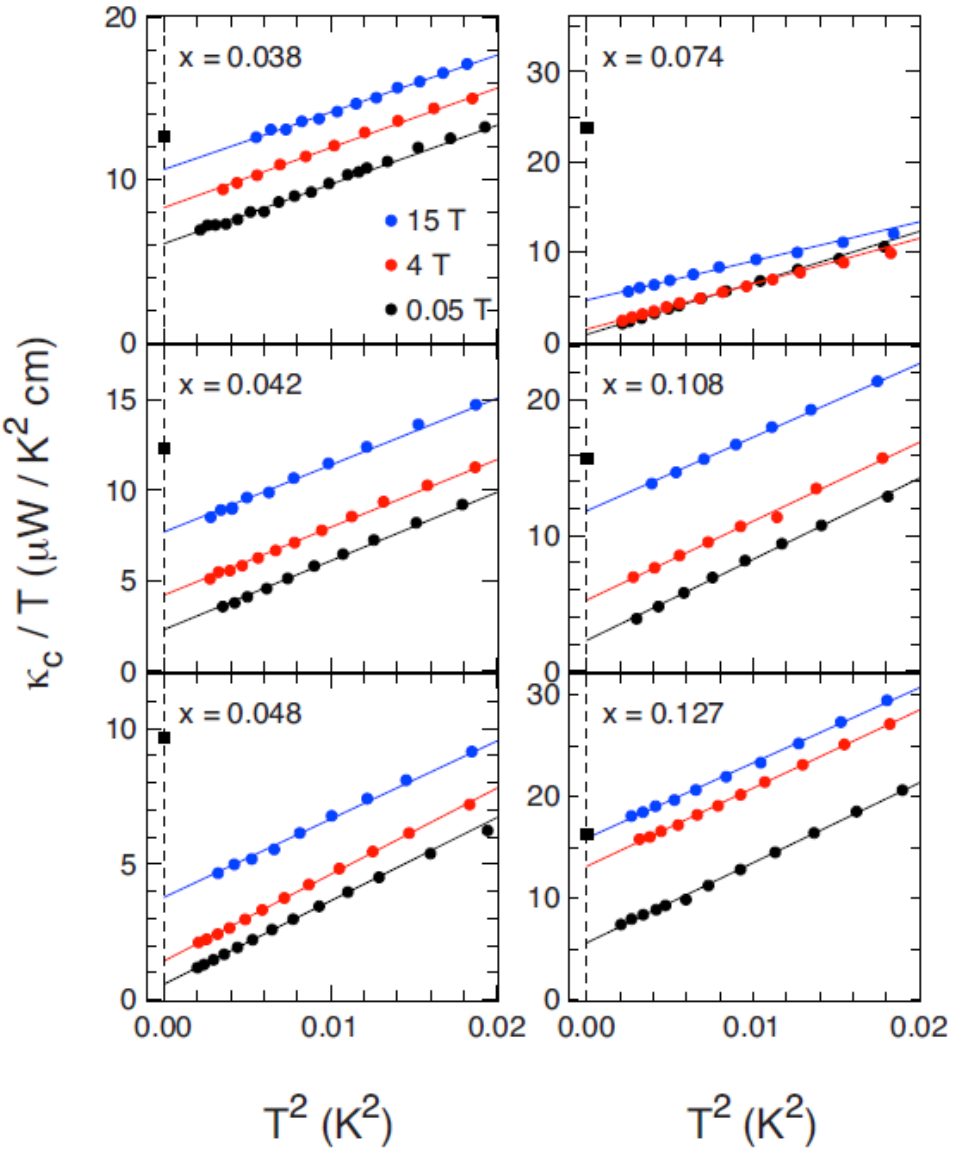

Figure 1.12: Thermal conductivity vs. temperature curves for $BaFe_{2-x}Co_xAs_2$ samples with a wide range of x values and measured at applied magnetic fields of up to 15 T. The extrapolated value of κ/T at $T = 0$ approaches roughly zero for some samples at low field, but at high field an increasing residual thermal conductivity is observed. The presence of a nonzero residual value in the absence of applied field is evidence of nodes in the SC order parameter, and the evolution of the residual term's value in increasing magnetic field reveals further information about the gap structure. (From Ref. [47].)

the presence of two isotropic gaps and suggested a connection between FS nesting and Cooper pairing based on comparison with the hole-doped $Ba_{1-x}K_xFe_2As_2$ case. A sample of ARPES data used to extract gap structure information is shown in Figure 1.13 for the case of a $BaFe_{2-x}Co_xAs_2$ sample. Finally, to date less extensive studies of Raman spectroscopy have been completed in the 122 FeSC materials [41, 52], where one study has shown band anisotropy in $BaFe_{2-x}Co_xAs_2$ supporting a nodal s-wave model [53].

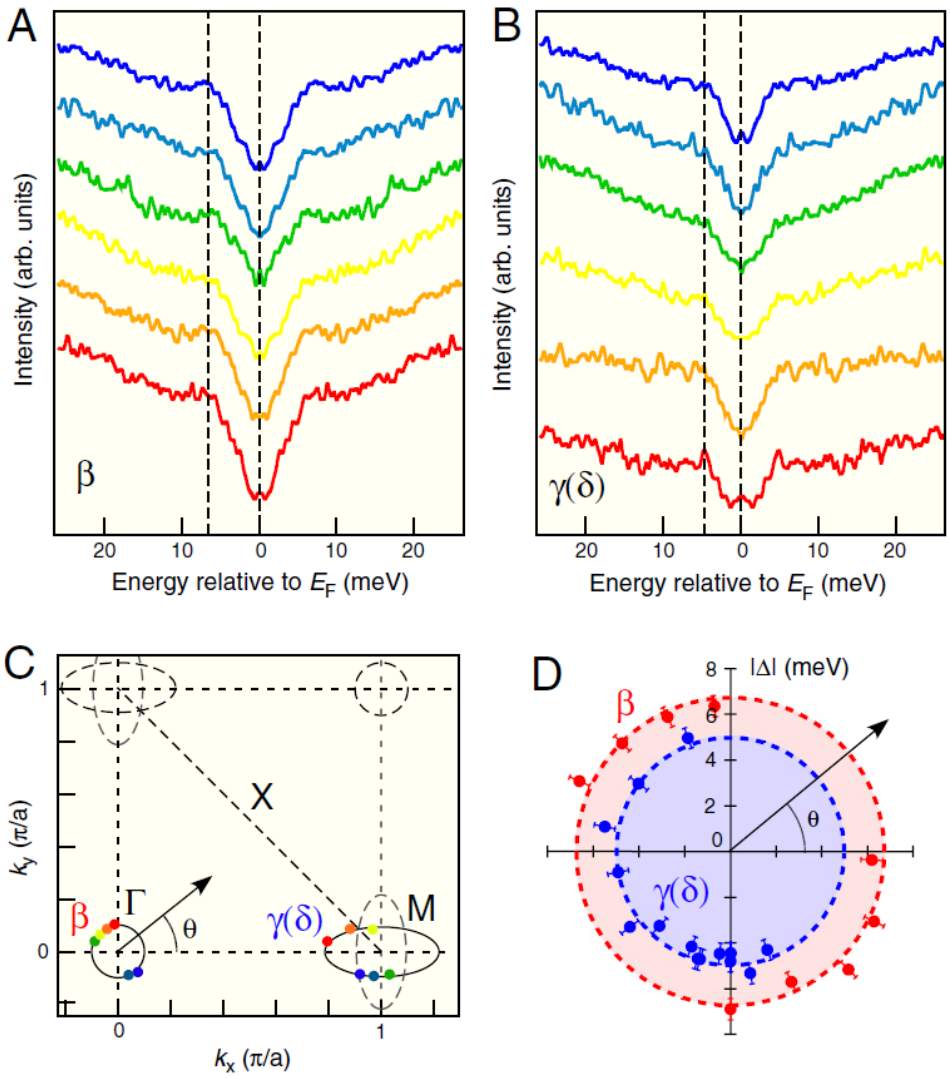

Figure 1.13: Symmetrized energy distribution curves (EDCs) obtained from ARPES showing the density of states at several points on the Fermi surface on the hole-like (A) and electron-like (B) Fermi surface pockets of $BaFe_{2-x}Co_xAs_2$. The specific locations in momentum space where these EDCs were measured are indicated in (C), while (D) shows the magnitude of the two SC gaps as a function of angle in momentum space, demonstrating that the two gaps are isotropic within error. (From Ref. [51].)

Chapter 2: Topological Superconductors

2.1 Topological Insulators

Many material properties can be characterized by symmetries and the phase transitions that break them. For example, the transition from a liquid to a solid phase reduces the spatial symmetry of a substance, while the application of a magnetic field breaks time reversal symmetry of moving electrons. Recently, topological order has emerged as a new classification of matter that does not break symmetries.

Topological order is manifested in materials known as topological insulators (TIs), a class of materials that show great promise both as a source of new and interesting physics but also for potential technological applications. The hallmark of a topological insulator is a phenomenon known as band inversion, in which energy bands with fundamentally different spatial symmetries reverse order. To compare this phenomenon to mathematical topology, the bands of a topological insulator cant be adiabatically transformed into the structure of a conventional insulator or semiconductor, much in the same way that a sphere cannot be adiabatically transformed into a torus. This fundamental rearrangement of bands results in an accidental crossing of energy states at the Fermi level, which turns a nominally insulating material into a conductor at the surface. Fig. 2.1 contrasts the calculated band structures of

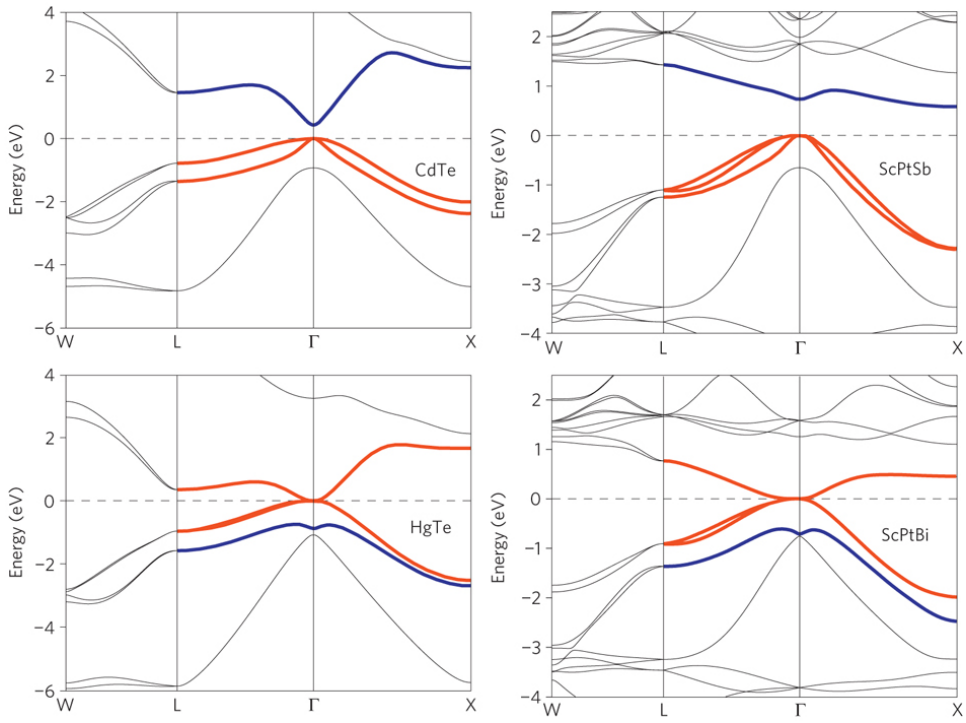

Figure 2.1: Band diagrams for two sets of materials illustrating the effects of band inversion as determined by density functional theory calculations. CdTe and ScPtSb are topologically trivial semiconductors and thus have a gap in the density of states. HgTe and ScPtBi (same crystal structures as CdTe and ScPtSb, respectively) experience an inversion in the order of the bands with Γ_8 symmetry (red) and Γ_6 symmetry (blue) resulting in a crossing at the Fermi energy. (From Ref. [54].)

two predicted topological insulators with their topologically trivial counterparts. As illustrated in Fig. 2.2, these surface states are also spin-momentum locked, meaning that electrons moving along the surface have their momentum locked at a 90-degree angle to their spin.

This spin-momentum locking means that TIs could be useful for spintronic devices. Another interesting behavior has been predicted when superconductivity is induced in a topological insulator by the proximity effect. It has been predicted

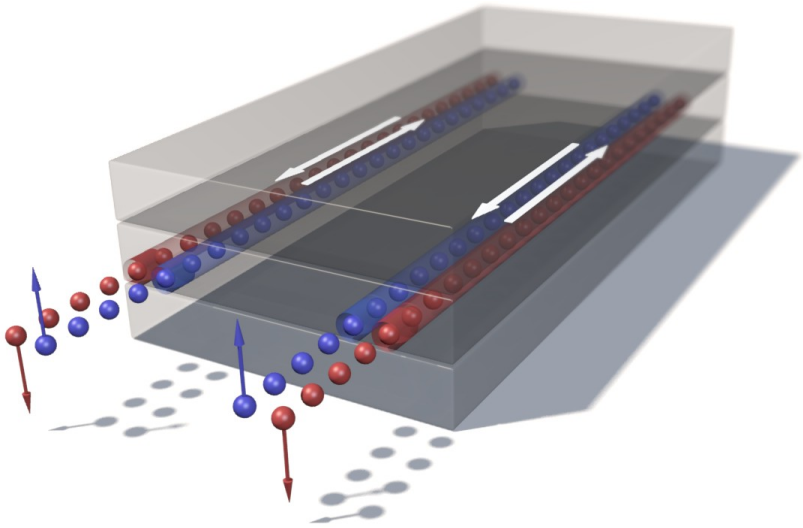

Figure 2.2: Illustration of spin-momentum locking in a topologically insulating surface. Note that electrons with opposite spins move in opposite directions along the edge of the surface. (From Ref. [55].)

that when a TIs surface state becomes superconducting it can support Majorana fermions (MFs). The Majorana fermion is an elusive quasiparticle interaction that is its own antiparticle. It has been proposed that a Majorana bound state, an anyon that obeys non-Abelian statistics, can be formed when a MF is bound to a defect [56]. Because of the unique entanglement expected to occur between these bound states, they could form the basis of a topological quantum computer. This would represent a groundbreaking technological opportunity, but detecting and manipulating MFs is quite difficult. For now, there is still much insight to be gained by studying the unique properties of topological materials themselves.

While some TIs simply have a conductive surface state, others enter a superconducting state at very low temperatures. These topological superconductors are especially promising for technological applications, but they are also interesting purely

because of their differences from other superconductors. Proving that a superconductor is topological or that experimental results are consistent with the presence of MFs can be difficult, but there are some proposed signatures. Section 2.3 will discuss this issue in greater detail as it pertains to a specific class of topological superconductors known as half-Heuslers.

2.2 Noncentrosymmetric Superconductors

It is generally assumed that the superconducting half-Heuslers are unconventional superconductors, but the nature of their superconducting states is still unclear. However, some predictions can be made based on their noncentrosymmetric (NCS) crystal structure. The electronic structure and pairing symmetry of NCS superconductors has been thoroughly explored from a theoretical perspective [57, 58]. Other SCs lacking inversion symmetry have also been detailed, many of which have been shown to be heavy fermion materials.

The lack of inversion symmetry in the crystal lattice affects in how electrons interact with the crystal field via spin-orbit (SO) coupling. This noncentrosymmetry lifts the spin degeneracy of the Bloch bands, thus changing the spin texture of the band in **k**-space. Perhaps most interestingly, NCS superconductors are predicted to support triplet pairing states (S = 1) and chiral or mixed-parity pairing states [58,59], the implications of which will be discussed in this section. The effects of spin-orbit coupling on band structure in NCS materials [57] and the behavior of topological SCs in general [56, 60–62] have been explored in great detail in the literature, but this

work will only focus on the general conclusions from these works.

In a conventional superconductor, the two electrons in each Cooper pair are in a spin singlet (S = 0) quantum state. Furthermore, the gap symmetry is generally an isotropic s-wave. This combination of features is not a coincidence. Because a Cooper pair is an interaction between two fermions its wavefunction must obey the Pauli exclusion principle, imposes the exchange symmetry condition $\Delta_{\alpha\beta}(\mathbf{k}) = -\Delta_{\alpha\beta}(-\mathbf{k})$ on the order parameter. As a consequence, a spin singlet state (antisymmetric with respect to particle exchange) is associated with spatial wavefunctions that are even under applications under the parity operator such as *s*- and *d*-wave. Likewise, a spin triplet state should have an odd parity spatial component such as *p*-wave [63]. While this decoupling of the spin and spatial components of the wavefunction is complicated by spin orbit coupling, the association between triplet pairing and p-wave symmetry is still very strong. These combinations of pairing state and gap symmetry can be seen in Figure 2.3.

The noncentrosymmetric (NCS) crystal structure of materials like the half-Heuslers has led to speculation that they should be unconventional superconductors with a topological nature. In a material whose crystal lattice lacks inversion symmetry the spin degeneracy of the bands is removed and an electronic state that breaks time reversal symmetry becomes possible. The absence of inversion symmetry also introduces a non-trivial topology into the band wavefunctions.

The first NCS superconductor to be discovered was $CePt_3Si$ (Ref. [64]). Many others have been discovered since then, [65–70] and while evidence has been found for unconventional superconductivity the exact nature of the gap structure and pairing

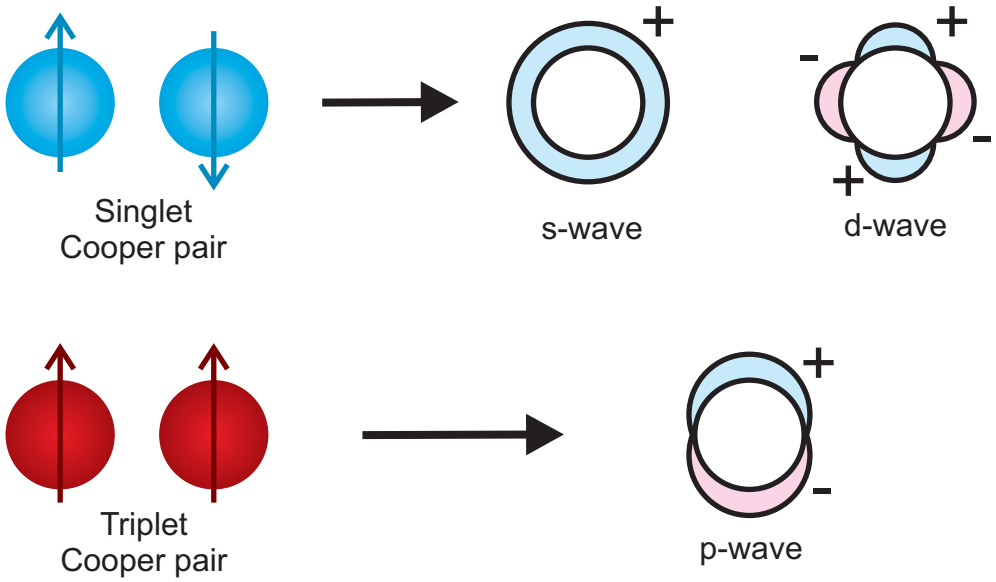

Figure 2.3: Singlet Cooper pairing states are associated with pairing symmetries that are symmetric under application of the spatial parity operator such as s- and d-wave. Likewise, triplet pairing is associated with chiral pairing symmetries such as p-wave.

symmetry has not been settled in most cases. Although it has a centrosymmetric crystal structure, the perovskite Sr_2RuO_4 provides a useful point of comparison. Sr_2RuO_4 is the only material that is widely accepted as a triplet-pairing superconductor with a p-wave gap symmetry. [71] Previous experimental results on Sr_2RuO_4 will be discussed at length in Section 2.4.

2.3 Half-Heusler Compounds

Several materials have been proposed as topological materials and studied in detail, including SmB_6 [72–74] and binary telluride compounds such as HgTe and $Sn_{1-x}In_xTe$ [75, 76]. Another system of note is a system of materials known as half-Heuslers. This family of materials that has been known for decades, but only recently characterized as superconductors with a potentially topological nature.

The crystal structure of half-Heuslers consists of a face-centered cubic lattice in the $F\bar{4}3m$ space group, which is also known as the MgAgAs-type structure. The typical chemical formula is expressed as XYZ where X is typically Sc, Y, or a rare earth element; Y is a transition metal; and Z is a pnictide (or occasionally a Group 14 element), most often Bi or Sb. The half-Heusler structure, shown in Figure 2.4, is characterized by a face-centered cubic (FCC) sublattice of the X atoms, with the Y and Z atoms also arranged in offset FCC sublattices which are located at the Miller indices (1/4, 1/4, 1/4) and (3/4, 3/4, 3/4), respectively. Another way of visualizing this structure is as an overlap of a zinc-blende lattice with the formula XY overlapping with a rock salt (NaCl) structure lattice with formula XZ overlapping at the X sites.

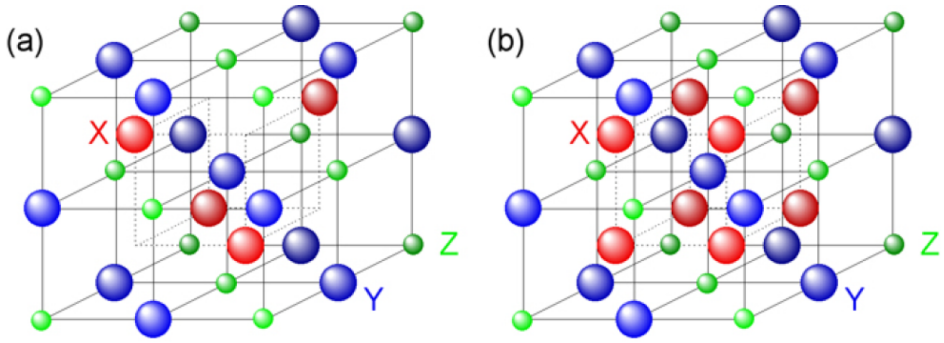

Figure 2.4: a. Half-Heusler and b. Heusler crystal structures with the chemical formulae XYZ and X_2YZ. The non-centrosymmetric half-Heusler lattice consists of face-centered cubic sublattices of X, Y, and Z atoms. Application of the parity operator at the center of the unit cell leads to the red X atoms occupying different sites on the imaginary cube drawn with a dotted line. The centrosymmetric Heusler structure is shown for comparison. (From Ref. [77].)

Perhaps the most striking feature of this crystal structure is that it lacks a center of inversion. It is a well-established principle of solid state physics that crystal structure has a direct effect on electronic structure [78]. In this case, the noncentrosymmetric (NCS) nature of the half-Heusler structure is predicted to affect the superconducting properties of these materials, as was discussed in Section 2.2.

As a note on nomenclature, the half-Heusler structure is a modification of another FCC structure known simply as Heusler compounds. The similar (but centrosymmetric) Heusler structure, also shown in Figure 2.4, is seen in compounds with the stoichiometric formula X_2YZ and is identical to the half-Heusler structure, but with an additional FCC sublattice of X atoms offset by (1/2, 0, 0).

Among superconductors that are predicted to be topological, a wide range of electronic states has been observed at high temperature. For the half-Heusler SCs

some significant differences in electron transport properties have been measured depending on the elements present in the structure. For example, YPtBi (which will be discussed at length in Chapter 5) is insulating at high temperature, but as it is cooled down below roughly 150 K a crossover to metallic behavior is observed and resistivity decreases down to T_c. In the chemically similar material YPdBi, no transition is observed and resistivity increases monotonically down to T_c. Making a different elemental substitution to LuPtBi results in similar semimetallic behavior in ρ vs. T [79], but LuPtBi and YPdBi behave significantly differently when comparing magnetic susceptibility vs. temperature. [cite] Significant differences have also been observed in the residual resistivity ratio (RRR), expressed as $\rho(300\text{ K})/\rho(0\text{ K})$, where $\rho(0\text{ K})$ is extrapolated from low temperature resistivity, ignoring the zero resistivity SC transition if present. These differences in resistivity highlight the complex effects produced by elemental substitution and the difficulty of making theoretical predictions.

Several studies have investigated the electron transport properties of different half-Heusler compounds, but here I will focus on YPtBi. YPtBi was first characterized by Canfield *et al.* [80], who found that the resistance of YPtBi increases by a factor of roughly 25-30% as temperature is decreased from 300 K to 150 K. Superconductivity in the compound was first characterized by Butch *et al.* [81], who observed a SC transition temperature of $T_c = 0.77$ K and a critical field of $H_{c2} = 1.5$ T when $H_{c2}(T)$ was extrapolated to zero temperature. Above T_c, semimetallic behavior was observed, with $\rho(T)$ increasing with decreasing temperature, and then leveling off below roughly 100 K. At high magnetic fields, Shubnikov-de Haas os-

cillations were observed with a frequency corresponding to a hole-majority carrier density of 1.7 $\times 10^{18}$ cm^{-3}. Further analysis of these quantum oscillations revealed a node that introduced a π phase shift and could be consistent with two spin-orbit split Fermi surfaces of similar size. Differences in magnetoresistance behavior were also observed after mechanically roughening the surface, which may be evidence of the predicted surface states. Fig. 2.5 shows electron transport data from Butch *et al.* over a range of temperatures and magnetic fields demonstrating the superconducting transition and quantum oscillations [81].

More recent studies of YPtBi have used other experimental techniques to probe the electromagnetic properties and gap structure. Bay *et al.* [82] observed an unexpected metallic behavior in $\rho(T)$, with resistivity decreasing monotonically down to T_c. Carrier concentration was also much more temperature independent compared to the previous study, though the precise reason for this difference was not clear. Application of hydrostatic pressure caused a consistent increase in T_c up to $p =$ 2.51 GPa. Analysis of normalized upper critical field vs. temperature found that H_{c2} was approximately linear in temperature for all applied pressures. Comparison to the Werthamer-Helfand-Hohenberg (WHH) model and a polar-state model for this data showed a better fit to a p-wave model than s-wave. This unusual H_{c2} behavior, coupled with a large calculated mean free path, was cited as evidence for a dominant odd-parity component in the order parameter.

Further work by Bay *et al.* [83] showed that YPtBi is a bulk superconductor with a volume fraction of approximately 70%. They also found a very small lower critical field, which was argued to be consistent with a non-unitary Cooper pair state.

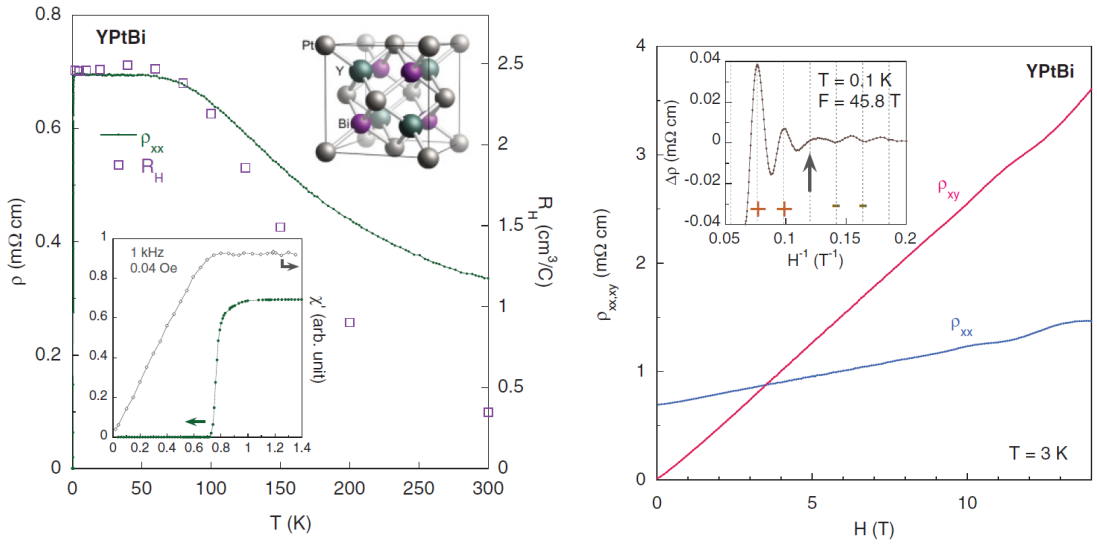

Figure 2.5: Resistivity (ρ, green) and Hall resistance (R_H, purple) vs. temperature (left) in YPtBi with inset showing detail of resistive transition and magnetic susceptibility around T_c and magnetoresistance data (right) with background normalized quantum oscillations shown in the inset. At high temperatures resistivity behavior is consistent with a single-band semimetal, and R_H follows a similar temperature dependence. A sharp transition to zero resistance is observed at $T_c = 0.77$ K, and diamagnetic screening is also seen at this same transition temperature. At 3 K relatively linear magnetoresistance was measured for fields applied both parallel and perpendicular to the direction of current flow and quantum oscillations are seen at high magnetic fields. Similar oscillations were observed at 0.1 K, seen in the lower inset with the background resistance subtracted. The oscillations have a period of 0.02 T^{-1}, which corresponds to an effective mass of 0.15 m_e, and a node appears due to beating resulting in a π phase shift. (From Ref. [81].)

Finally, Shi *et al.* [84] used nuclear magnetic resonance (NMR) measurements to detect enhanced orbital diamagnetism in YPtBi and YPdBi, induced by spin-orbit coupling.

Most published experimental work on half-Heuslers has focused on a single measurement on one or two compounds. Fewer systematic studies examining a range of similar materials have been published. One example is a study by Gofryk *et al.* [85] of polycrystalline RPdBi (where R represents six different rare earth compounds), which included measurements of magnetic susceptibility, resistivity, thermopower, and Hall resistance. It was found that most of the compounds undergo an antiferromagnetic transition at low temperature but that YPdBi is diamagnetic. Electrical resistivity and thermopower measurements were consistent with semimetals with hole-majority carriers. Overall, results were considered to be consistent with theoretical predictions for topological insulators, especially in the case of YPdBi, which has been predicted to have a very small band inversion strength.

Multiple theorists have analyzed the half-Heusler crystal structure using density functional theory (DFT) [54, 86–88]. Calculations of the band structure are able to predict band inversion and the resultant surface states in some half-Heusler materials, but others are predicted to be normal band insulators or semiconductors. As shown previously in Fig. 2.1, significant differences are predicted for various compounds at the Fermi level. For example, ScPtSb is predicted by Chadov *et al.* to be a trivial insulator, while ScPtBi is predicted to undergo inversion of two bands with Γ_6 and Γ_8 symmetries, experience a crossing at the Fermi level, and behave as a topological insulator.

The aggregate of these results can be displayed qualitatively, as shown in Fig. 2.6. These DFT calculations yield a quantity, ΔE representing the difference in energy between the Γ_6 and Γ_8 bands, which represents effective band inversion strength. When ΔE is plotted against the lattice constant or atomic number, general trends emerge. For example, half-Heusler compounds with heavier elements are more likely to be calculated as topologically nontrivial. This is consistent with the role that spin orbit coupling plays in NCS materials, as will be discussed in the next section.

2.4 Experimental Work on Topological and Noncentrosymmetric Superconductors

Experimentally proving that a superconducting state is topological can be challenging. However, finding evidence of a p-wave or mixed parity gap or triplet pairing can be done with standard experimental techniques. Most notably for this work, I will use point-contact spectroscopy to distinguish between different gap structures and pairing symmetries, as discussed in detail in Chapter 3.

The basic idea was modeled by Honerkamp and Sigrist [89], who showed that a triplet pairing state should produce a zero bias peak in the conductivity spectrum as shown in Fig. 2.7. The zero bias peak generally corresponds to an approximate doubling of the high bias conductance, but with a peak morphology that is slightly different from the s-wave shapes seen in, for example Fig. 1.11, and which will be discussed in greater detail in Chapter 3. Furthermore, for all but the largest values of the Z parameter, shallow dips in conductance are predicted at a bias voltage

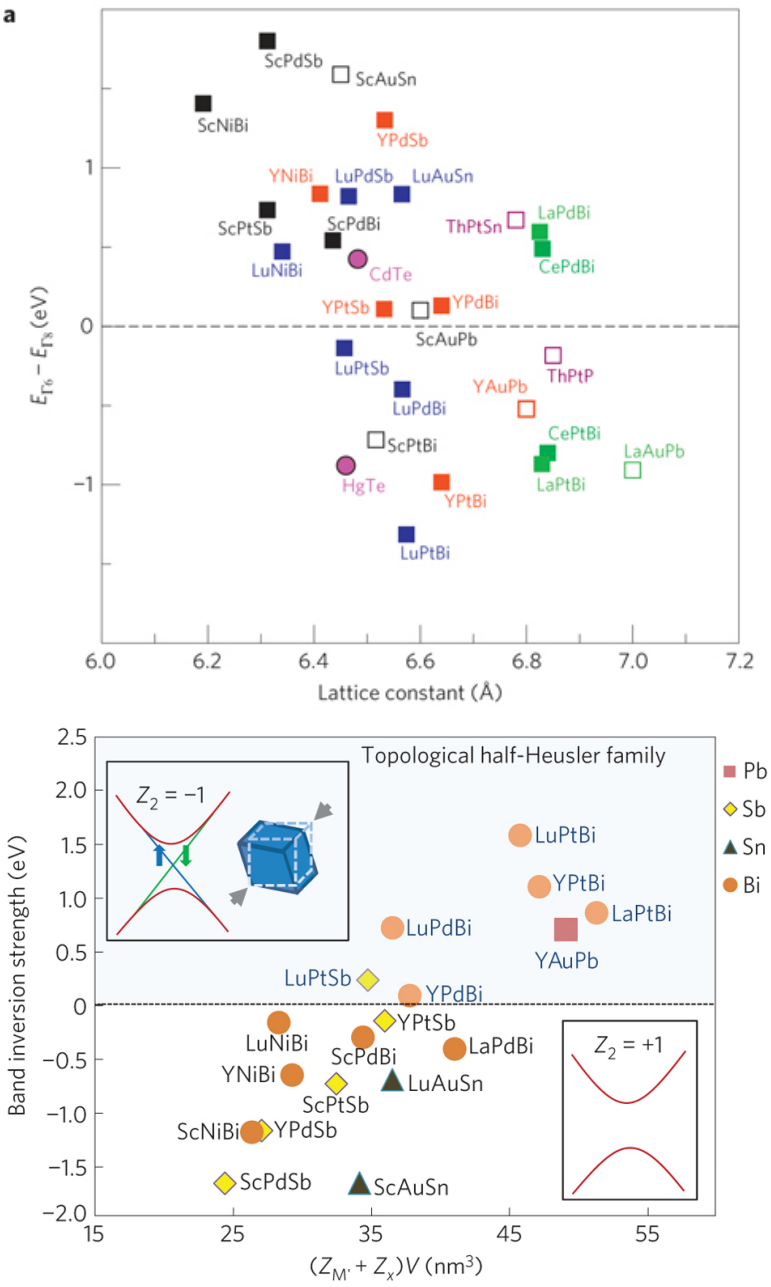

Figure 2.6: Band inversion strength plotted against different parameters for several half-Heusler compounds, as calculated from density functional theory. Note that in the upper figure (from Ref. [54]) band inversion is identified by a negative value of $E_{\Gamma 6}$-$E_{\Gamma 8}$ while in the lower figure (from Ref. [86]) topological materials are identified by a positive value of band inversion strength.

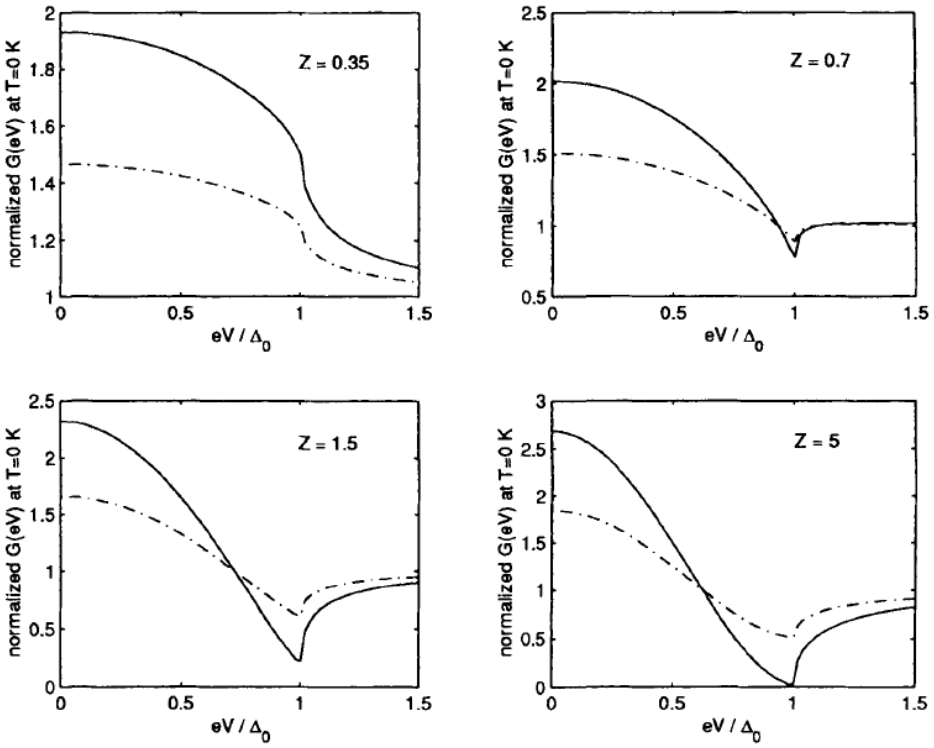

Figure 2.7: Predicted dI/dV spectra for a triplet superconductor for a range of Z values. (From Ref. [89].)

corresponding to $\pm\Delta$. This feature is not uncommon for predictions of dI/dV curves for unconventional superconductors (it is also seen in a d-wave model under certain conditions, for example). However, the specific shape of the peaks and dips still set the triplet model apart, and other experimental methods could also be used to confirm the triplet pairing state.

Laube *et al.* performed point contact measurements on the proposed spin-triplet p-wave SC Sr_2RuO_4 [90] to test this model. Using the needle-anvil technique in a dilution refrigerator they observed two distinct types of conductivity spectra. Some junctions showed a double peak structure at zero bias, which is often a characteristic of s-wave SCs, but with very small enhancement in conductivity at zero bias (about 3% compared to high-bias values). Other junctions had dI/dV curves with a single zero bias peak (10-15% enhancement) and small dips at higher bias. Both of these morphologies were fit to a triplet pairing model allowing a tunable transparency, and the temperature dependence of the gaps was consistent with that expected for an triplet pairing.

Recent work by Sasaki *et al.* sheds more light on how topological superconductivity manifests itself in point-contact measurements with studies of $Cu_xBi_2Se_3$ (Ref. [91]) and $Sn_{1-x}In_xTe$ (Ref. [92]). In both cases a clear zero bias conductance peak was observed in dI/dV spectra accompanied by dips on either side of the peaks. Based on the shape of these features and their evolution in magnetic field it was argued that the peaks are caused by an Andreev bound state (ABS) rather than Andreev reflection, reflectionless tunneling, or magnetic scattering. Based on analysis of the symmetry of the Hamiltonian, it was argued that in each case the ABS must be caused by an

unconventional, odd-parity bulk SC state. Furthermore, in the case of $Sn_{1-x}In_xTe$, the zero bias enhancement observed was greater than 100% compared to the high bias value [92], which is impossible for typical Andreev reflection. This was cited as further evidence for the ABS. It should be noted, however, that more recent work on $Cu_xBi_2Se_3$ using scanning tunneling spectroscopy shows a full gap in the density of states with no zero bias features [93], which puts this work into question.

Another technique that could potentially distinguish triplet pairing is nuclear magnetic resonance (NMR) measurements of the Knight shift. In NMR spectroscopy the nuclear spins in the target material are aligned using an external field, then a radio frequency pulse is applied and the samples relaxation response is measured. The Knight shift is a characteristic shift in the frequency of nuclei due to the spins of conduction electrons. For a conventional superconductor with spin-singlet Cooper pairs the Knight shift should detect a sharp change in spin susceptibility as a function of temperature below T_c. In the presence of a small magnetic field, singlet Cooper pairs will not be broken, meaning the SC state has a low net magnetization compared to that produced by the unpaired electrons in the normal state. In a triplet SC however, the low-field spin susceptibility should not change below T_c because the conducting electrons transition from a collection of single electrons with aligned spins to a collection of Cooper pairs with similarly aligned spins.

This phenomenon has provided direct evidence for triplet pairing in Sr_2RuO_4, one of the only materials in which the presence of a triplet pairing state has been convincingly established. As detailed in a review by Mackenzie and Maeno [71], spin susceptibility χ_s is the result of Zeeman splitting of electron states into spin-up

and spin-down Fermi surfaces. In a SC with a singlet pairing state, this splitting suppresses Cooper pair formation, as the two electron states necessary to form a pair ($\mathbf{k}\uparrow$ and $\mathbf{k}\downarrow$) no longer exist at the Fermi surface. In the superconducting state, the free energy gain from condensation into the SC state dominates and χ_s is reduced to zero as $T \to 0$. For a spin triplet SC, however, this spin splitting does not affect Cooper pair formation. Thus, for a triplet superconductor in a low applied field, spin susceptibility is strong both above and below T_c, as both individual electrons or spin-aligned Cooper pairs will align in the direction of the field. This persistence of χ_s below T_c in Sr_2RuO_4 was confirmed experimentally by Ishida *et al.* [94] in an applied field of 0.65 T. The stark contrast between expected behavior for singlet and triplet superconductors makes Knight shift measurements a prime candidate for unearthing the nature of the pairing state in YPtBi and other half-Heusler materials.

Evidence for unconventional superconductivity could also be found from measurements of the penetration depth and muon spin relaxation. The London penetration depth λ_L of a SC can be measured by several methods, including magnetic force microscopy, SQUID microscopy, and microwave cavity perturbation. For a conventional s-wave superconductor, the quantity $\Delta\lambda_L = \lambda_L(T) \;\; \lambda_L(0)$ should have an exponential T-dependence at low temperature. Deviations from this expected behavior, for example a linear $\lambda_L(T)$ in the cuprates, can be evidence of nodes [95]. In Sr_2RuO_4, $\Delta\lambda_L$ vs. T is quadratic at low temperatures as measured by Bonalde *et al.* [96]. This may be evidence in favor of non-s-wave superconductivity, but isnt completely conclusive due to complicating factors that may have caused this quadratic behavior.

Finally, muon spin relaxation (μSR) is a useful probe for measuring the local distribution of magnetic field in a solid. In this technique, a beam of spin-polarized muons are directed at a sample so that they come to rest inside it before decaying into a positron and two neutrinos. The positrons will be emitted in a direction that correlates with the local magnetic field at the site of the decay, and by observing positron polarization as a function of time one can extract information about magnetic fields inside the sample. In the case of Sr_2RuO_4, the muon spin relaxation rate has been shown to increase below T_c, which is likely due to the internal magnetic field caused by spin triplet Cooper pairs [97]. Enhancement of this relaxation rate is believed to be an indicator of broken time reversal symmetry. But like the case of non-exponential penetration depth, unconventional superconductivity is not the only possible explanation, although it appears to be the most plausible.

Chapter 3: Experimental Methods

3.1 Sample Preparation and Initial Characterization

3.1.1 Crystal Growth

All the experiments I carried out for this thesis involved measurements of single crystal superconducting samples. Working with single crystals is especially important to maintain consistency between research groups and even materials made by the same individuals. The introduction of microstructure and polycrystallinity adds another potential complication, as it can be difficult to ascertain how much the grain size and shape or presence of grain boundaries is affecting an electronic or magnetic measurement. This section details the crystal growth process with a particular emphasis on the growth of 122 materials.

One of the reasons the 122 iron pnictides are so attractive to study is that large single crystals can be grown relatively easily with the flux method. In flux-aided crystal growth the component elements are melted together along with an additional non-reacting component that helps the other components dissolve and mix together. The flux also provides a liquid medium in which single crystals of the desired solid material can grow [16, 98].

The flux method requires a few extra steps when dealing with arsenic, which is toxic and sublimes at 614 °C. Sublimation can be avoided by pre-reacting arsenic powder to form a compound that melts, usually the binary compound FeAs. This is achieved by sintering (i.e., heating a powder below its melting point) stoichiometric amounts of powdered Fe and As together, which results in the formation of the FeAs phase.

The FeAs powder is then combined with a stoichiometric amount of Ca, Sr, or Ba metal pieces as well as the correct amount of any doping element in an alumina crucible along with a large amount of flux, either extra FeAs or Sn. The crucible is then sealed under argon gas in a quartz tube. This is necessary to prevent the formation of oxides at the high temperatures required to melt the component materials.

The quartz tube is heated and cooled in a box furnace according to established heating schedules that usually last approximately one week. These temperature vs. time profiles generally require holding the mixture at multiple high temperatures to allow each component of the mixture to melt for a long enough time for all components to combine via diffusion. The mixture is then cooled slowly, allowing large single crystals to grow. For these materials, large means sizes on the millimeter scale. Typical crystals used for resistivity measurements are on the order of 1 mm $\times$ 2 mm $\times$ 0.05 mm, though under optimal conditions the size of the crystals is limited only by the size of the container usually about 1 cm.

When excess FeAs flux is used, the mixture is allowed to cool by simply programming the furnace to shut off once the heating schedule is completed. Once it reaches room temperature, the alumina crucible is broken and shiny, platelet-shaped

single crystals can be extracted from the solid, dull gray flux with tweezers and a razor blade. For Sn flux, the crystals cannot be extracted so easily. In this case, the quartz tube must be removed from the furnace at a temperature that is below the melting point of the 122 crystals but above the melting point of the Sn. The hot tube is then spun in a centrifuge to separate out most of the liquid flux, leaving the crystals behind. Usually these crystals still have some Sn flux on the surface. This can be removed by etching in HCl.

Fig. 3.1 shows an example of 122 crystals grown using the FeAs flux method. Note that the platelet shape observed in these crystals is caused by the relative strength of bonds within the lattice. The Fe-As bonds are stronger than Sr-As bonds, thus growth occurs preferably in the *ab*-plane, which reflects the layered crystal structure.

In the case of the half-Heuslers the same flux method is used, but with excess Bi as the liquid medium. This is possible because Bi has the lowest melting point of the component elements in this family of compounds. Much like Sn flux growths of 122 iron pnictides, Bi flux must be separated from the crystals at high temperature. This is done either by the centrifuge method or by decanting, that is, inverting the quartz tube containing the crucible immediately after removal from the furnace so that the molten Bi can flow downward into an empty crucible, thus leaving the crystals behind.

The Bi-flux method is currently the only known effective technique for growing half-Heusler materials and it typically yields fairly large crystals as shown in Fig. 3.1. Although not as large as optimal 122 crystals, the largest half-Heusler crystals are typically a few mm in length, which is large enough for the purposes of most of the

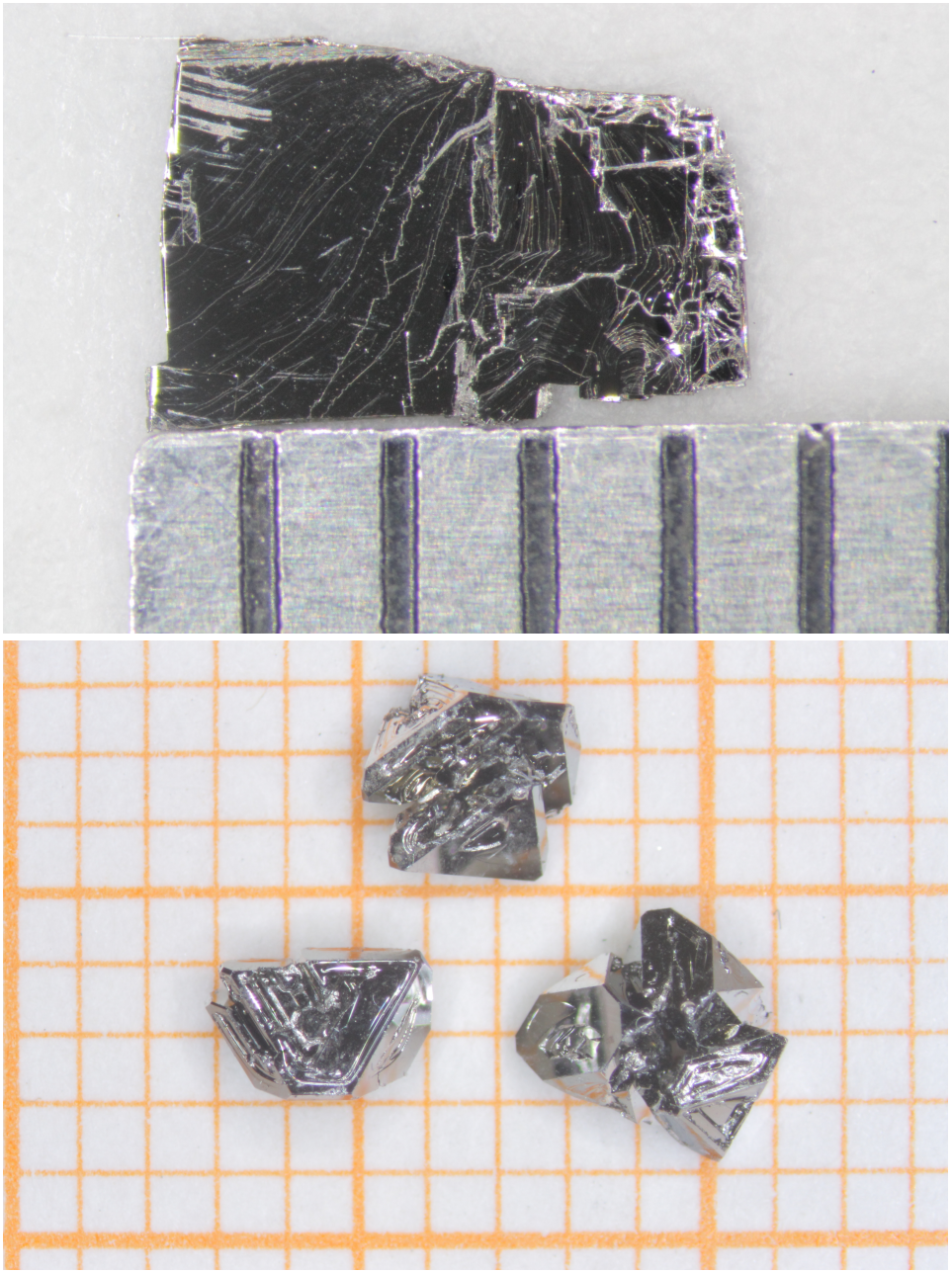

Figure 3.1: Single crystals of $BaFe_{1.9}Pt_{0.1}As_2$ grown in FeAs flux (above) and crystals of the half-Heusler LuPdBi grown in Bi flux (below).

measurements. Also of note is the shape of the crystals. Because of their cubic crystal structure, half-Heusler single crystals do not grow as platelets. As a result, I had to sand the crystals flat to expose a large face for the application of electrical contacts.

One final complication of working with half-Heusler crystals is the presence of residual Bi flux inside the material. In nearly all of my samples I typically observed under a microscope, small discolored areas have been observed on the surface. Elemental analysis using energy dispersive x-ray spectrometry in a scanning electron microscope reveals that they represent Bi inclusions. Figure 3.2 shows a close-up of these inclusions on a polished LuPdBi crystal as observed with a differential interference contrast microscope. Because the inclusions are small and fairly sparse it is generally assumed that they do not have a significant effect on experimental results.

3.1.2 Resistivity

The resistance of large samples can be determined by a simple two-point measurement with an ohmmeter. Such a measurement would be difficult for the small and highly conductive crystals used in my experiments, as the resistance of the contacts would not be negligible compared to the sample resistance. This problem can be remedied by using a four-point probe method, which utilizes four electrical contacts on the sample. In this method a known current I is applied to two outer contacts and the voltage drop V caused by that current is measured between two inner contacts (see Fig. 3.3). Since very little current passes through the wires on the voltage contacts, the voltage dropped across them is very small, and the voltage drop measured

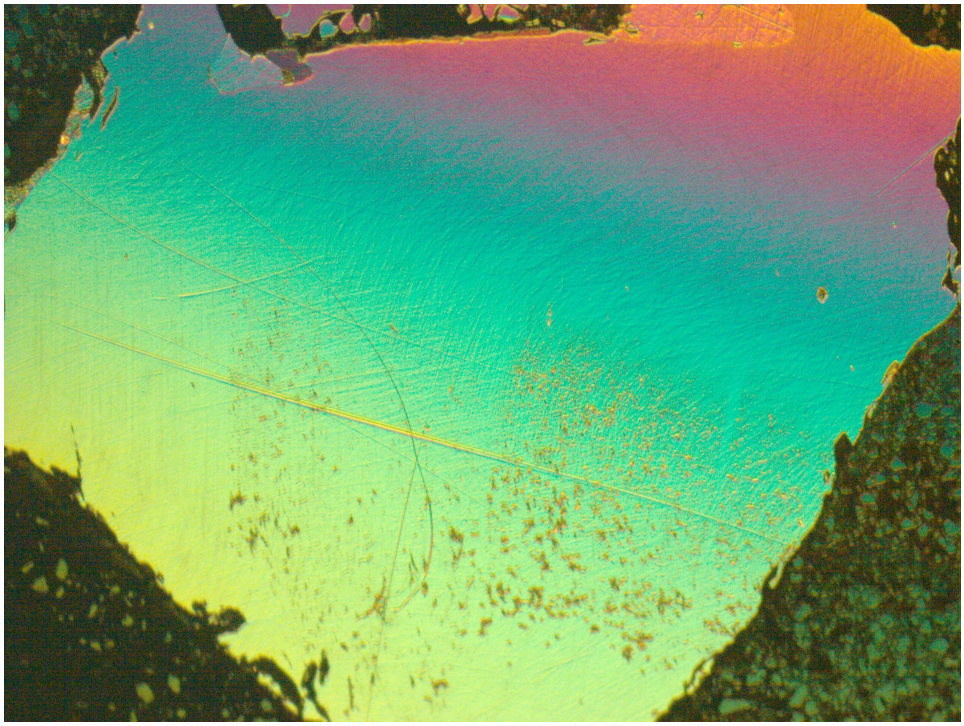

Figure 3.2: Image of polished LuPdBi crystal captured with a differential interference contrast microscope. The small spots scattered across the bottom of the crystal are inclusions of Bi flux.

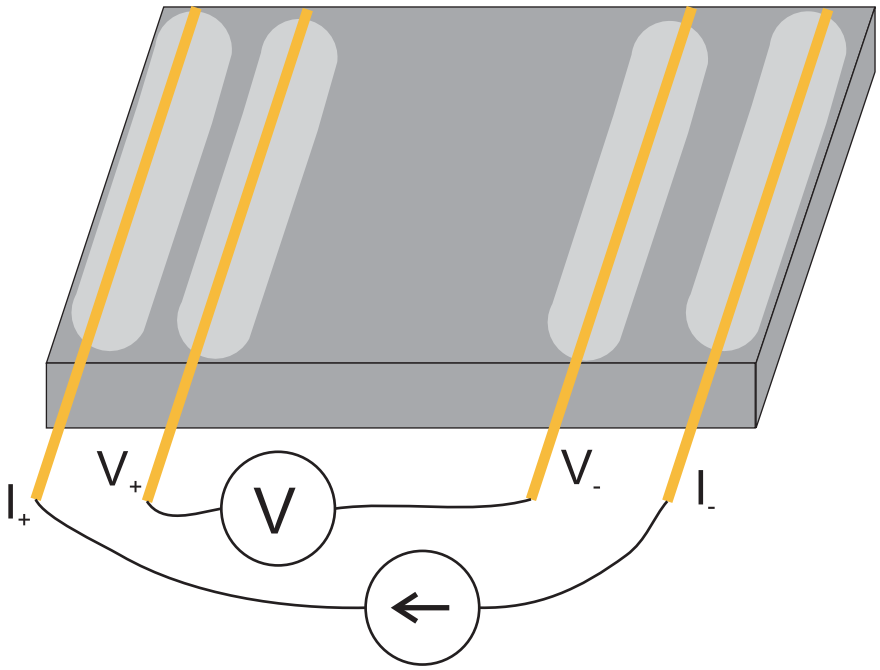

Figure 3.3: Schematic of a resistivity measurement using the four-point probe method. Gold wires are applied across the width of the sample using silver paste or Pb-Sn solder.

can be considered to be entirely across the sample. Using Ohm's Law, the measured current and voltage are then used to calculate the resistance $R = V/I$ between the two voltage leads. I converted the resistance R to resistivity $\rho = RA/l$ by measuring the length l between the voltage leads and the cross-sectional area A of the sample.

When making a four-point resistivity measurement on a 122 crystal I attached, four parallel gold wires, usually 50 μm thick, to the sample with conductive silver paste or Pb-Sn solder. The sample was then mounted on a puck specially designed for use with a Quantum Design Physical Property Measurement System (PPMS). Once inserted into the PPMS, the sample was cooled to as low as 1.7 K and I measured resistivity as a function of temperature. The system was also capable of applying

magnetic field and measuring other physical properties such as specific heat.

While the PPMS was suitable for many measurements, in some cases lower temperatures than 1.7 K were required. Such low temperatures can be attained with a dilution refrigerator, which achieves cooling by taking advantage of a unique property of liquid helium. Helium has two stable isotopes, ^{3}He and ^{4}He. Because the two isotopes are immiscible below a critical temperature, when a mixture of ^{3}He and ^{4}He is cooled below about 1 K they separate in an endothermic process. This process can be then repeated by pumping out the dilute ^{4}He phase and properly adding it back into the remaining ^{3}He phase so that continuous cooling power can be achieved. [57] Theoretically, this could be repeated ad infinitum so that the system exponentially approaches 0 K. Practically, the minimum temperature obtainable is limited by radiative and conductive heating in the sample chamber and is typically in the 10-20 mK range. Resistivity, magnetoresistance, and specific heat measurements can all be obtained with a properly configured dilution refrigerator. The advantage of a dilution refrigerator is the extremely low base temperature, which is necessary for detecting superconducting transitions in the 20 mK to 1 K range and observing the behavior of transport properties (such as resistivity and specific heat) as T approaches zero.

A useful intermediate option is a ^{3}He probe produced by Quantum Design for use with a PPMS. This specialized insert uses a small amount of liquid ^{3}He which is continuously circulated throughout the probe. Given the limited cooling power of a smaller probe with less ^{3}He than a dilution refrigerator, the minimum temperature for the system is only around 400 mK. This is still less than the T_c of many half-Heusler

materials, and the fact that it offers all of the functions of the PPMS and much faster cooling than a dilution refrigerator made it a viable option for many measurements.

3.1.3 Magnetic Properties

The primary tool used for determining the magnetic structures of samples is neutron diffraction, which yields the same crystal structure information as x-ray diffraction while also giving information about magnetic ordering. This is possible because, unlike x-rays, neutrons have a net magnetic moment. Thus, they can be diffracted by an array of periodic magnetic moments ((e.g.), a magnetically ordered lattice). In analyzing neutron diffraction data, one can use Rietveld refinement to separate the crystal lattice peaks (the same peaks one would observe from x-ray diffraction) from additional magnetic peaks. Based on the Bragg angles and peak heights, one can determine the spatial orientation of spins of the atoms in the crystal lattice (e.g., AFM, SDW) through further refinement [25–29].

Magnetic susceptibility can be measured using a superconducting quantum interface device (SQUID), which is capable of detecting very small changes in magnetic field. A SQUID is essentially two Josephson junctions [58, 59] connected to form a loop (see Fig. 3.4). It is known that the magnetic flux through such a loop is quantized in units of the flux quantum $\Phi_0 = h/2e \approx 2.07 \times 10^{-15}$ T*m^2 [99, 100]. When properly current biased, small changes in magnetic field applied to the loop cause the voltage across the loop to vary periodically in the flux. In order to measure magnetic susceptibility, a superconducting sample is placed in an inductance coil that is cou-

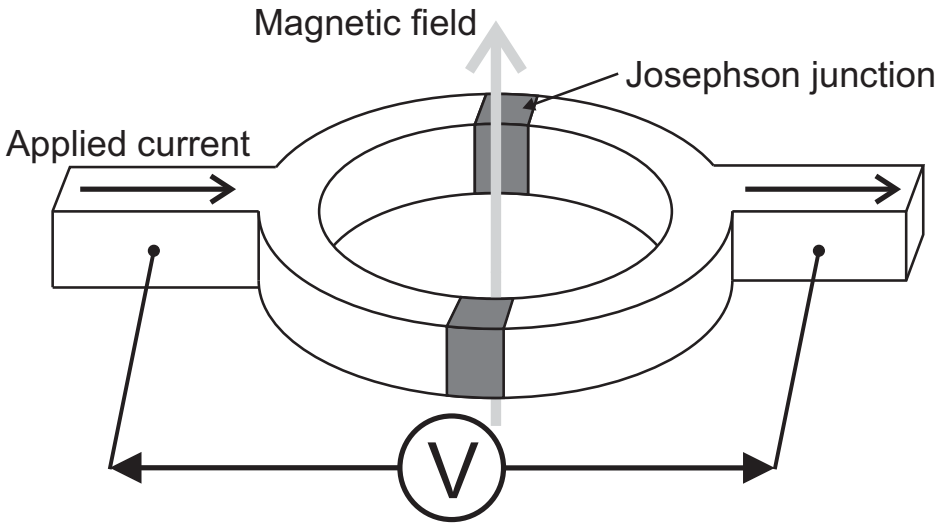

Figure 3.4: Diagram of a superconducting quantum interface device (SQUID), a loop of superconducting material with two Josephson junctions.

pled to the SQUID while a magnetic field is applied. The sample is then physically oscillated in order to induce changes in the field, which in turn causes changes in the voltage across the SQUID. This voltage is a measure of the change in magnetic field, from which one can calculate the net magnetization of the material causing the change and thus the magnetic susceptibility of the sample. The Quantum Design Magnetic Property Measurement System (MPMS), is capable of measuring susceptibility as a function of temperature and applied magnetic field.

3.2 Point-Contact Spectroscopy: Theory

While resistivity and magnetization measurements can reveal a great deal of information about the SC state, they fall short when it comes to understanding the nature of the superconducting order parameter and its symmetries. In contrast,

phase-sensitive experiments are designed to reveal information about gap structure and pairing symmetry. Point-contact spectroscopy (PCS) is a particularly versatile tool that can be used to extract gap sizes and provide some information about phase.

The basis of point-contact spectroscopy is a small junction created between a normal metal tip (N) and a superconducting sample (S) below its transition temperature. Consider the density of states of both materials at the interface. The states in the normal metal are continuous up to the Fermi surface, while the superconductor has a gap between the lower occupied band of Cooper pairs and the unoccupied higher band of excited states. When the Fermi energy of the normal metal falls within this gap, an electron travelling at the Fermi momentum in the normal metal cannot pass through the gap. Since the electron doesnt have sufficient energy to reach an excited quasiparticle state in the superconductor, it must either form a Cooper pair in order to pass into the superconductor or simply be reflected back. This single-electron transmission across the junction is forbidden [5]. In the case where the electron does pass through the barrier and form a Cooper pair in the superconductor, a hole with spin opposite that of the incident electron must be reflected back into the normal metal (this is known as retroreflection) in order to conserve charge, spin, and momentum. This process is known as Andreev reflection and is illustrated in Figure 3.5.

The extent of Andreev reflection can be measured as a function of bias voltage across the N/S junction, which moves the Fermi level of the normal metal up and down relative to the gap. When the bias voltage is such that the Fermi level of the normal metal is above the gap of the superconductor, single electrons can pass through

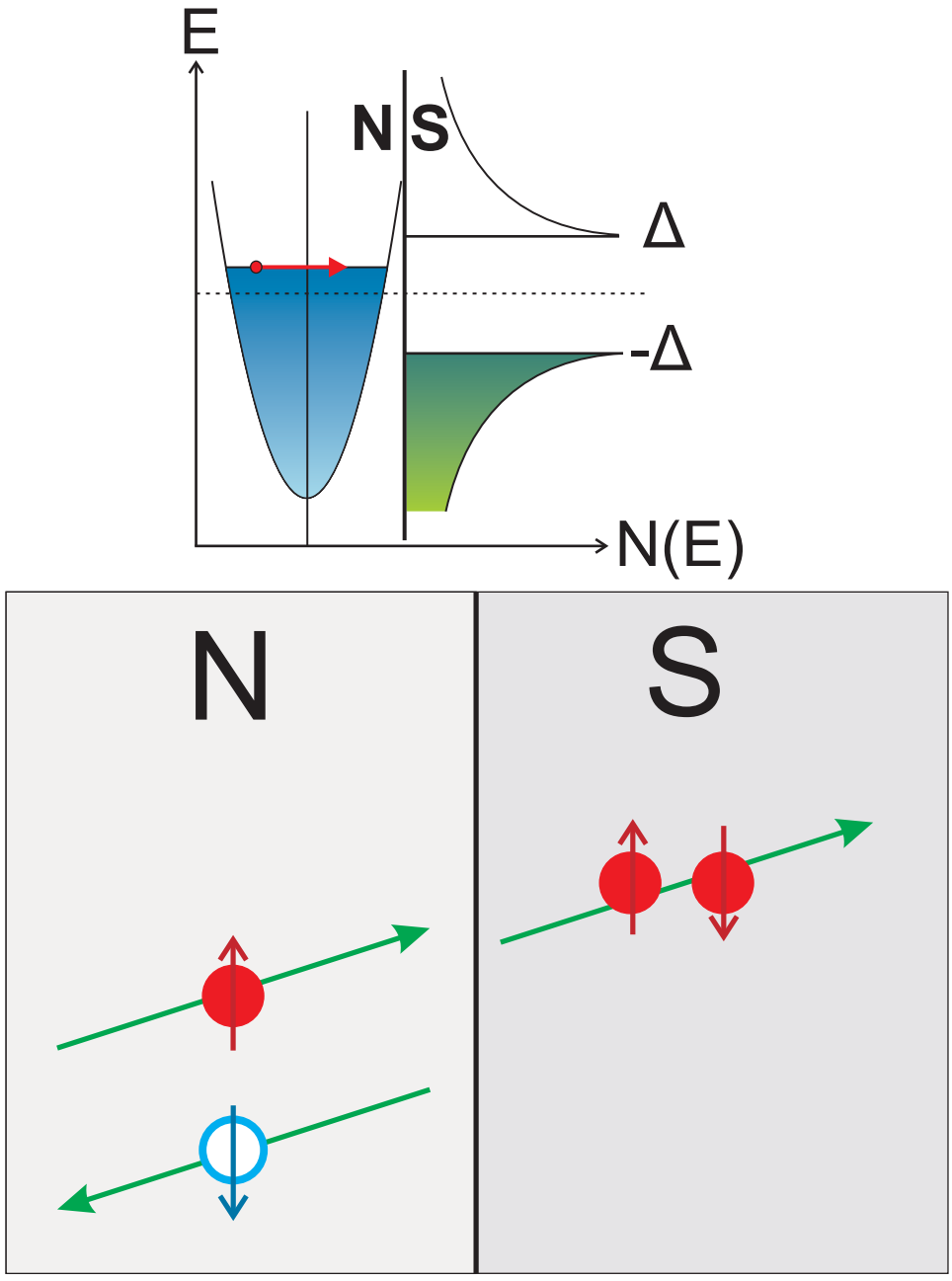

Figure 3.5: Density of states of normal metal (N) and superconductor (S) (top) with the Fermi energy of the normal metal within the SC gap; illustration of Andreev reflection (bottom) with an incident electron at the junction creating a Cooper pair in S and a retroreflected hole in N with opposite spin.

the junction and the conductivity of the junction reaches a fixed value. When the Fermi energy is within the gap (at least in the simplest case), each incident electron generates a Cooper pair and a hole moving in the opposite direction. Since the amount of charge moving has effectively doubled compared to the high bias value, one would expect the conductivity of the junction to double as well.

In practice, the scattering process, and the behavior of the conductivity, is more complex. One very typical complication is the presence of a potential barrier at the junction, often in the form of a thin oxide layer at the surface of the normal metal or superconductor. Similar effects can result from a mismatch in Fermi velocities between the normal metal and the SC [5]. As the effective magnitude of this barrier increases, more electrons are reflected back at the junction rather than transmitted via Andreev reflection. In the extreme case where the barrier is infinitely high, 100% of all incident electrons are reflected and no current passes through, meaning the conductivity drops to zero for all bias voltages within the gap [5]. The height of this barrier is quantified by a unitless fitting parameter labeled Z, which can vary from zero (no barrier, conductivity should double inside the gap) to infinity (strong barrier, no conduction inside the gap).

Blonder, Tinkham, and Klapwijk have quantified the effect of a potential barrier and other factors on conductivity in what has become known as the BTK theory [40]. In modeling the behavior of electrons approaching a N/S junction, the barrier is treated as a delta function potential with height Z. This model [41] assumes that the densities of states for quasiparticles and Cooper pairs in the superconductor are given as

$$N_q(E) = \frac{E + i\Gamma}{\sqrt{(E + i\Gamma)^2 - \Delta(E)^2}} \tag{3.1}$$

$$N_p(E) = \frac{\Delta(E)}{\sqrt{(E + i\Gamma)^2 - \Delta(E)^2}} \tag{3.2}$$

where E is the energy that is controlled by adjusting bias voltage, $\Delta(E)$ is the energy gap, and Γ is a term with units of energy that accounts for inelastic scattering. This is the density of states function illustrated in Figure 3.5. For the BTK model of the barrier as a delta function of magnitude Z, the transmission coefficient for tunneling through the barrier is

$$\tau_N(\theta) = \frac{\cos^2(\theta)}{\cos^2(\theta) + Z^2} \tag{3.3}$$

where θ is the angle between the momentum of the particle incident on the barrier and the normal direction to the barrier $\mathbf{n}$ (e.g., $\theta = 0$ for normal incidence). The relative transparency of the barrier, σ_S, can be written as:

$$\sigma_S(E, \theta) = \frac{1 + \tau_N(\theta)|\gamma(E)|^2 + (\tau_N(\theta) - 1)|\gamma(E)^2|^2}{|1 + (\tau_N(\theta) - 1)\gamma(E)^2|^2} \tag{3.4}$$

where γ is given by

$$\gamma(E) = \frac{N_q(E) - 1}{N_p(E)} \tag{3.5}$$

This quantity can then be integrated over all possible incident angles in the two-dimensional plane to arrive at the expected normalized conductance:

$$G_{2D}(E) = \frac{\int_{-\pi/2}^{\pi/2} \sigma_S(E,\theta)\tau_N(\theta)\cos(\theta)\,\mathrm{d}\theta}{\int_{-\pi/2}^{\pi/2} \tau_N(\theta)\cos(\theta)\,\mathrm{d}\theta} \tag{3.6}$$

Equations 3.1-3.6 assume that the energy gap has no dependence on angle, that is, an isotropic s-wave superconductor. The BTK model can be easily extended to include angular dependence to the gap, as will be demonstrated later. For the simplest case of an isotropic s-wave with no inelastic scattering ($\Gamma = 0$) and at zero temperature, the model produces conductance vs. bias voltage curves (with bias voltage expressed in units of the energy gap divided by electron charge, Δ/e) as shown in Fig. 3.6.

I note in particular the doubling in conductivity within the gap ($-\Delta/e \leq V_{bias} \leq \Delta/e$) for the zero barrier case and the reduction of conductivity to zero in the gap for $Z \gg 1$. The large barrier case also yields high conductivity close to bias voltages of $V = \pm\,\Delta/e$, due to the high density of states in the superconductor at those energies [41]. One can include inelastic scattering using nonzero values of Γ, resulting in curves such as those in Figure 3.7.

Generally speaking, increasing the magnitude of the inelastic scattering term tends to change the shape of the curve by causing more reflection inside the gap for shorter barriers and less tunneling close to the gap for a higher barrier. Other changes occur when accounting for the effect of non-zero temperature. At nonzero temperatures thermal motion causes the density of states to smear out. This is reflected in Figure 3.8 for a low-Z case. The most obvious effect is that the height of the conductance peaks decreases with increasing temperature; this is consistent for

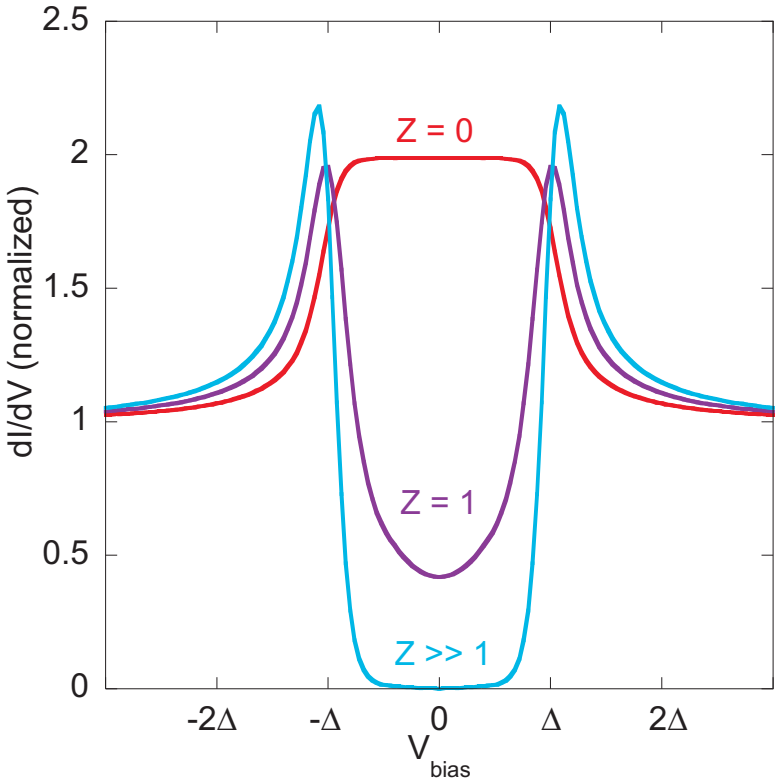

Figure 3.6: Expected conductivity vs. bias voltage curves for Andreev reflection and tunneling with potential barriers of different sizes. Computed from BTK theory with $T = 4.2$ K, $\Delta = 5$ meV, and $\gamma = 0$.

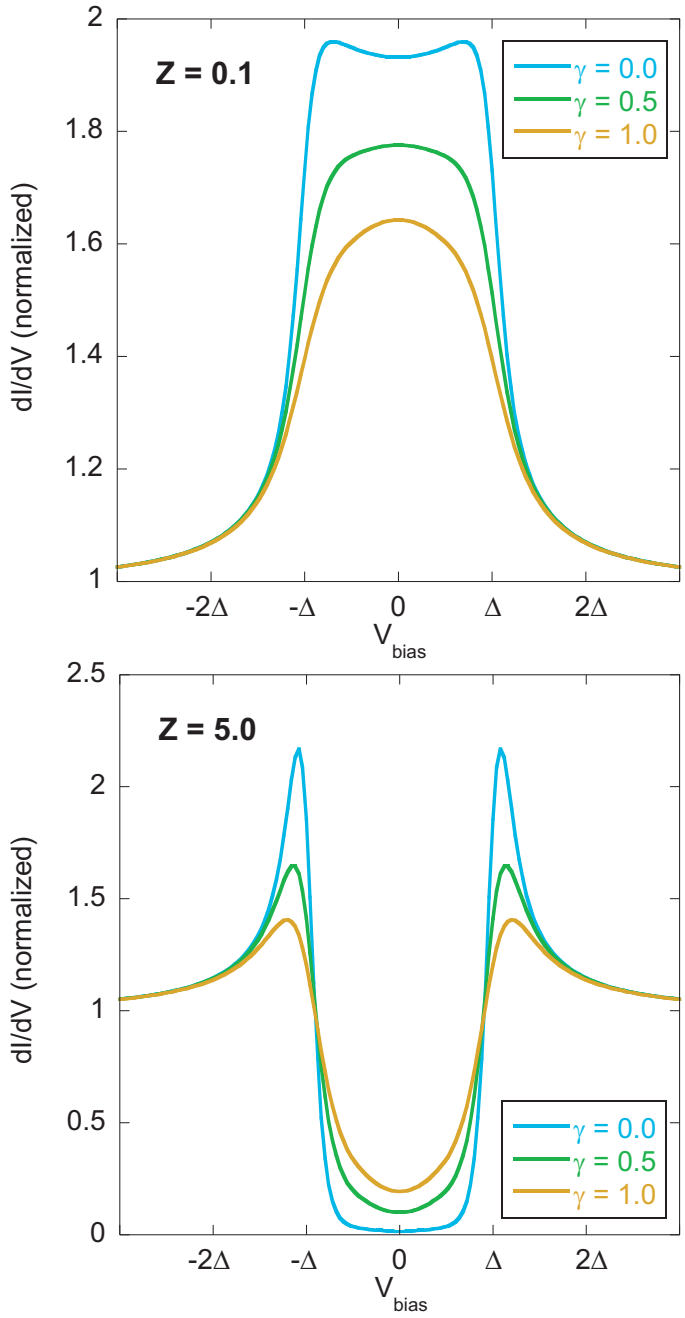

Figure 3.7: Examples of conductance curves showing the effect of increasing Γ for small Z (Andreev limit, above) and large Z (tunneling limit, below) at $T = 4.2$ K with $\Delta = 5$ meV. T_c can be assumed to be large compared to 4.2 K. Temperature only affects the conductance via the Fermi-Dirac term $f(\mathrm{E}) = (\mathrm{e}^{E/kT}+1)^{-1}$ in the BTK theory.

all values of Z and Γ. Also, the magnitude of the gap Δ decreases too as T increases to T_c [5]. Qualitatively this makes sense - the energy gap should disappear when the superconductor undergoes a transition to the normal state. This shrinking of the gap is predicted by the BCS theory, and similar behavior is observed for non-BCS superconductors, and is approximated in equation (3.7) [5] and plotted in the inset of Figure 3.8.

$$\frac{\Delta(T)}{\Delta(T=0)} \approx 1.74(1-\frac{T}{T_C})^{1/2} \tag{3.7}$$

As T is increased beyond T_c, the gap disappears and the conductivity becomes that of the normal state. This background conductivity can be used to normalize lower temperature conductivity curves so that they may be properly fit to BTK curves predicted by equation (3.6).

As I noted above, one can extend the BTK theory to account for pairing symmetries in which $\Delta(E)$ is not constant as a function of angle. The anisotropic s-wave and d-wave symmetries (see Fig. 3.9) can be modeled as follows:

$$\Delta_{s,anis}(E,\theta) = \Delta(E)\cos^4[2(\theta-\alpha)] \tag{3.8}$$

$$\Delta_d(E,\theta) = \Delta(E)\cos[2(\theta-\alpha)] \tag{3.9}$$

The parameter α introduced in Equations (3.8) and (3.9) represents the difference in angle between the a-direction of the crystal lattice of the superconductor and the vector $\mathbf{n}$ that is normal to the N/S interface [41]. In the case of my iron

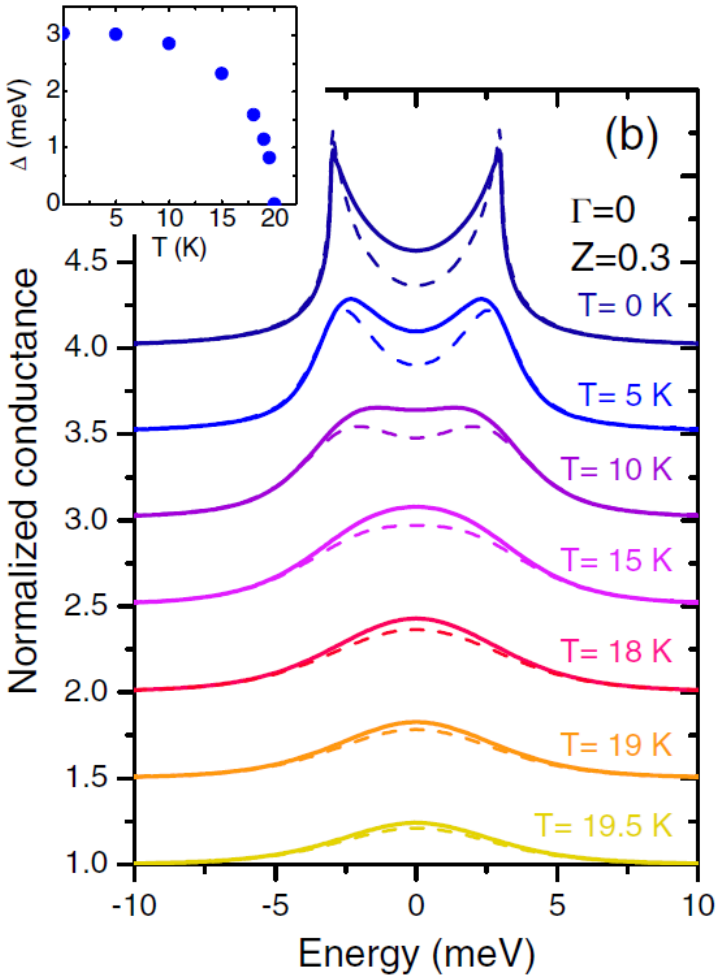

Figure 3.8: Effect of increasing temperature on expected PCS conductivity curves and gap size (inset). From Ref. [41].

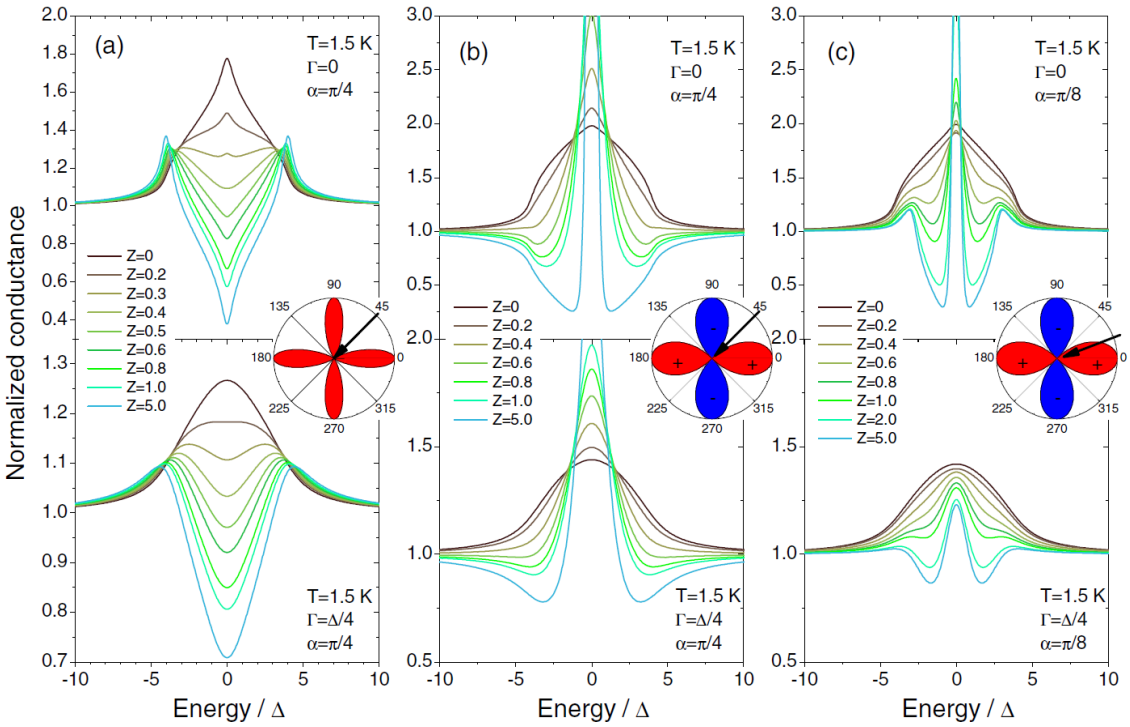

Figure 3.9: Effect of inelastic scattering, barrier height, and tunneling direction on conductance curves with angular dependence taken into account for anisotropic s-wave ($\alpha = \pi/4$, left) and d-wave ($\alpha = \pi/4$, center; and $\alpha = \pi/8$, right). Note that (a) and (b) correspond to current injection in the direction of the nodes in the gap. (From Ref. [41].)

pnictide samples the interface was always parallel the ab-plane (so the normal to the surface was the c-direction) meaning $\alpha = \pi/2$. Figure 3.9 shows a few examples of the effect of including the angular dependence for in anisotropic s-wave or d-wave superconductor.

It should also be noted that Andreev reflection can only be observed when the radius of the N-S junction a is small in comparison to the mean free path l of electrons. Based on the ratio of these two lengths, the behavior of a point-contact junction can be divided into three general regimes.

The ideal case in which $a \ll l$ is known as the ballistic regime because electrons will be accelerated through the contact area without scattering and gain a kinetic energy of eV, where V is the applied voltage. Contacts in which the junction radius is greater than the elastic scattering length, but still less than the diffusion length, are in the diffusive regime. In this regime, elastic scattering occurs inside the junction area, but energy resolution is still possible. The other extreme where $a \gg l$ is known as the thermal regime. In this case, elastic scattering causes energy loss and local heating in the vicinity of the point contact. Figure 3.10 illustrates the differences between these three regimes and the types of scattering observed in each.

For an N-S junction, the energy resolution needed for a successful spectroscopic measurement is possible in both the ballistic and diffusive regimes. Ballistic contacts are preferred, as anomalies in point-contact spectra have been observed for contacts in the diffusive regime. Thus, in general it is desirable to obtain the smallest junction possible for a PCS measurement.

3.3 Point-Contact Spectroscopy: Experimental Setup

There are several variations of the point-contact technique that can be used to create a normal metal-superconductor junction. I used two different methods, known as needle-anvil (NA) and soft point contact (SPC), and each has advantages and disadvantages. With the NA method a sharp normal metal tip is pressed into the sample. The SPC technique uses a small spot of conductive paint or paste on the surface of the SC as the normal metal contact, as described by Daghero *et al.* [101].

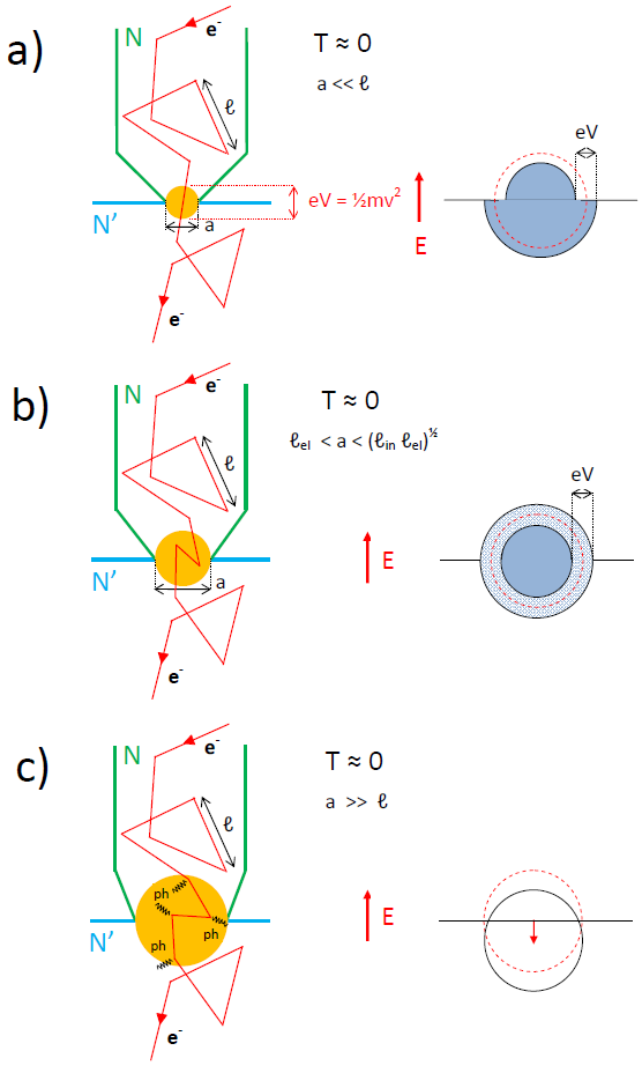

Figure 3.10: Diagrams of point contacts in the (a) ballistic regime, (b) diffusive regime, and (c) thermal regime. In a ballistic contact there is no scattering at the junction, while for diffusive and thermal contacts one observes inelastic and elastic scattering, respectively. The diagrams on the right side indicate how the Fermi surface changes upon application of an electric field for a normal metal-normal metal heterojunction. (From Ref. [101].)

Diagrams of both types of junctions are shown in Figure 3.11.

The needle-anvil technique has the advantage of being adjustable, making it possible to explore a wide range of junction resistances in the same measurement run. On the other hand, the mechanical apparatus required for these measurements can be sensitive to vibrations, and there is evidence that pushing a sharp tip into a sample can create pressure that may affect results (see, for example, Ref. [102]).

The soft point contact method produces junctions that are very mechanically stable and offers greater flexibility in the variety of measurement probes it can be used with. However, soft point contact junctions cannot be adjusted after fabrication, and depending on the fabrication technique the junction size can be larger than those obtained using electrochemically sharpened tips.

The choice of method I used was based on the materials' properties and available equipment. I used the NA technique for the 122 iron pnictide samples because of the adjustability, which allowed for up to five different junction resistances to be measured during each measurement run. Based on the specific probe I used, the lower temperature limit for the NA method is either 4.2 K or 1.7 K, both of which were too high to reach the very low transition temperatures of the superconducting half-Heuslers. Therefore, I used the SPC method for my half-Heusler samples, and cooled them in the ^{3}He insert designed for the PPMS.

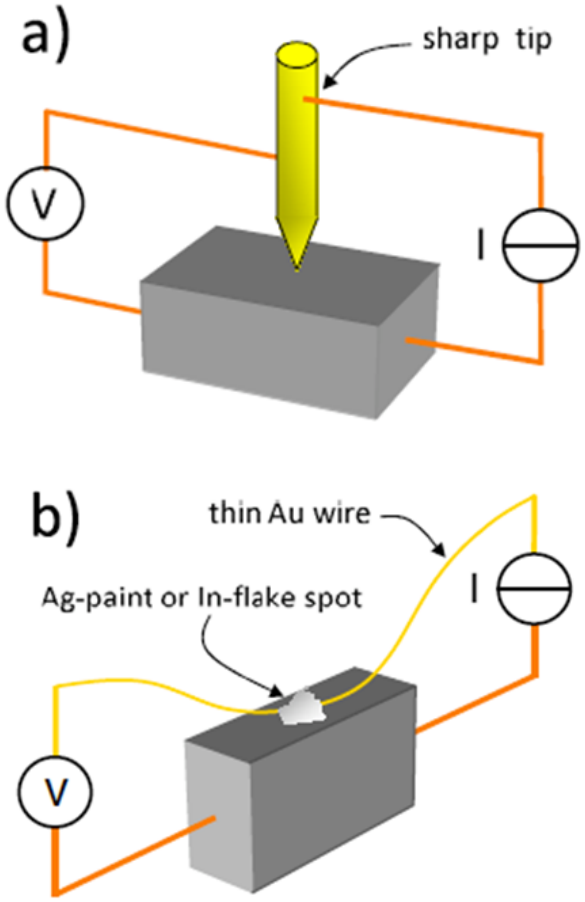

Figure 3.11: a. Needle-anvil point contact junction with a sharp normal metal tip pressed into a superconducting sample. b. Soft point contact junction with a small spot of silver paste forming the normal metal contact. (From Ref. [101].)

3.3.1 Needle-Anvil Method

Needle-anvil point-contact measurements were performed using a specialized probe that allowed for precise control of experimental parameters. This probe was used in conjunction with external voltage and current sources and a cryogenic temperature controller. To create the junction, I first prepared a normal metal tip by using a razor blade to shave either a piece of thick gold wire into a sharp tip or a piece of lead shot into a sharp pyramid. Two copper wires were attached to the tip with DuPont silver paint, and the tip was mounted on a movable stage at one end of the probe. I also soldered wires onto the superconducting sample, which were connected to a breakout box at the room temperature end of the probe. This gave a total of four leads that were connected to the junction (V_+ and I_+ on the tip, V_- and I_- on the sample). A closeup view of the stage end of the probe is shown in Figure 3.12.

A vacuum can was secured over the end of the probe containing the tip and sample and sealed with indium wire. The probe was then inserted into a cryostat and the other end connected to an instrument panel. The system is cooled to 4.2 K by flushing the cryostat with liquid nitrogen, then pushing out the N_2 and filling with liquid He. The stage containing the tip was carefully moved using a system of gears until contact is made with the sample and the junction formed. While moving the tip the voltage between the tip and sample was closely monitored, as a sharp change indicated that contact had been made.

I used a Labview script to collect conductivity data. Fig. 3.13 shows a diagram of the circuit used to adjust the bias voltage and measure conductivity. Two voltage

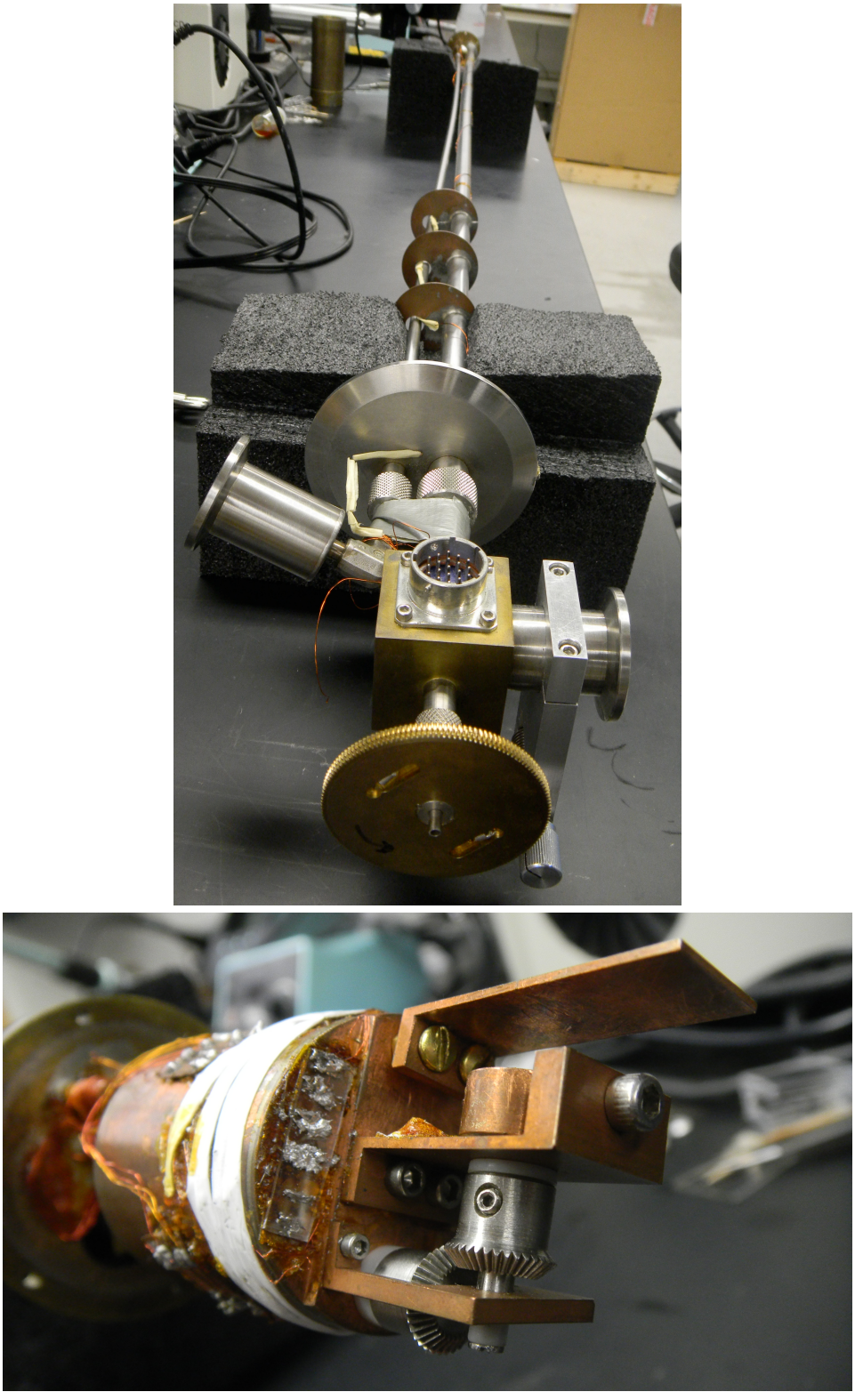

Figure 3.12: Needle-anvil probe used for experiments in Chapter 4 (above) with a close up image of the stage end of the probe showing the gear mechanism that pushes the tip into the sample (below).

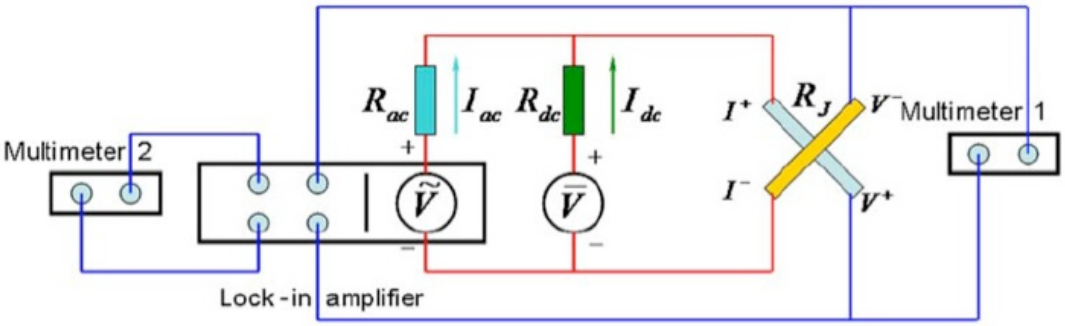

Figure 3.13: Wiring diagram for measuring PCS conductance curves. R_{ac} and R_{dc} are adjustable, and for typical values $R_{ac} \gg R_{dc} \gg R_J$. The junction is represented by the "X" shape labeled as R_J, with the I_- and V_- corresponding to the leads on the tip and I_+ and V_+ to the leads on the superconducting sample.

sources (DC and AC) are connected in parallel with the junction. The DC voltage is used to sweep the bias point, generally from about +50 mV to -50 mV. A lock-in amplifier is then used to superimpose a small AC signal on top of the bias and measure the output, which is proportional to the sample resistance.

A typical measurement run consisted of measuring resistance as a function of bias voltage at a fixed temperature, then precisely increasing the temperature (usually by 1 or 2 K) using a Lakeshore cryogenic temperature controller and repeating the resistance measurement until the temperature exceeded T_c. I then moved the stage to push the tip further into the sample and repeated the measurements. Moving the tip changed both the junction resistance and the effective barrier height, which was useful for verifying that the apparent gap size Δ did not change with increasing Z or R_J.

3.3.2 Soft Point Contact Method

I made soft point contact junctions by first attaching 50 μm gold wires (the V_- and I_- "bottom" electrodes) to the edges of a sample using DuPont 4929N silver conductor paste diluted with paint solvent. Next, I painted a clear epoxy (Stycast 1266 two-part epoxy) over the surface of the crystal, leaving small openings on the order of 0.1 mm in diameter. This was done to prevent the diluted silver paste used for the top wire from wetting the surface so that the contact area between the tip and sample will be as small as possible. Using silver paste in this way requires somewhat delicate control. With this method, the electrically resistive epoxy allows one to use enough paste to ensure that the wire stays in place without all of it coming in contact with the sample

Once the epoxy set, I attached the remaining two electrodes (V_+ and I_+) by making a sharp bend in a length of 25 μm gold wire and adhering it to the exposed sample area with a dilute silver paste solution. The sample was then mounted on a specialized puck for use with the ^{3}He probe designed for a Quantum Design Physical Property Measurement System (PPMS). This particular setup allowed me to use most of the measurement capabilities of the PPMS while also achieving the low temperatures necessary to go below the transition temperatures of the half-Heuslers. Fig. 3.14 shows a soft point contact junction on a sample of $BaFe_{1.9}Pt_{0.1}As_2$ before and after the "top" electrodes were added.

I cooled the samples to temperatures as low as 400 mK with the PPMS ^{3}He option. As with the NA method, I measured conductivity spectra by sweeping a DC

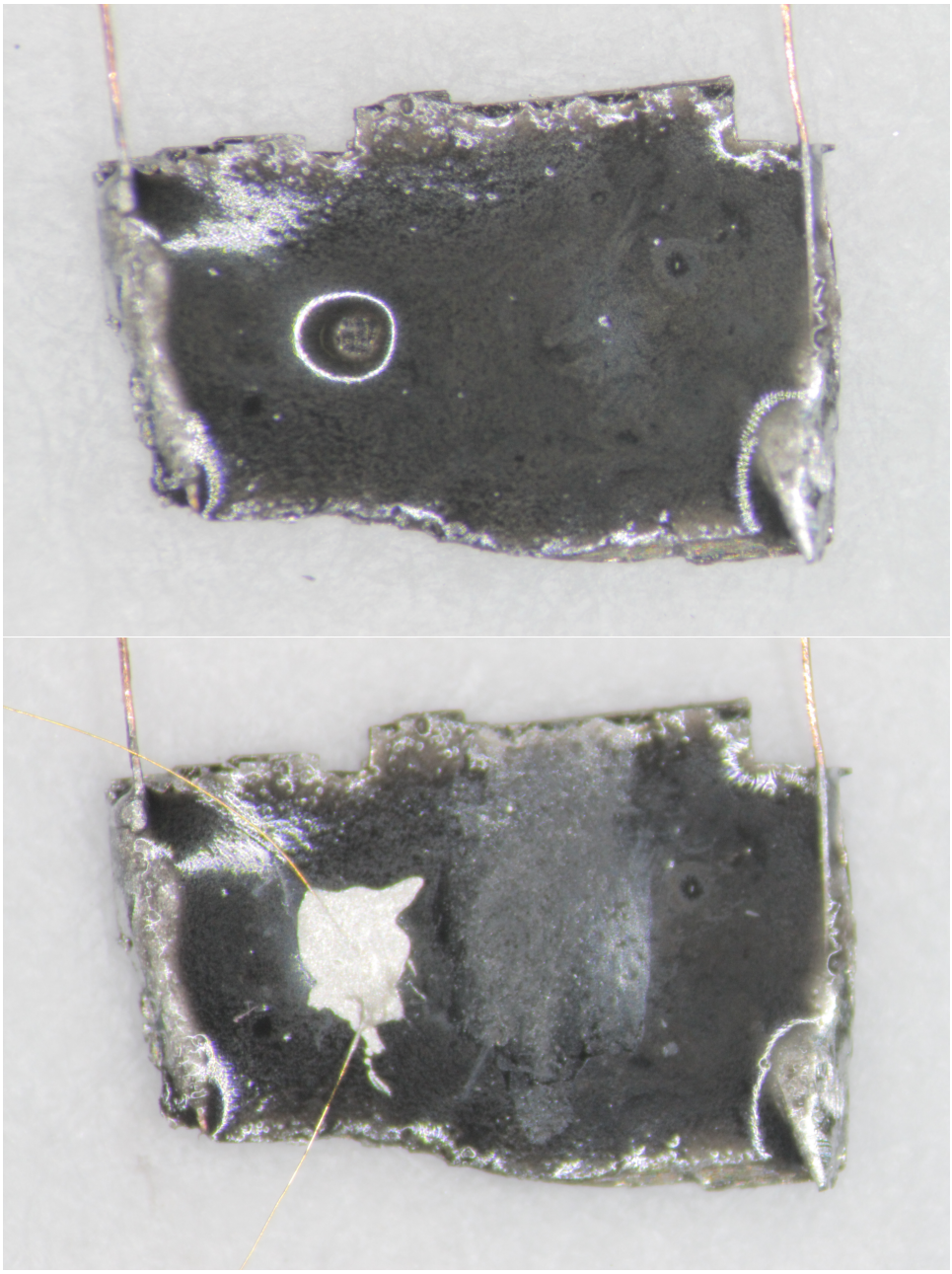

Figure 3.14: Soft point contact junction on a $BaFe_{1.9}Pt_{0.1}As_2$ sample before (above) and after (below) application of top electrodes. The sample was cleaved and the bottom electrodes were soldered onto the edges of the crystal. Epoxy was applied across the surface with a small hole left in the center to ensure a small junction area. Finally, the top wires were applied with silver paint to complete the junction.

bias voltage and using a lock-in amplifier to apply a small AC signal and measure the response at several points. This process was repeated over a range of temperatures and applied magnetic fields up to and above T_c and H_{c2}.

3.4 Point-Contact Spectroscopy: Data Collection and Analysis

Once a measurement was complete, I converted the current vs. voltage curves to normalized conductivity vs. bias voltage. This required the removal of a nontrivial "background" conductivity, which usually persists above T_c (but did not change significantly when temperature was increased further). Since the exact V_{bias} values differed for the dI/dV curves measured at different temperatures, I could not simply subtract the high temperature curve from the low temperature curves. Instead, I fit the background conductivity to a polynomial function. The low temperature conductivity values were divided by their corresponding points on the polynomial fit curve, which removed the curvature resulting from the "background" and yielded normalized conductivity data that approached a value of 1.0 away from zero bias. Once the curves were properly normalized, I calculated the expected conductivity curves such as those in Figures 3.6 through 3.9. I then manually varied the parameters to generate the best fit estimates for the gap size(s), barrier height, and inelastic scattering energy, as well as an assessment of the pairing symmetry of the superconducting order parameter.

Chapter 4: Multi-experimental Study of $BaFe_{1.9}Pt_{0.1}As_2$ Gap Structure

Much of this chapter is based on the published paper by Ziemak *et al.*, Superconductor Science and Technology **28**, 014004 (2014).

4.1 Initial Characterization of Samples

Single crystals of $BaFe_{1.9}Pt_{0.1}As_2$ were grown from prereacted FeAs and PtAs powders and elemental Ba using the FeAs self-flux method [103]. This yielded crystals with typical dimensions $0.1 \times 1 \times 2$ mm^3 (Ref. [14]). Single crystal x-ray diffraction and Rietveld refinement determined the Fe:Pt ratio and the precise composition of $BaFe_{1.906(8)}Pt_{0.094(8)}As_2$. Previous x-ray measurements had shown that Pt substitution reduces the c-axis length and c/a ratio while increasing the a-axis length and unit cell volume compared to pure $BaFe_2As_2$ (Ref. [14]). Characterization by energy- and wavelength-dispersive x-ray spectroscopy verified the same substitutional concentrations across several specimens.

As shown in Fig. 4.1, resistivity measurements exhibited the expected metallic behavior and a sharp transition to the superconducting state with an onset of T_c=23 K and zero resistance achieved by 21.5 K for a transition width of $\Delta T_c < 1.5$ K. No kink

was observable at higher temperatures, which would have indicated a magnetically ordered phase, as seen in the parent compound and underdoped samples. [21, 104]

Figure 4.2 shows a series of resistivity vs. temperature curves for $BaFe_{1.9}Pt_{0.1}As_2$ in a magnetic field of up to 14 T. As field strength is increased, the zero resistivity transition broadens slightly and T_c is significantly decreased, but superconductivity is not fully suppressed. The inset plots the extracted upper critical field as a function of temperature. Magnetic field suppressed T_c to approximately 16 K at 14 T as shown in Fig. 4.2. This is consistent with an upper critical field of approximately 45 T as determined by fits to the Werthamer-Helfand-Hohenberg approximation. [14] However, $H_{c2}(0)$ may be as high as 65 T based on a linear fit to $H_{c2}(T)$, which would be similar to the value found in materials such as $SrFe_{2-x}Ni_xAs_2$ (Ref. [105]).

DC magnetic susceptibitity was measured with field applied along the *ab*-plane, under zero-field-cooled conditions and field cooled with a 1 mT applied field. As shown in the inset in Fig. 4.1, a sharp transition is observed at T_c=23 K into the diamagnetic state with a full-volume shielding fraction observed, as indicated by $4\pi\chi = -1$ by 17 K. Previous specific heat measurements [14] have confirmed the bulk nature of the transition, with a jump in $C_p(T)$ that occurs slightly below T_c. The size of the jump was estimated as $\Delta C_p/T_c \approx 20$ mJ mol^{-1}K^{-1}. Assuming the BCS weak-coupling ratio of $\Delta C_p/\gamma T_c$=1.43 applies, this yields $\gamma = 16(2)$ mJ mol^{-1}K^{-2}. [14].

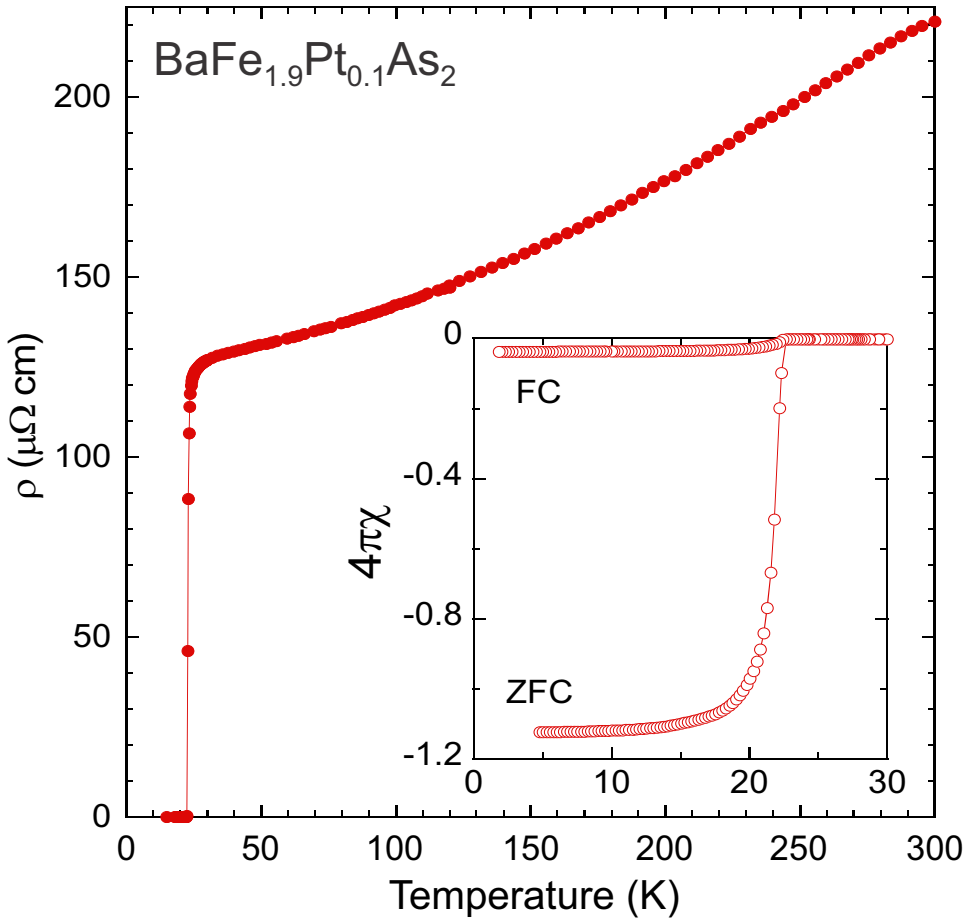

Figure 4.1: Characteristic properties of the superconducting transition in single-crystal samples of $BaFe_{1.9}Pt_{0.1}As_2$ with resistivity (main panel) and magnetic susceptibility (inset) measurements exhibiting sharp transition features consistent with a transition temperature at T_c=23 K, as observed in other bulk measurements. [14] Magnetic susceptibility measurements performed in zero-field-cooled (ZFC) and field-cooled (FC) conditions with a magnetic field of 1 mT indicate a 100% superconducting volume fraction (inset).

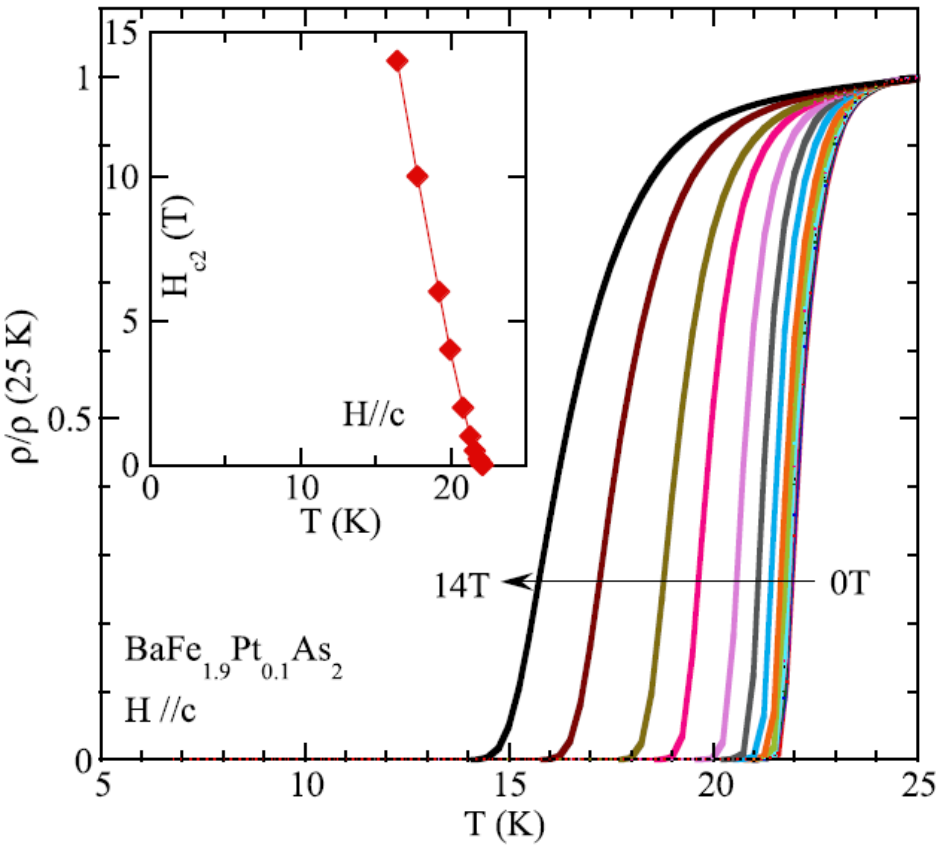

Figure 4.2: Normalized in-plane resistivity of $BaFe_{1.9}Pt_{0.1}As_2$ in magnetic fields (0, 0.01, 0.02, 0.03, 0.04, 0.05, 0.1, 0.2, 0.5, 1, 2, 4, 6, 10, and 14 T in order as indicated by the arrow) applied along the c-direction. Resistivity values are normalized to the 25 K normal state value for clarity. The inset shows the upper critical field H_{c2} as a function of temperature based on the 50% positions of the resistive transitions for each field value from the main figure. (From Ref. [14]).

4.2 Point-Contact Spectroscopy

4.2.1 Measured dI/dV Spectra from Multiple Samples

I performed needle-anvil point-contact measurements on several single crystal $BaFe_{1.9}Pt_{0.1}As_2$ samples using the techniques described in Chapter 3. Electrical contacts consisted of thin Cu wires that I soldered onto the platelet-shaped crystals or attached to the sharpened Pb or Au tips with silver paste.

Conductance spectra were obtained on several crystals from the same synthesis batch. It was necessary to measure multiple samples to ensure that features observed in the spectra were repeatable and not irreproducible artifacts.

For each junction, the normal metal tip was slowly brought closer to the crystal using a gear mechanism until a sharp decrease in resistance indicated that electrical contact had been made between the tip and sample. Next, dI/dV spectra were measured for bias voltages in the $\pm$40-50 mV range to ensure that potential gap features could be detected. The temperature was then increased, and a similar bias voltage sweep was performed at 1-2 K intervals over temperatures ranging from 4 K to roughly 30 K (well above T_c). After recooling to 4 K, the tip was pushed further into the crystal to decrease the junction resistance and the process was repeated. In each individual measurement run, I took data for at least three different tip positions and three different junction resistances. This was necessary to ensure that features in the spectrum could be observed consistently over a range of R_J values.

A sampling of my measured dI/dV curves are shown in Fig. 4.3, presented as

raw data without background normalization but with normalizion to their individual high-bias values (*i.e.* at 40 meV for each curve) in order to account for differences in junction resistance. Disregarding the slight differences in the shape of the curves, which results from differing background or scattering (γ) contributions, each of the dI/dV curves in Fig. 4.3 features a relatively sharp low-bias peak with a width of approximately 2-3 meV, consistent with Andreev reflection in the superconducting state. Furthermore, all curves exhibit depressions or enhancements in conductance at higher energies (*i.e.* 5-6 meV). This overlap is most easily seen in the inset to Fig. 4.3, which presents the same data without vertical offsets.

Figure 4.4 shows the temperature evolution of the PCS conductance for sample S2, with dI/dV normalized to the normal state spectra to remove the background contribution to conductance (c.f. Fig. 4.3). This was done by dividing out a polynomial fit to the dI/dV data measured at 18 K from each temperature data set. Upon cooling below T_c [106], the features described above emerge and evolve with decreasing temperature to reveal a sharp conductance enhancement and a depression at higher bias, suggesting features with at least two energy scales in the order parameter.

4.2.2 Fitting to BTK Model

To better understand the features observed in the conductance spectra, I attempted fitting the Blonder-Tinkham-Klapwijk (BTK) model to my data. The BTK model includes several parameters which I varied to fit my data. [40] As discussed previously, the $I-V$ characteristics of a sufficiently small normal metal-superconductor

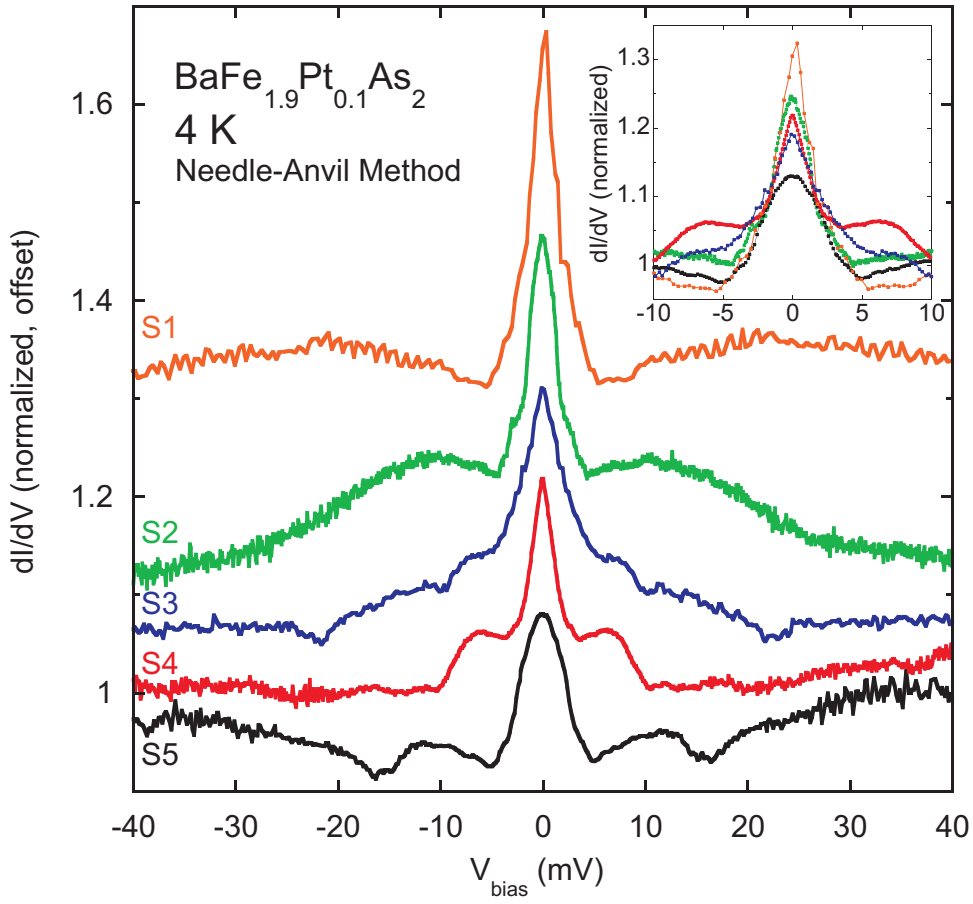

Figure 4.3: Conductance curves obtained from point contact spectroscopy measurements performed on five $BaFe_{1.9}Pt_{0.1}As_2$ samples from the same synthesis batch, offset vertically for clarity. Each has a strong zero bias enhancement of similar width and either a depression or secondary enhancement at higher bias. These curves represent raw data without background subtraction, and each curve is normalized to their high bias values but includes an offset. The inset presents the conductance curves for all five samples plotted without an offset in order to show the overlap of the gross gap features. The green curve (S2) corresponds to the data analyzed in Figs. 4.4 and 4.5.

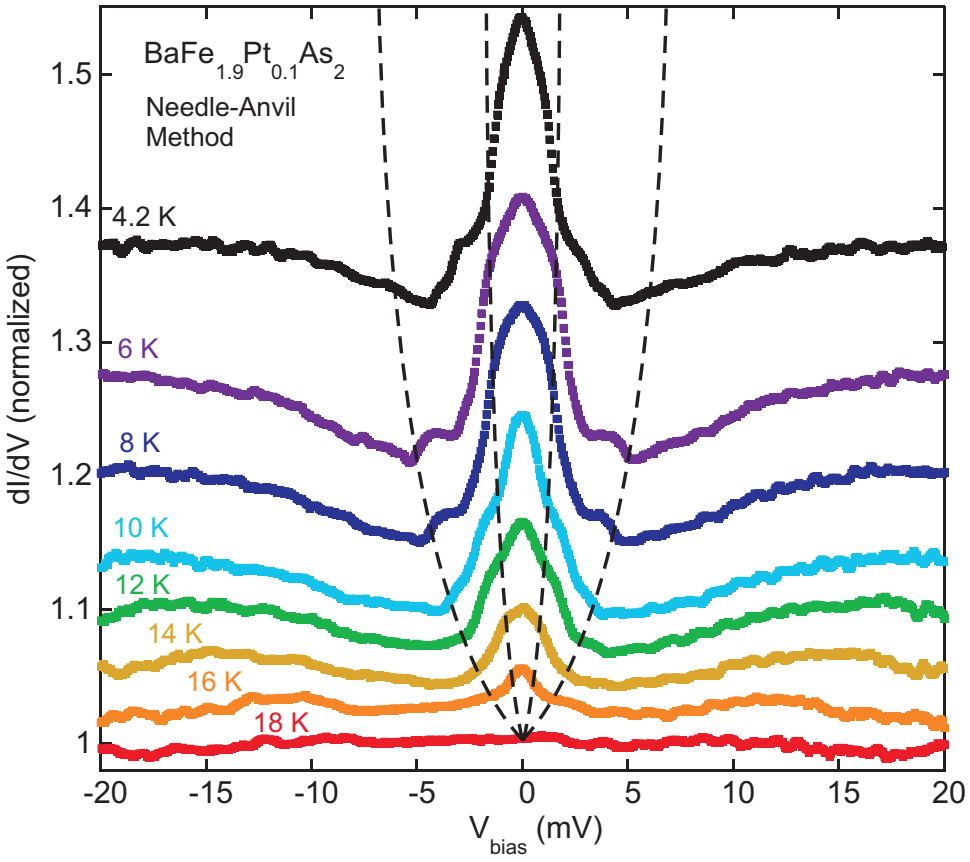

Figure 4.4: Normalized dI/dV spectra over a range of temperatures for single crystal $BaFe_{1.9}Pt_{0.1}As_2$ with high temperature background conductance divided out. Curves are offset for clarity. Dashed curves serve as a guide to the eye to indicate two possible superconducting gap features, the low-bias conductance enhancement and higher bias wells, decrease as expected up to T_c (see text for details).

(N-S) junction are determined by the gap size Δ, a unitless barrier strength Z, the temperature T, and an inelastic scattering energy γ. The value of Z determines the strength of tunneling across the junction: $Z = 0$ indicates complete Andreev reflection, while $Z \to \infty$ indicates the weak tunneling limit. In the low-Z case, the dI/dV vs. V_{bias} curve contains a peak at zero bias extending out to bias voltages corresponding to approximately $+\Delta$ and -Δ, whereas for large Z, dI/dV is suppressed at zero bias with enhancements at $\pm\Delta$ due to quasiparticle tunneling. The γ term affects the shape of the dI/dV curves and is critical in obtaining a good fit to measured data. In the case of a two-gap BTK model, the fit parameters include two gap sizes, Δ_1 and Δ_2, two barrier strengths, Z_1 and Z_2, two scattering energies, γ_1 and γ_2, and an additional weight factor w, which indicates the proportion of electrons incident on the barrier that interact with either gap. The composite two-gap BTK curve is simply a weighted average of two single-gap curves.

It should be noted that the fits I obtained were not true least-squares statistical fits. Rather, the fitting process was done by manually adjusting the parameters until the agreement appeared to be good to my eye. Due to the large number of parameters involved, particularly for a two-gap fit, a proper least-squares fit would be quite difficult to converge because of the time required to generate even a single BTK curve.

Figure 4.5 shows the best fit that I obtained for the normalized dI/dV curved labelled as sample S2 in Figure 4.3. The black points represent my data, while the blue curve corresponds to the two-gap isotropic s-wave BTK fit. I made several attempts to obtain a single-gap s-wave fit. While a single-gap model can be matched

relatively well to the central zero bias peak, in each case it failed to account for the sharp dips closer to 5 meV. In contrast, the double gap fit was much more successful at reproducing the measured data, matching both the wells and zero bias peak in amplitude and energy scale.

I conclude, therefore, that the two-gap nodeless s-wave model more accurately describes the conductance observed via PCS. The fit assumed the existence of a nodeless gap with energy $\Delta_1 = 2.5$ meV, while the high bias depression was well modeled by including a second gap of magnitude $\Delta_2 = 7.0$ meV. These features are strikingly similar to those observed in PCS measurements performed on the two-gap superconductor MgB_2, which also exhibit peak-dip features that were understood in terms of a two-gap scenario with similar gap energies (but of course a much higher T_c of 40 K). [107]

4.2.3 Discussion of Fit Parameters

Interestingly, I found that the best fit values for Z and γ depended on the gap. For instance, the parameter set for the smaller gap spectrum (Δ_1= 2.5 meV, Z_1 = 0, γ_1 = 1.0 meV) indicated complete Andreev reflection with little broadening. In contrast, the larger gap spectrum ($\Delta_2 = 7.0$ meV , $Z_2 = 7.0$, $\gamma_2 = 7.0$ meV) appeared closer to the tunneling limit with a larger Z and much greater broadening. The weight factor of w=0.6 indicated comparable amounts of Andreev reflection and tunneling into each gap with more conduction for the smaller gap.

While it is not clear why such significant differences were observed in the mod-

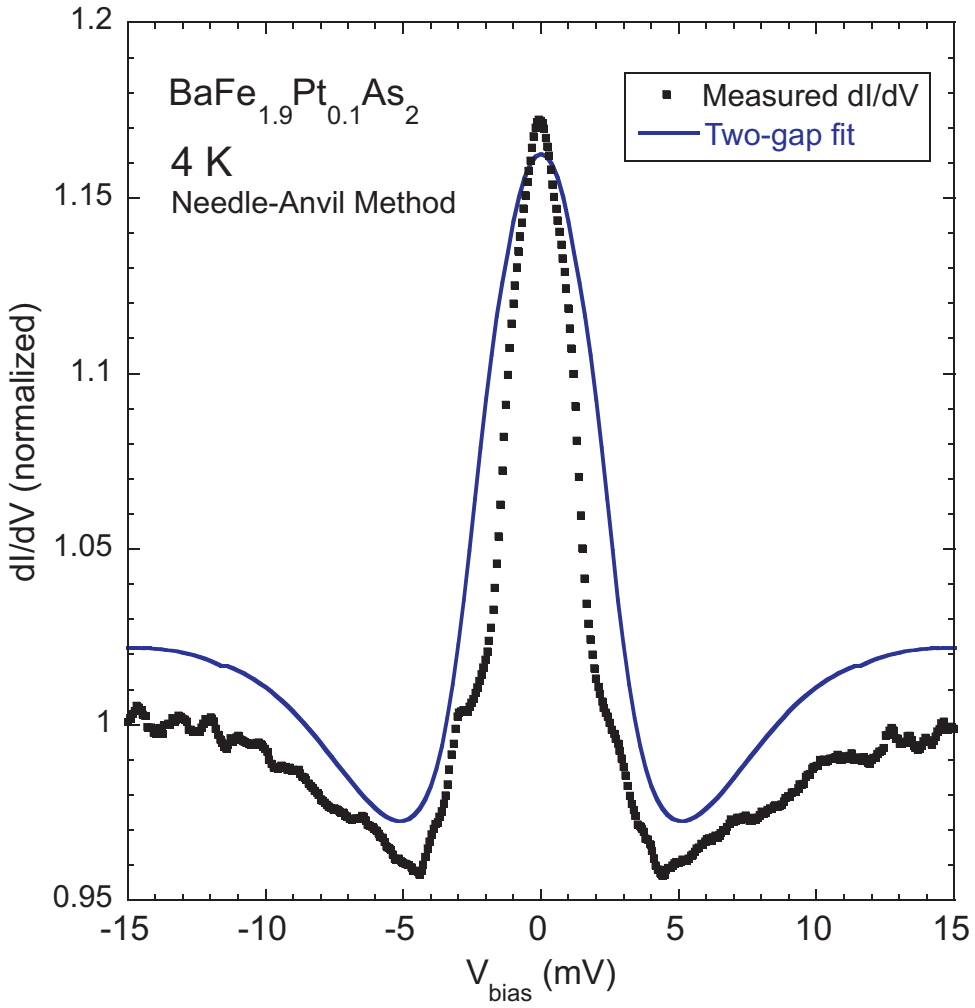

Figure 4.5: Point contact conductance spectrum of $BaFe_{1.9}Pt_{0.1}As_2$ sample S2, at 4.2 K, normalized to remove the normal state background conductance (black points). The blue curve shows the fit to an isotropic s-wave two-gap Blonder-Tinkham-Klapwijk model, yielding Δ_1= 2.5 meV, Z_1 = 0, γ_1 = 1.0 meV for the smaller gap and Δ_2 = 7.0 meV , Z_2 = 7.0, γ_2 = 7.0 meV for the larger gap, with a weighting factor of w=0.6.

eled barrier heights and scattering strengths of the two gaps, such differences are not unprecedented. For example, a two-gap model whose larger gap also had a larger Z was observed in $Ba_{1-x}K_xFe_2As_2$ [42]. The unusually large scattering strength deduced from the fit to BTK for the larger gap, with $\gamma_2 \simeq \Delta_2$, is also unusual. However, a high quasiparticle scattering rate has also been deduced from pair-breaking experiments. [49,108] For example, Kirshenbaum *et al.* investigated pair-breaking scattering in a range of 122 iron pnictide materials with transition metal substitutions at the Fe site. [108] From their observations one can estimate the transport scattering rate of $\Gamma \simeq 2.5 \times 10^{13}$ s^{-1} for $BaFe_{1.9}Pt_{0.1}As_2$ based on a T_c value of 23 K. This translates to an energy scale of $\hbar\Gamma \approx 16$ meV, which is actually higher but of the same order of magnitude as γ_2, suggesting strong scattering in the FeSC materials [108].

Alternatively, the contrast between Z_1 and Z_2 may be due to a relatively large "impedance mismatch" between the tip and the large-gap band than for the small-gap band. Thermal conductivity measurements on LiFeAs [49] also indicate the possibility of a mismatch in Fermi velocities, so it is possible that my observation of this large contrast in Z values are valid.

Finally, the appearance of spectral features at energy scales much larger than the predicted weak-coupling BCS gap value for a 23 K superconductor, $\Delta_{BCS} = 1.76k_BT_c = 3.5$ meV, is puzzling but also not unprecedented in tunneling and PCS studies. For normal metal-superconductor junctions outside the ballistic limit, it has been shown that sharp dips can occur at higher bias voltage. [109] A conservative estimate gives an electron mean free path on the order of nanometers, [110] which would place my micron-size junctions (assuming a perfect and full contact) in the

diffusive rather than ballistic regime, and outside the Sharvin limit. However, as evidenced in Fig. 4.3 my spectra exhibit features at higher bias voltages, including both gap-like dips and Andreev-like shoulders.

I note that many other PCS experiments have observed dominant spectral features in a lower-energy range consistent with our prominent features near Δ_1. For example, $BaFe_{1.86}Co_{0.14}As_2$ [42] and several 122's exhibit $2\Delta/k_BT_c \simeq 3.1$ [111]. Data from the latter study are presented in Fig. 4.6 for multiple concentrations of $Ba_{1-x}K_xFe_2As_2$. These dI/dV curves were fitted to a single gap BTK fit, which provides a useful contrast to the two-gap spectra observed for $BaFe_{1.9}Pt_{0.1}As_2$. In the case of LiFeAs, observations of a small gap of 1.6 meV ($2\Delta/k_BT_c = 2.2$) have been reported from PCS measurements using Pb and Au tips [112]. They do not observe features associated with any larger gap, such as seen in ARPES experiments. [113, 114] However, other studies have revealed prominent two-gap features, such as in $Ba_{0.55}K_{0.45}Fe_2As_2$ [42, 43] and $BaFe_{2-x}Ni_xAs_2$ up to x = 0.10 [44]. Furthermore, a wide range of scanning tunneling spectroscopy experiments have observed superconducting gap magnitudes indicative of strong coupling, with $2\Delta/k_BT_c$ ratios far above the BCS weak-coupling expectation of 3.5 [115]. For example, optimally doped $BaFe_{2-x}Co_xAs_2$ shows a superconducting tunneling gap with coherence peaks corresponding to a much larger (average) single-gap value of $\Delta = 6.25$ meV, corresponding to $2\Delta/k_BT_c = 5.73$ [116].

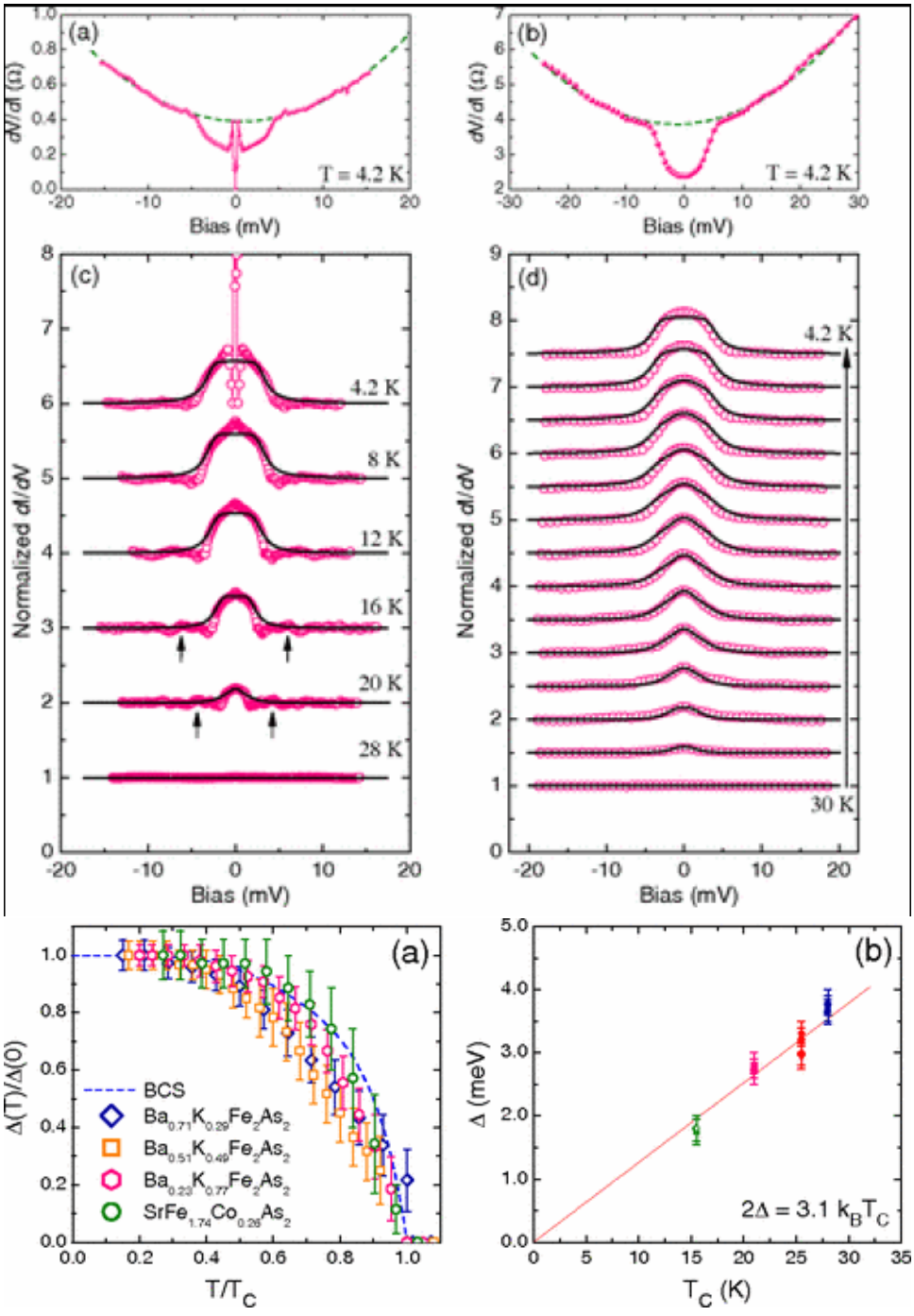

Figure 4.6: Needle-anvil point-contact spectra for $Ba_{0.51}K_{0.49}Fe_2As_2$ (top left) and $Ba_{0.71}K_{0.29}Fe_2As_2$ (top right) showing normalized dI/dV spectra overlaid with BTK fits. These single-gap spectra are clearly different in form than the two-gap spectra I observed for $BaFe_{1.9}Pt_{0.1}As_2$. The lower figure shows the normalized gap extracted from BTK fits plotted against temperature (bottom left) and Δ vs. T_c for four different compounds (bottom right) demonstrating $2\Delta/k_BT_c \simeq 3.1$ for these iron pnictide materials. From Ref. [111]

4.3 Other Thermodynamic and Spectroscopic Measurements

4.3.1 Thermal Conductivity

All thermal conductivity data I discuss in this section was measured at Université de Sherbrooke in Quebec, Canada by Kevin Kirshenbaum and the group of Dr. Louis Taillefer.

Thermal conductivity was measured using a one-heater, two-thermometer steady state technique, as a function of temperature, to 60 mK in a dilution refrigerator. Temperature sweeps were repeated for fixed magnetic fields from 0 T to 15 T, in both parallel ($H \parallel ab$) and perpendicular ($H \parallel c$) orientations with respect to the crystallographic basal plane. Measured κ/T vs. T are shown in Fig. 4.6, along with fits to $\kappa/T = a + bT^{\alpha-1}$. Extrapolating to the $T \to 0$ limit, one obtaines the residual electronic term $a = \kappa_0/T$.

The residual electronic contribution $a = \kappa_0/T$ clearly approaches a value of zero as $T \to 0$, indicating no zero energy quasiparticles in the superconducting state. The fitted value of κ_0/T is actually slightly negative, but is within experimental error of zero. For comparison, in the $T \to 0$ limit one can calculate the electronic contribution to thermal conductivity from the Wiedemann-Franz law, $\kappa_0/T = L_0/\rho_0$, where $L_0 = (\pi^2/3)(k_B/e)^2 = 2.44\times10^{-8}$ W Ω K^{-2}. Using a fictitious residual zero-temperature resistivity value of ρ_0=125 $\mu\Omega$ cm based on extrapolating the zero-field data (c.f. Fig. 4.1) yields an approximate value of L_0/ρ_0=0.195 mW K^{-2} cm^{-1}, shown in Fig. 4.7 as blue diamonds on the T=0 axis. As evident in Fig. 4.6, this estimated normal state

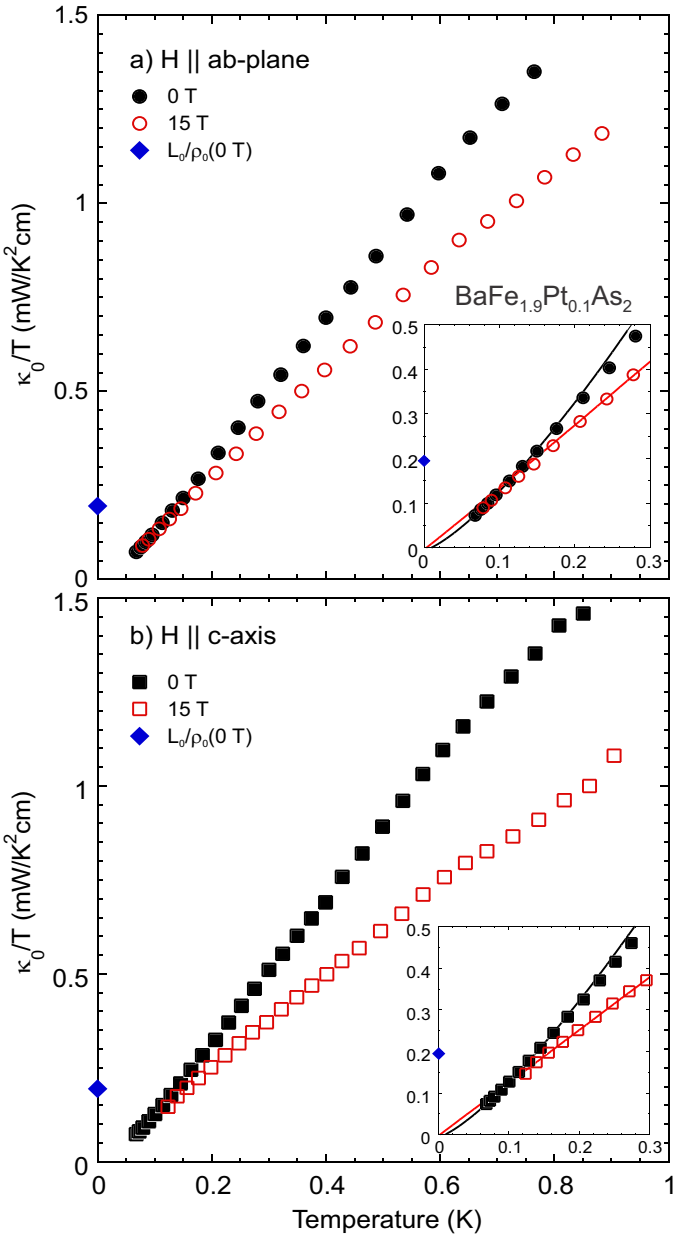

Figure 4.7: (a) Low temperature thermal conductivity of a crystal of $BaFe_{1.9}Pt_{0.1}As_2$ measured in zero (black, closed symbols) and 15 T (red, open symbols) applied magnetic fields, oriented along the crystallographic *ab* basal plane (circles) and (b) the *c*-axis (squares). Zero field measurements were repeated in each orientation using the same crystal for direct comparison. Insets show a detailed view of the low-temperature data, with solid lines representing power law fits to $\kappa/T = a + bT^{\alpha-1}$ below 150 mK. Blue diamonds in all panels represent the normal state electronic thermal conductivity estimated using the Wiedemann-Franz law.

limit is many orders of magnitude larger than the maximum possible extrapolated value of κ_0/T allowed by error, suggesting a fully gapped superconducting order parameter with no nodes or deep minima. This is to be contrasted with the finite κ_0/T expected for superconductors with either symmetry-imposed or accidental nodes in the gap, such as observed in the d-wave superconductor $Tl_2Ba_2CuO_{6+\delta}$ (Tl-2201) [46] or in c-axis transport measurements of $BaFe_{2-x}Co_xAs_2$ away from optimal doping [47], respectively.

The absence of low-energy excitations is also evident in magnetic field measurements up to 15 T, or approximately 25% of H_{c0}. Figure 4.7(a) and (b) show κ/T vs. T for both $H \parallel ab$ and $H \parallel c$ orientations, respectively. Figure 4.8 shows κ_0/T as a function of field for several materials. Single-gap isotropic s-wave superconductors at $T = 0$ such as Nb [117] do not possess quasiparticles until the magnetic field becomes so large that vortex core bound states begin to delocalize. This process proceeds exponentially with the ratio of intervortex spacing to coherence length (or essentially the magnitude of magnetic field) up to the uppper critical field. Multiband s-wave superconductors such as $NbSe_2$ also have $\kappa_0/T = 0$ in zero field due to lack of nodes in the gap structure. However, vortex core delocalization can be accelerated in a multi-band superconductor due to a reduced gap magnitude on one or more bands. This can produce an onset of low-energy excitations and a finite and increasing value of κ_0/T at fields much smaller than H_{c2}. [50].

Figure 4.8 (a) shows the evolution of κ_0/T with magnetic field in $BaFe_{1.9}Pt_{0.1}As_2$ and other superconductors. Figure 4.8 (b) shows the behavior observed in the FeSC family. The lack of absence of a residual term in $BaFe_{1.9}Pt_{0.1}As_2$ is clear: the evolu-

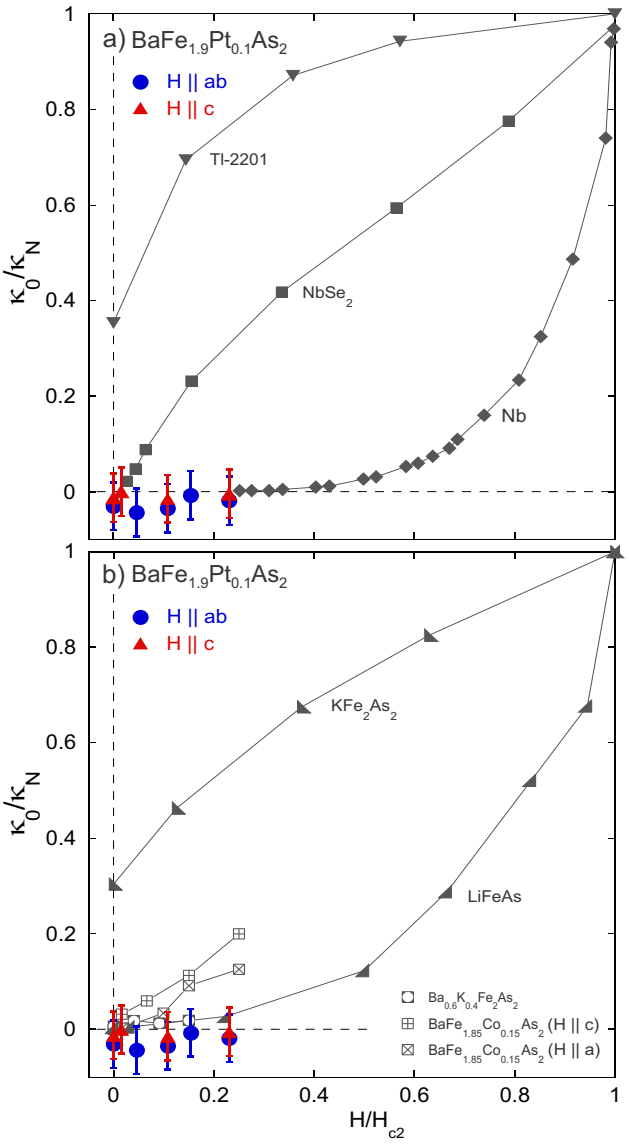

Figure 4.8: (a) Residual thermal conductivity κ_0/T of $BaFe_{1.9}Pt_{0.1}As_2$ extracted from temperature sweep measurements and normalized to the normal state conductivity κ_N/T, plotted as a function of reduced magnetic field and compared to several characteristic superconductors. The lack of increase in κ_0/κ_N in $BaFe_{1.9}Pt_{0.1}As_2$ is comparable to the behavior of isotropic, single-gapped s-wave superconductors such as elemental Nb [117] that exhibit an exponentially slow activated increase with field, and is in contrast to the cases for multi-band s-wave superconductor $NbSe_2$ [50] and d-wave nodal superconductor $Tl_2Ba_2CuO_{6+\delta}$ [46], which exhibit a much faster rise with field due to nodal or small-gap low energy quasiparticle excitations. (b) Comparison of κ_0/T in $BaFe_{1.9}Pt_{0.1}As_2$ to that in a range of iron-based superconductors including KFe_2As_2 [118], $Ba_{0.6}K_{0.4}Fe_2As_2$ [118], $BaFe_{1.85}Co_{0.15}As_2$ [47], and LiFeAs [49].

tion in $BaFe_{1.9}Pt_{0.1}As_2$ is comparable to that of elemental Nb [117]. This is in stark contrast to that of the *d*-wave and multiband *s*-wave superconductors Tl-2201 and $NbSe_2$, respectively. Within the FeSC family, such a flat response is not unprecedented. In fact it it what one expects for a fully isotropic *s*-wave gap, as deduced for both $Ba_{0.6}K_{0.4}Fe_2As_2$ [118] and LiFeAs [49].

In a multi-band scenario, which is the case for $BaFe_{1.9}Pt_{0.1}As_2$ as measured by ARPES (see Sect. 4.3.2), the suppression of the maximum energy gap on portions of the band structure can lead to an enhancement of tunneling between vortex core bound states, resulting in an effectively reduced critical field for those portions. In the case of $NbSe_2$, this field scale is identified with a shoulder in $\kappa_0/\kappa_N(H)$ near $H^* \sim H_{c2}/9$. This is consistent with an energy gap ratio $\Delta_{min}/\Delta_{max} \simeq 1/3$ since $H_{c2} \propto \Delta^2$ [50]. In contrast, in $BaFe_{1.9}Pt_{0.1}As_2$ the lack of a rise in $\kappa_0/\kappa_N(H)$ up to $H_{c2}/4$ suggests little if any anisotropy in the gap. However, as with LiFeAs [49], the lack of a rise in $\kappa_0/\kappa_N(H)$ does not rule out the existence of a smaller gap in the band structure: it may be that the conductivity contribution of the small-gap Fermi surface is much smaller that that of the large-gap component, or if coherence lengths are comparable due to scaling of Fermi velocities (*i.e.* since $\xi_0 \sim v_F/\Delta$).

LiFeAs is relevant to $BaFe_{1.9}Pt_{0.1}As_2$ because recent ARPES experiments on LiFeAs show two gap magnitudes of approximately 2-3 meV and 5-6 meV [113, 114, 119]. The observed anisotropies are weak, with gap minima not reaching below ~2 meV. $BaFe_{1.9}Pt_{0.1}As_2$ may be similar, or have similar coherence lengths across bands, making it difficult to determine the gap anisotropy via thermal conductivity.

4.3.2 Angle-Resolved Photoemission Spectroscopy

ARPES allows the measurement of electronic structure of materials and characterization of the order parameter of the superconductor. If suitably clean surfaces can be prepared, ARPES can be particularly useful for identifying and characterizing the momentum-resolved energy scales of the gap function $\Delta(\mathbf{k})$ and elucidating the gap structure of multi-band superconductors. The ARPES data I discuss in this section was measured at the Leibniz Institute for Solid State and Materials Research (IFW) in Dredsen, Germany by the group of Dr. Sergey Borisenko.

ARPES was performed on clean $BaFe_{1.9}Pt_{0.1}As_2$ sample surfaces, which were cleaved in high vacuum at low temperatures, exposing mirror-like surfaces. Figure 4.9(a) shows the resulting Fermi surface map of $BaFe_{1.9}Pt_{0.1}As_2$. There is a large electron pocket at the X point and a smaller hole pocket at the Γ point. This is similar to other electron-doped 122 FeSCs [120]. Energy-momentum cuts presented in Figs. 4.9(b) and (c) show occupied bands above and below T_c. Figures 4.9(d)-(g) show the corresponding energy distribution curves (EDCs). The EDC curves show a clear peak, consistent with a gap opening below approximately 17 K in both the electron and hole pockets. For example, upon cooling below T_c a sharp coherence peak and gap at the Fermi energy are clearly seen in the EDC curve in Fig. 4.9(d). The width of these features corresponds to approximately a 3 meV gap, consistent with the small gap size Δ_1 that I extracted from fits of the point contact spectroscopy data (see Sect. 4.2).

Integrated energy distribution curves (IEDCs) were also recorded at different

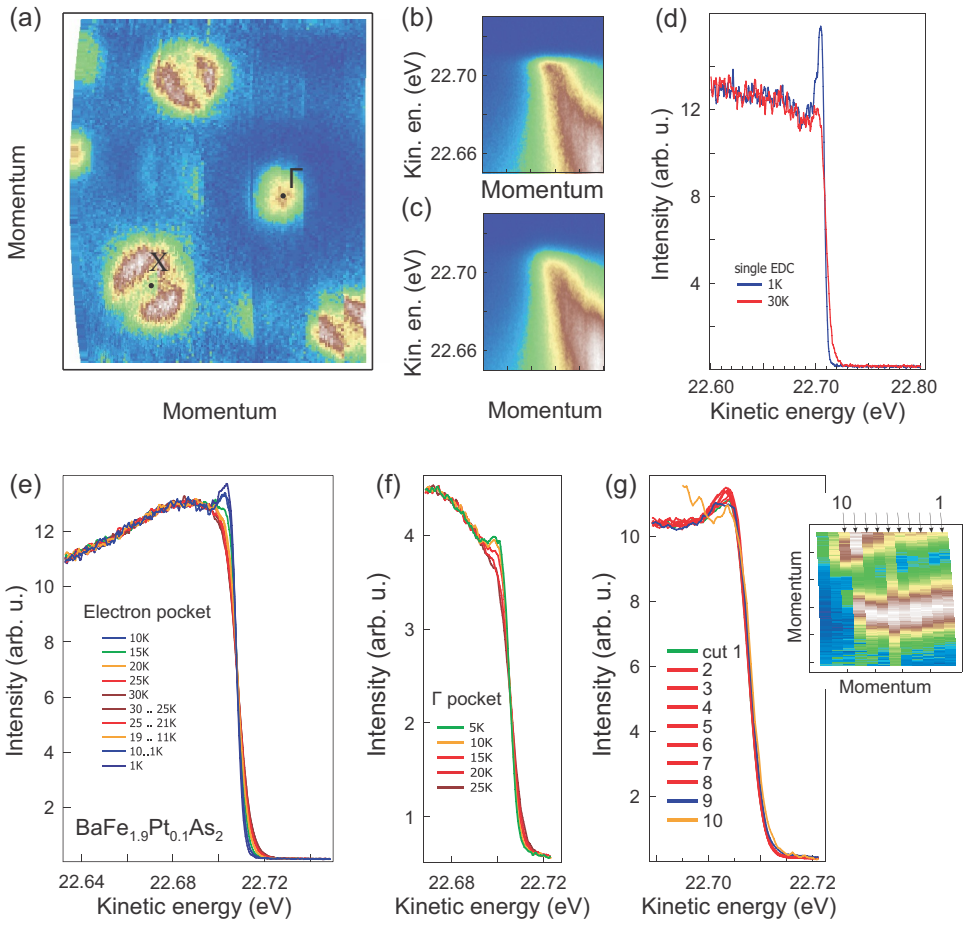

Figure 4.9: ARPES measurements of $BaFe_{1.9}Pt_{0.1}As_2$. (a) Fermi surface map, revealing large electron-like pockets around Brillouin zone corner and small hole-like pockets at center. (b) Energy-momentum cut, passing through the electron pocket recorded below T_c. (c) Same cut, recorded above T_c. (d) Single energy distribution curve (EDC) recorded above and below T_c shows appearance of a sharp peak in the superconducting state. (e) Temperature dependence of the integrated EDC (IEDC) recorded from electron pocket for heating up to 30 K and cooling down to 1 K. (f) Temperature dependence of the IEDC for hole pocket. (g) IEDC recorded from different parts of the electron pocket. Positions of cuts are indicated in the mini-map in inset.

positions along the electron pocket, as shown in Fig. 4.9(g). Each IEDC has a peak of approximately the same width, confirming that the observed electron pocket gap is isotropic. This behavior is similar to several other 122 FeSCs including optimally doped $Ba_{1-x}K_xFe_2PtAs_2$ [121], $BaFe_{2-x}Co_xAs_2$ [51] and LiFeAs [119], which all show multiple gap sizes with little or no anisotropy.

4.3.3 Raman Spectroscopy

All Raman spectroscopy data for this work was obtained by the group of Dr. Girsh Blumberg at Rutgers University.

Raman spectra were obtained using a Kr+ laser with 647 and 476 nm wavelengths 1.2 to 12 mW of incident laser power was focused to a spot of 50×100 μm^2 on the freshly cleaved *ab*-plane crystal surface. The backscattered light was collected close to the backscattered geometry was focused onto 100×240 μm^2 entrance slits of a custom triple-stage spectrometer equipped with 1800 lines/mm gratings. To obtain symmetry-resolved Raman spectra of $BaFe_{1.9}Pt_{0.1}As_2$, the Rutgers group employed both linearly- and circularly-polarized light. [53] Data were collected from 14 total samples at 3 and 30 K. The estimated local heating in the laser spot did not exceed 4 K for laser power less than 2 mW.

Figure 4.10 shows examples of the raw Raman data, $d\sigma(\omega)/d\omega$, normalized to the power and laser frequency in the B_{2g} channel. The plot illustrates the importance of measuring the normal state response and highlights the contribution of the major superconducting phase to the Raman response. I also note that the

residual flux gives rise to a related, large background of laser-induced luminescence. The magnitude of this background luminescence (bottom arrow) sets the minimum polarization contribution for each measured polarization. This background contribution is not related to Raman scattering and must be subracted before $d\sigma(\omega)/d\omega$ can be converted into the Raman response. The final spectra are calculated as $\chi'' = (d\sigma(\omega)/d\omega - BG)(n(\omega,T)+1)$, where $n(\omega)$ is the Bose factor. The resulting response is further decomposed into contributions from the major superconducting phase and impurity phase(s). These potential impurity phases may not be superconducting or may simply have a much lower T_c. Based on the flattened section of the experimental data (from the cutoff near 10 cm^{-1} to roughly 25 cm^{-1}) at 3 K and general flattened response at 30 K, we assumed that contributions from any impurity phase(s) were well approximated by a constant, much like the luminescence term. To summarize, the total background (BG) gapping B_{2g} was removed and $d\sigma(\omega)/d\omega$ is converted to the Raman response, $\chi''_{major} = (d\sigma(\omega)/d\omega - BG)(n(\omega,T)+1)$.

The normal state response (red curve in Fig. 410) was essentially flat down to the cutoff value of the spectrometer. The superconducting response (blue curve) exhibited a broad peak around 80-90 cm^{-1}. This feature was clearly seen in previous Raman studies [53, 122, 123] as well as a threshold near 45 cm^{-1}, marked by a black dashed line in Fig. 4.10. The response flattens out below approximately 25 cm^{-1}. The flattened background (uppermost black dashed line) is likely a result of sample impurity content. All 14 samples showed non-vanishing backgrounds with amplitude depending on spot position within the cleave and laser excitation wavelength.

Here we focus on properties of the major superconducting phase and attempt

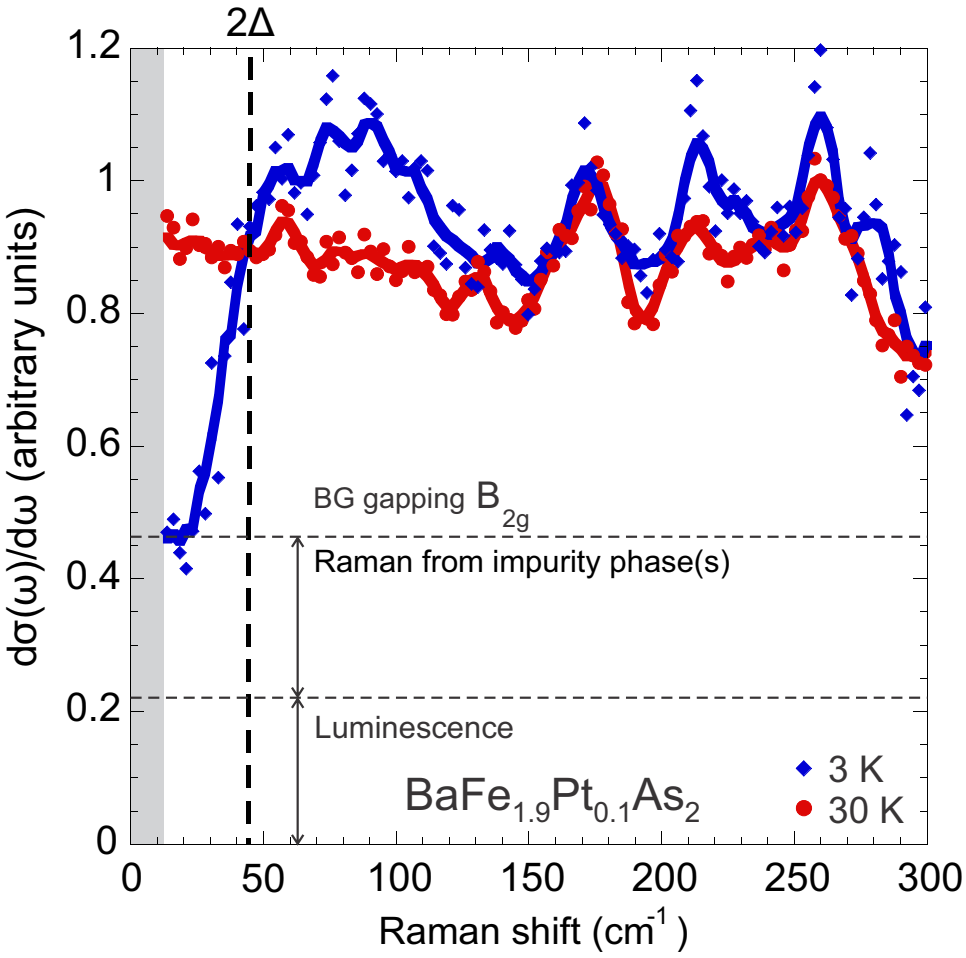

Figure 4.10: Raw measured data, containing contributions from both Raman and luminescence channels, for sample S3, obtained with laser excitation of 467 nm. Blue diamonds represent data at 3 K, while red circles represent 30 K data. The superconducting gap is indicated by the vertical dashed line labeled 2Δ. Note that the gray area indicates energies below the cutoff range of the spectrometer.

to remove the contributions from impurity phases. The measured electronic Raman response $\chi''(\omega)$ in the B_{2g} and A_{1g} channels is shown in Figs. 4.11(a) and (b), respectively. The data in the SC state exhibit a threshold around 45-50 cm^{-1} (vertical black dashed line, labelled as 2Δ), clearly seen in both B_{2g} and A_{1g} polarizations. This is the gap, also seen in ARPES and point-contact spectroscopy. The value $\Delta = 3 \pm 0.3$ meV was confirmed for multiple $BaFe_{1.9}Pt_{0.1}As_2$ samples.

4.4 Discussion

To understand all of these results it is instructive to review the conclusions drawn from similar experiments on Co-substituted $BaFe_2As_2$. Results from multiple studies on optimally doped $BaFe_{2-x}Co_xAs_2$ tend to confirm a similar nodeless gap structure. Comprehensive analysis of the phase diagram by Reid *et al.* [47] looked at the evolution of the gap structure with increasing Co concentration based on thermal conductivity. Based on the presence or absence of residual thermal conductivity κ_0/T and its evolution in field, it was argued that line nodes are present in under- and overdoped $BaFe_{2-x}Co_xAs_2$ but that optimally doped $x = 0.148$ samples were nodeless.

Daghero *et al.* measured several PCS spectra for overdoped samples with $x = 0.2$ [41]. Current was injected in the *ab*-plane and parallel to the *c*-direction using the soft point-contact method. Fitting to BTK theory showed better agreement for a two-gap isotropic *s*-wave model than for a single nodeless gap. The estimated gap values were $\Delta_1 = 3.8$-5.2 meV and $\Delta_2 = 8.2$-10.9 meV. The authors also reported

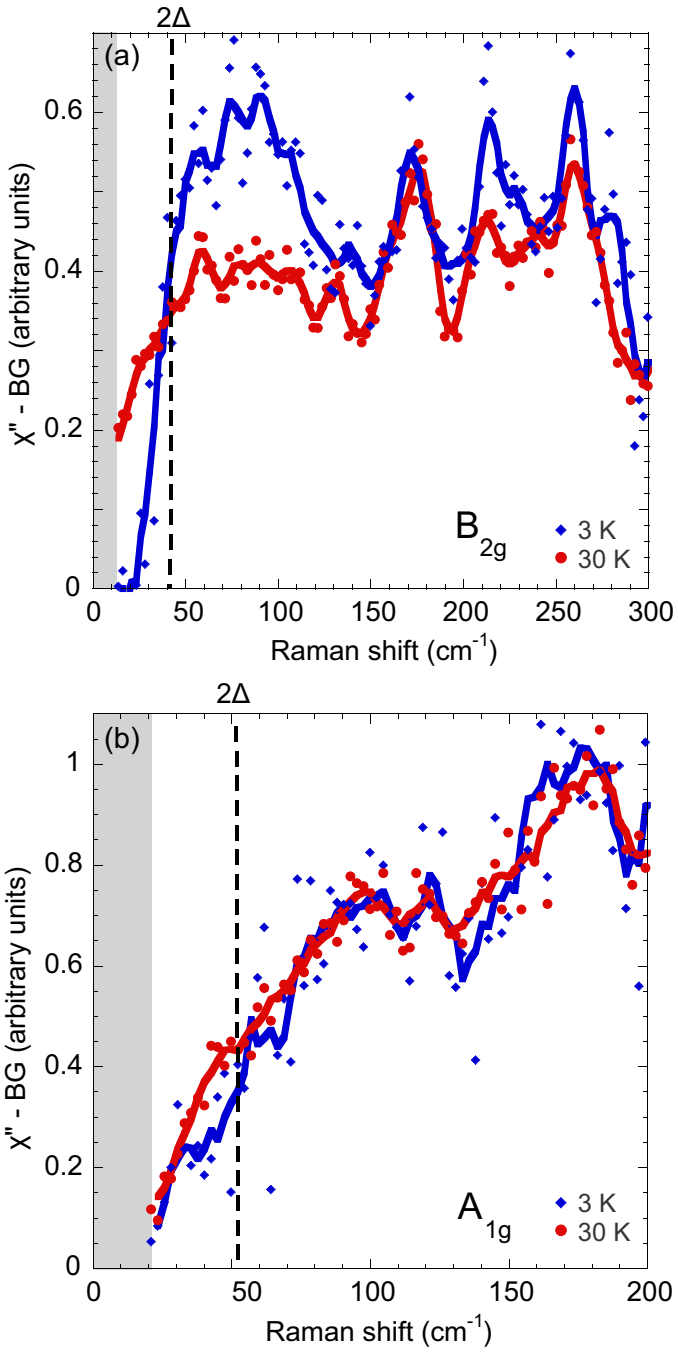

Figure 4.11: Electronic Raman response (background removed) of sample S3, obtained with 476 nm laser excitation in (a) B_{2g} and (b) A_{1g} channels. Blue (red) dots show superconducting (normal state) response averaged over four (two) experimental scans. Both thick lines represent 5-point smoothed data. Black dashed lines mark the energies corresponding to the superconducting gap observed, 2Δ. The gray area again indicates areas below the cutoff energy of the spectrometer.

features in the dI/dV curves at higher bias voltage that deviated from the BTK fit which they attributed to strong electron-boson coupling.

PCS measurements were also performed by Samuely *et al.* with sharpened Pt tips pressed into freshly cleaved optimally doped ($x = 0.14$) crystals. [42] BTK fits to the measured dI/dV curves showed only a single isotropic gap of magnitude Δ = 5-6 meV, suggesting that if multiple gaps were present they were close together in magnitude. Given the significant differences in gap structure observed through thermal conductivity across the $BaFe_{2-x}Co_xAs_2$ phase diagram, it is possible that the difference in these results may be due to different Co concentrations.

Terashima *et al.* examined the gap structure of $x = 0.15$ samples using ARPES and found strong evidence for two isotropic gaps. [51] Energy distribution curves showed two gaps with $\Delta_1 = 5 \pm 1$ meV on the electron pocket and $\Delta_2 = 7 \pm 1$ meV on the hole pocket. EDCs measured over a range of angles shows that both gaps are isotropic within error.

Muschler *et al.* performed Raman spectroscopy measurements on $BaFe_{2-x}Co_xAs_2$ samples with optimal doping ($x = 0.122$) and slight overdoping ($x = 0.17$). [53] Based on the strong low-temperature shift in the B_{2g} spectrum which varies as $\sqrt{\Omega}$ the authors propose an s-wave state with accidental nodes in the optimally doped sample. Slight overdoping resulted in a B_{2g} peak with greatly diminished amplitude suggesting that the gap is strongly effected by doping and disorder and potentially sample quality.

The most commonly agreed upon conclusion regarding the gap structure of $BaFe_{2-x}Co_xAs_2$ seems to be that there is an s-wave gap which is has no nodes at

optimal doping, but nodes appear at higher and lower Co concentrations. The nodes do not appear to be imposed by symmetry and are present away from the *ab*-plane. However, some results appear to contradict each other. For example, PCS studies have consistently supported an isotropic gap while Raman spectra at multiple dopings suggest the presence of nodes. Some have suggested reconstruction of the gap at the surface as a possible explanation for the difference, but this alone does not reconcile disagreements between thermal conductivity, PCS, and Raman spectroscopy, all of which are bulk probes. Another possible explanation is differences in crystal quality, and thus impurity scattering, as has been proposed by Muschler and others.

Compared to the Co-substituted system, our results on $BaFe_{1.9}Pt_{0.1}As_2$ offer a more comprehensive conclusion of an isotropic gap structure. All of the samples were made in the same batch and therefore are expected to have similar impurity concentrations and defect structures. Furthermore, our results all support the conclusion of at least one gap with a consistent magnitude of approximately 3 meV, and all experiments point to an isotropic *s*-wave gap symmetry.

Comparing the Co- and Pt-doping results, both optimally doped materials lack a residual thermal conductivity at zero field, indicating a fully-gapped superconducting order parameter. For the Co compound, a nonzero κ_0/T emerges at small magnetic fields, while for the Pt compound it remains zero at all fields observed. While the thermal conductivity of each material could only be observed up to a small fraction of H_{c2}, this may suggest subtle differences in gap morphology. BTK fits to PCS measurements on both yielded good fits to nodeless *s*-wave models. Results from our study with optimal Pt doping seem to compare more directly with those of overdoped

$BaFe_{2-x}Co_xAs_2$ rather than optimally doped. Both point to a two-gap structure with features present in the spectrum that do not perfectly match the BTK fit. This may indicate strong electron-boson coupling in both materials. ARPES measurements on optimally doped samples in both systems showed no variation in gap magnitude as a function of angle. [51] In the Co-doped compound, two gaps were consistently seen, while only one was observed in our study of $BaFe_{1.9}Pt_{0.1}As_2$. Finally, Raman spectra on both compounds feature low temperature enhancements in the A_{1g} and B_{2g} channels at positions which agreed with other reported values of gap size.

While we found no evidence of nodes for optimally doped $BaFe_{1.9}Pt_{0.1}As_2$, under- and overdoped compounds in the $BaFe_{2-x}Pt_xAs_2$ system have yet to be explored as far as gap structure is concerned. It has yet to be seen whether similar nodes would appear or if the Pt-substituted system would exhibit significant differences from the Co-substituted system. Future investigation of the entire $BaFe_{2-x}Pt_xAs_2$ phase diagram is certainly warranted.

Our results on $BaFe_{1.9}Pt_{0.1}As_2$ can also be used to draw interesting parallels with the multiband superconductor LiFeAs. Both compounds present no evidence of quasiparticle excitations in thermal conductivity measurements at low magnetic fields, and ARPES shows minimal gap anisotropy. Both also exhibit comparable small and large gap magnitudes as extracted from PCS measurements and ARPES measurements (in the case of LiFeAs), with $2\Delta/k_BT_c \simeq 2$ for the smaller gap in each system. The multi-gap nature of both materials would seem to be in disagreement with the thermal conductivity observations, but can be reconciled if one assumes the coherence length is similar between the two gaps. In our PCS observations of

$BaFe_{1.9}Pt_{0.1}As_2$, the large discontinuity between Z values for the two gaps is consistent with large differences between Fermi velocities, which means that v_F/Δ could be comparable for the two gaps as suggested for LiFeAs. [49]

4.5 Conclusions

In conclusion, I examined results from four measurement techniques that probed the superconducting gap in single-crystal samples of $BaFe_{1.9}Pt_{0.1}As_2$, finding reliable evidence for an isotropic one- or possibly two-gap s-wave model. Thermal conductivity measurements showed no sign of low energy quasiparticle excitations even at relatively high magnetic fields, with behavior comparable to other isotropic, single-gapped s-wave superconductors. While there was no indication of a reduced energy gap, the presence of a second gap cannot be completely excluded because of the small relative field range that was studied.

The conductivity spectra that I measured by point-contact Andreev reflection spectroscopy exhibit sharp enhancements and notable suppression of dI/dV at lower and higher bias, respectively, which suggests the presence of two gaps. Fitting to an isotropic two-gap Blonder-Tinkham-Klapwijk model results in gap size estimates of 2.5 meV and 7.0 meV, corresponding to features in the spectra that have been replicated in several crystals from the same batch.

Angle-resolved photoemission spectroscopy measurements show an isotropic gap on both electron and hole bands with a magnitude of approximately 3 meV. Finally, Raman spectroscopy revealed excitations in the superconducting state in both A_{1g}

and B_{2g} channels whose energy scales correspond with the 3 meV gap magnitude observed in other measurements.

Overall, I can conclude that the data on the optimally doped iron-based superconductor $BaFe_{1.9}Pt_{0.1}As_2$ support an isotropic, fully gapped superconducting order parameter with no nodes or deep minima, and possibly with band-dependent energy scales of order 3 meV and 7 meV. Combining results from different experimental probes allowed me to rule out several extrinsic parameters, allowing for better elucidation of the pairing mechanism of this iron-based superconductor.

Chapter 5: Point-Contact Spectroscopy in Half Heusler Compounds

5.1 Initial Characterization of Superconducting Materials

Single crystal samples of several half Heusler materials including YPtBi and LuPdBi have been synthesized using the Bi flux method described in Chapter 3. A detailed characterization of YPtBi was first described by Butch *et al.* (Ref. [81]) and revealed a lattice parameter of 6.6522(10) $\mathring{A}$ and the expected $F\bar{4}3m$ space group.

Figure 5.1 shows my measurement of resistivity as a function of temperature. Note that as YPtBi is cooled below 300 K, the resistivity first increases as expected for a band insulator. Below approximately 130 K however, $\rho(T)$ decreases before an abrupt zero resistance transition ending at $T_{c0} = 0.7$ K. This behavior is consistent with a semimetallic normal state. It should be noted that resistivity in this sample experiences a maximum at 133 K, while $\rho(1\text{ K})$ is nearly equal to $\rho(300\text{ K})$. This contrasts with the samples measured by Butch *et al.*, where resistivity leveled off below approximately 100 K rather than decreasing, and as a result $\rho(1\text{ K})$ was approximately twice $\rho(300\text{ K})$. The reason for this difference is not immediately clear, but it may be related to differences in crystal quality that affected the transition.

I also measured the low-temperature resistivity as a function of magnetic field, as shown in Fig. 5.2 for the same sample at 0.4 K. The observed R vs. H behavior

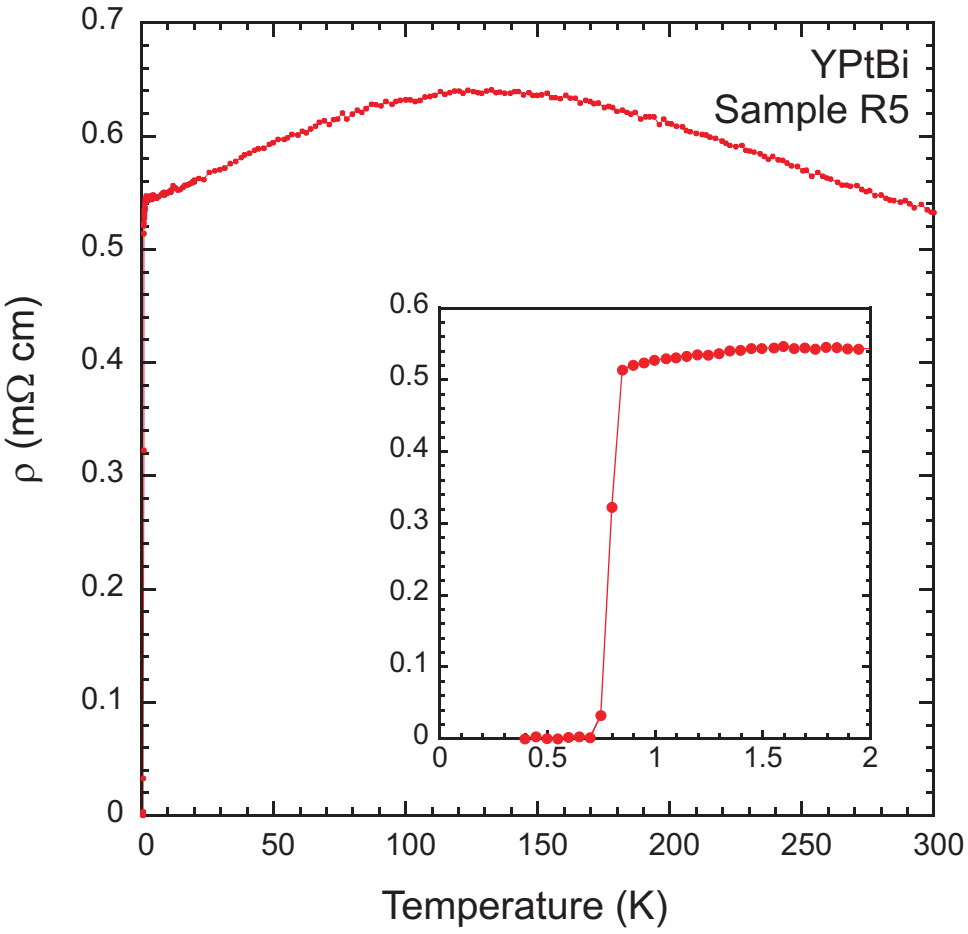

Figure 5.1: Resistivity vs. temperature between 0.4 K and 300 K showing semimetallic behavior. The inset shows a close-up of the data below 2 K and reveal $T_c \simeq 0.7$ K.

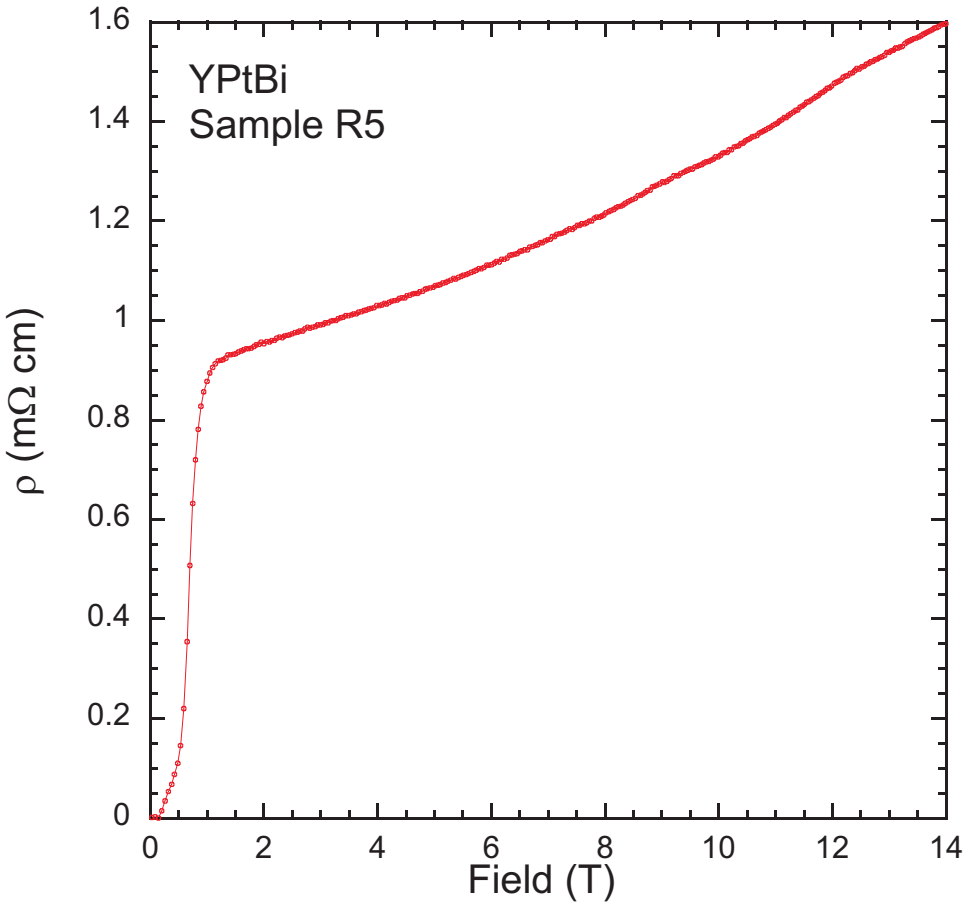

Figure 5.2: Resistivity ρ vs. magnetic field H in YPtBi at 0.4 K
Zero resistivity is only observed below 0.2 T, but based on the midpoint of the resistive transition, the true H_{c2} is closer to 1 T.

indicates a critical field of approximately $H_{c2} = 1$ T, although the resistivity continues to increase above the fairly broad transition.

5.2 Soft Point-Contact Measurements on YPtBi

5.2.1 Preparation of Junctions and the ^{3}He Probe

I measured point-contact spectra for these YPtBi samples using the soft point contact method with silver paste as the normal metal contact (see Chapter 3). Only

the soft point contact method was feasible because the samples had to low of a T_c to be accessible in our needle-anvil probe.

I prepared junctions by applying two "bottom" wires to the edges of a YPtBi sample that had sanded to reveal a large, flat face. I then coated the surface of the crystal with a clear epoxy, leaving a small contact area for the counter-electrode. This counter-electrode "tip" was applied by adhering a bent wire to the exposed area of the crystal with diluted silver paste. Fig. 5.3 shows a typical junction created in this fashion. In this case I left with three holes in the epoxy layer so that several junctions could be made from the same sample.

The four electrodes were attached to a measurement puck to prepare them for insertion into a PPMS using the specialized ^{3}He probe. Compared to the needle-anvil probe, this system offers a few advantages. In addition to a lower base temperature and faster cooling, it also allows for the application of magnetic fields of up to 14 T, which enables a wider range of data to be measured.

5.2.2 Measured dI/dV Curves

Samples were cooled to temperatures as low as 400 mK with the PPMS ^{3}He option. Conductivity spectra were measured by slowly sweeping the DC bias voltage V_{bias} while using a lock-in amplifier to apply a small AC current signal I and measure the response V. This process was repeated over a range of temperatures and applied magnetic fields up to and above T_c and H_{c2}, respectively.

$I - V$ curves were converted to dI/dV vs. V_{bias} and were divided by their high

Figure 5.3: YPtBi single crystal sample R5 used for soft point contact measurements as shown in Fig. 3.11. Gold wires on far left and right represent the V_- and I_- "bottom" electrodes. Clear epoxy has been painted over most of the surface except for three spots, each approximately 100 μm in diameter. The uppermostmost spot is covered with silver paste, as it was used in a previous measurement for which the tip wire has since been removed. The leftmost spot contains an intact junction with a thinner gold wire used as the V_+ and I_+ "top" electrodes. The rightmost spot shows the still-exposed crystal surface through the slightly opaque epoxy.

bias values in order to normalize them. Fig. 5.4 shows dI/dV data taken in zero applied field over a range of temperatures, while Fig. 5.5 shows data over a range of applied magnetic fields at a constant temperature of 0.4 K. For all samples I observed a relatively flat background conductance on the order of 0.1-1 Ω in the normal state.

The sample denoted as R5 used for point-contact measurements in Figs. 5.4 and 5.5 is the same that was used for the R vs. T and R vs. H measurements in Figs. 5.1 and 5.2, but not during the same measurement run. After the resistivity measurements I removed the sample from the cryostat, cleaned it in acetone to remove the silver paste from the resistivity contacts, and prepared the soft point contact junction as described previously. Although these data sets were not taken *in situ*, the sample was exposed to air for a short period of time (less than an hour) and showed no obvious signs of oxidation.

5.2.3 Comparison to Previous Studies

The most obvious feature of the dI/dV spectra shown in Figs. 5.4 and 5.5 is the strong enhancement in conductivity at zero bias. This zero bias conductance peak (ZBCP) is characteristic of point-contact spectra in the Andreev reflection regime. The ZBCP diminishes in height and disappears above both T_c and H_{c2}, which is a strong indication that this feature represents a superconducting effect rather than some type of anomalous scattering. A less obvious aspect of the data is that dI/dV increases monotonically up to $V_{bias} = 0$. Typically for soft point-contact spectra one observes a "split peak" morphology, which is characterized by a small dip in the

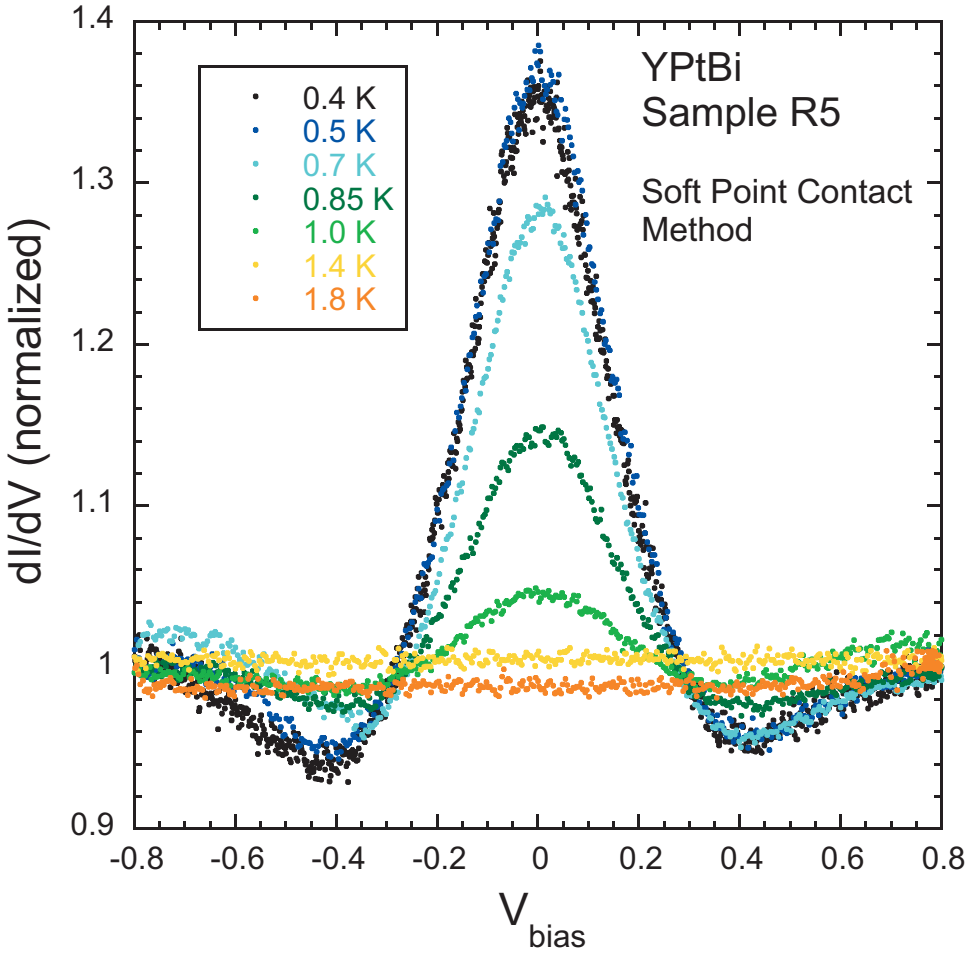

Figure 5.4: Normalized dI/dV vs. V_{bias} for sample R5 for selected temperatures. An enhancement of roughly 40% is observed at zero bias compared to the high bias dI/dV value. The peak is not split, as would be expected for a conventional superconductor. This peak persisted above 1.0 K, which is unusual considering the resistive transition temperature of $T_c = 0.7$ K.

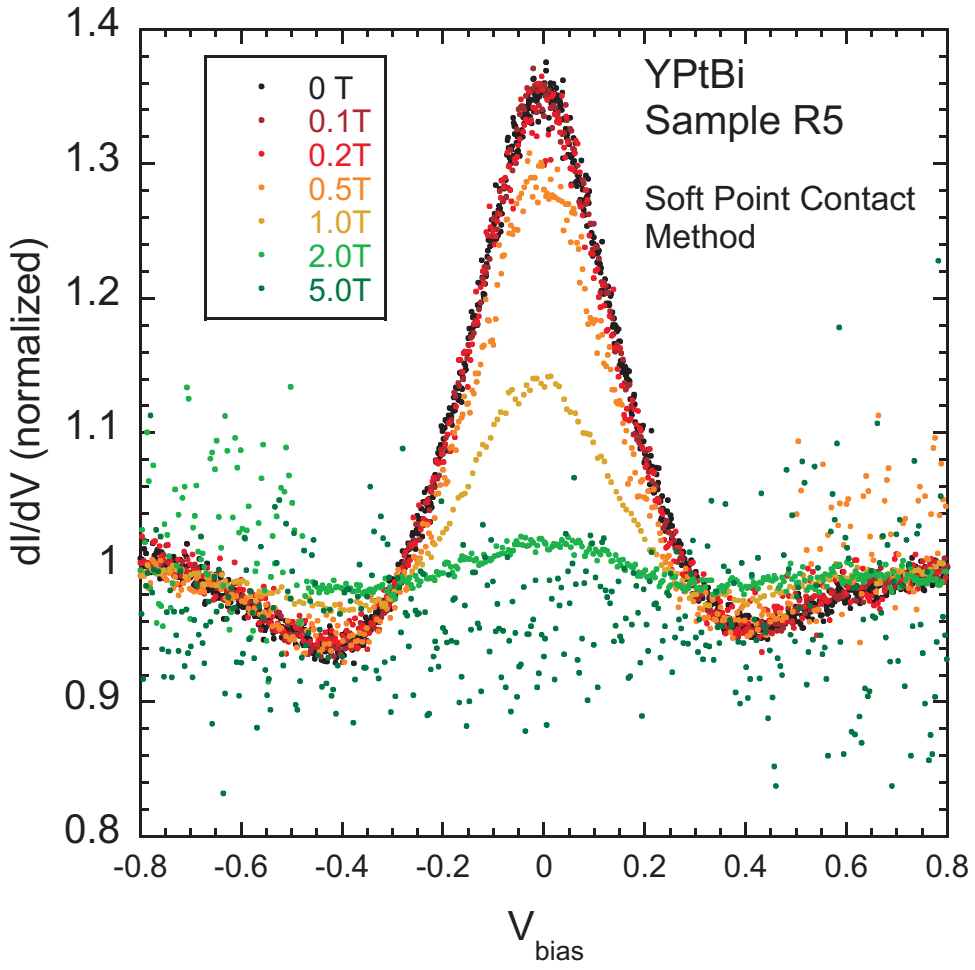

Figure 5.5: Normalized dI/dV vs. V_{bias} for selected applied magnetic fields measured at a temperature of 0.4 K. The zero bias peak decreases in magnitude before disappearing at roughly 2 T. This is also unexpected, as the upper critical field appears to be closer to 1 T as shown in Fig. 5.2. The considerable amount of noise in the 5.0 T spectrum and part of the 2.0 T spectrum is likely due to deterioration of the junction due to repeated application of current. This change in the junction occurred during the 2.0 T sweep and persisted during the 5.0 T sweep (which were performed in that sequential order at the end of the measurement). Despite the noise, those sections of the dI/dV spectrum still look as expected on average, with no strong changes in the average conductance for both $V_{bias} < -\Delta$ at 2.0 T and the entire 5.0 T sweep, for which $H > H_{c2}$.

dI/dV peak at zero bias. This dip is usually small, both in terms of the relative decrease in conductivity and the range of bias voltages over which it is measured, but it has been consistently observed for soft point contact measurements for a variety of samples close to T = 0 [41]. While the single peak structure is predicted by the BTK theory for Z = 0 case of complete Andreev reflection, [40] this is generally not observed in soft point contact measurements. In the case of YPtBi, this lack of a split in the ZBCP is a possible indication of unconventional superconductivity, as I discuss below.

In addition to the shape of the curves, other aspects of the data are unusual compared to what is expected for conventional superconductivity. First, the zero bias enhancement shown in Figs. 5.4 and 5.5 persists at values of temperature and magnetic field that are above the values of T_c and H_{c2} that were determined from the resistivity measurements in Figs. 5.1 and 5.2. The reason for the persistence of these gap features is unknown, but it may be suggestive of unconventional superconductivity. Second, the size of these gap features is also quite large compared to the expected weak-coupling BCS value of $\Delta_{BCS} = 1.76 k_B T_c = 0.1$ meV for a T_c of 0.7 K. In fact, based on the peak width the gap size appears to be at least twice the BCS value. This large deviation from weak-coupling provides some evidence against a conventional weak-coupling s-wave model.

It is interesting to compare these point-contact spectroscopy results, with those on the triplet p-wave SC Sr_2RuO_4 (see Chapter 2). Laube *et al.* measured soft point contact spectra on Sr_2RuO_4 and observed conductance curves with two distinct morphologies [90]. dV/dI resistance curves are compared with our YPtBi data at

0.4 K and 0 T in Fig. 5.6.

In the case of Sr_2RuO_4, some SPC junctions yielded a typical split-peak shape (which manifests as a split well for dV/dI data). However, other junctions showed an unsplit zero bias conductivity enhancement, similar to what I observed. This behavior in Sr_2RuO_4 was coupled with enhancements in dV/dI at higher bias that very closely mirror the higher bias dips in my conductivity data so that the shape of the dV/dI curves is quite similar between the two materials.

Laube *et al.* concluded that the presence of two types of zero bias features was consistent with a p-wave superconducting state and triplet pairing. Fits to the measured data showed that the dI/dV curves with a zero bias "double-minimum" are consistent with a high transparency barrier between a normal metal and a triplet superconductor, while the curves with the single-minimum zero bias dip corresponded to a low transparency condition. It is possible that our results are also in the low transparency limit for a normal metal-triplet superconductor junction. Of course, it is also possible that some other effect is producing the single minimum, but the positive comparison to Sr_2RuO_4 is encouraging.

5.2.4 Multiple Samples and >100% Zero Bias Enhancement

I repeated conductance measurements on different YPtBi samples in order to verify that the zero bias feature was repeatable and not an anomaly. Figure 5.7 shows dI/dV curves for three samples, including the one from Figs. 5.4 and 5.5, at 0.4 K in zero magnetic field. The zero bias unsplit peak is a consistent feature, but the height

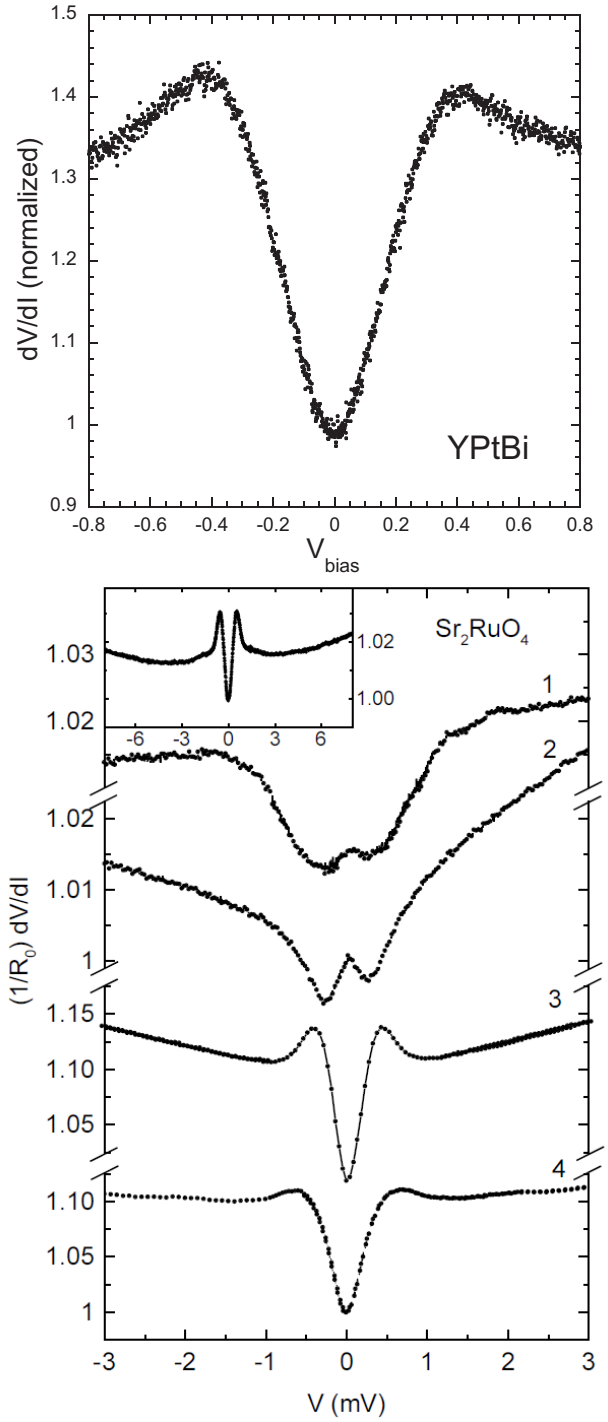

Figure 5.6: Comparison between dV/dI curves for YPtBi (top) and Sr_2RuO_4 (bottom). YPtBi data is the inverse of the 0.4 K, 0 T curve from Figs. 5.4 and 5.5. Sr_2RuO_4 data is from Ref. [90]. Laube *et al.* observed two different forms of dV/dI spectra using the same soft point contact technique on p-wave Sr_2RuO_4. Curves 3 and 4 strongly resemble our YPtBi data, with a smooth zero bias suppression of dV/dI and small enhancements at higher bias.

of the ZBCP is not constant. Indeed, for one sample the zero bias conductance was over twice the high bias value. I note that Sasaki *et al.* [92] have claimed a zero bias enhancement of over 100% is evidence of topological superconductivity in $Sn_{1-x}In_xTe$. Because I did not consistently observe this high level of enhancement, I do not claim that this material is topological or even that this large zero bias enhancement is repeatable. It is also notable that the energy scale of these gap features is fairly consistent, if one considers the higher bias "dip" observed for two of the three samples. This consistency between samples with a variety of junction resistances (with a range of 0.3 Ω – 8 Ω at high bias) supports the assumption that the ZBCP represents the SC gap.

5.3 Attempts at LuPdBi Tunnel Junctions

In order to confirm the unconventional nature of the superconducting gap in the half-Heuslers I attempted to artificially alter the impedance of the junctions to force them into the tunneling regime. Recent work on Fe nanowires suggests that a zero bias enhancement in an STM tunneling spectrum can be due to Majorana fermions [124]. Furthermore, measuring dI/dV curves over a range of junction resistances and Z values should strengthen the argument that the previously observed zero bias peaks represent a true superconducting gap.

The work described in this section was performed at the University of Illinois at Urbana-Champaign in conjunction with the group of Prof. Laura Greene. Dr. Greene's group, especially Dr. Wan Kyu Park, provided me with experimental assis-

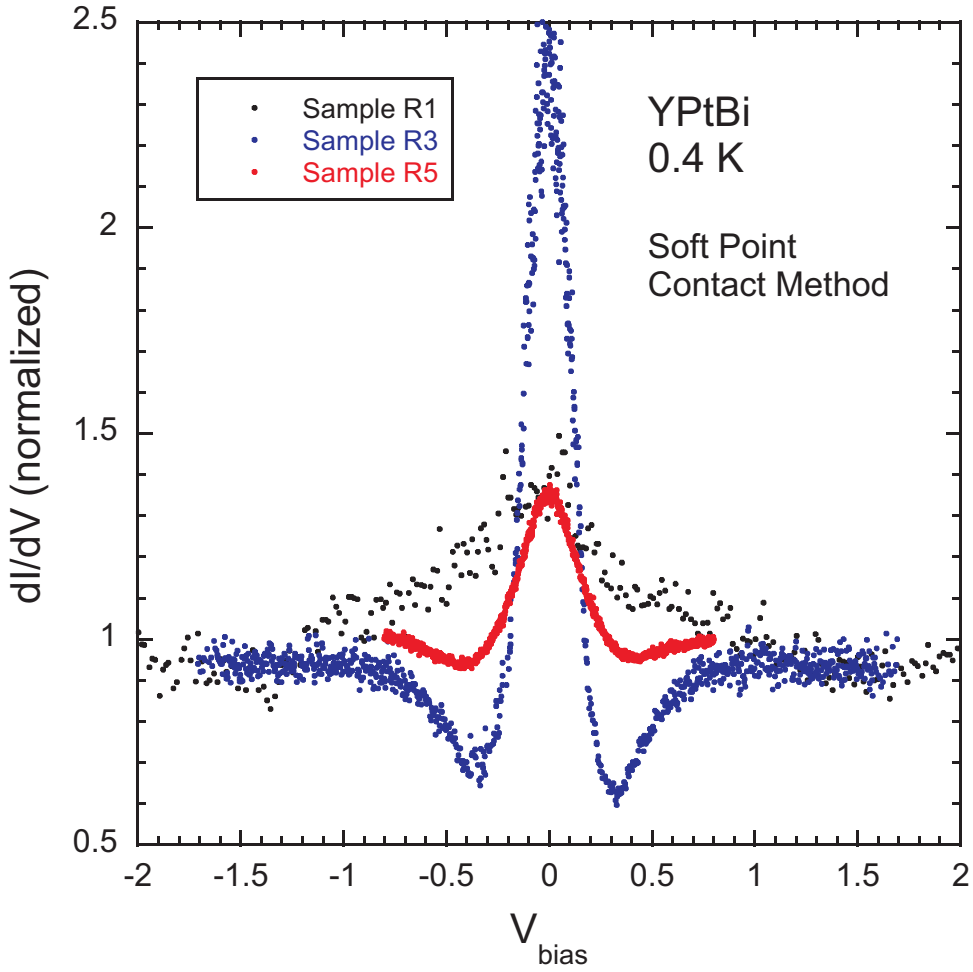

Figure 5.7: dI/dV vs. V_{bias} at $T = 0.4$ K and $H = 0$ T for YPtBi samples R1, R3, and R5. The shape of the curves and height of the zero bias enhancement changes significantly between samples, but the consistent width of the overall curves possibly suggests the same energy scale for the gap features. Although sample R1 has a much broader peak, it lacks the higher bias dips in dI/dV present in the other two samples.

tance. Dr. Park taught me this method of sample preparation and how to do the SiO_2 sputtering and Ag evaporation steps described below.

5.3.1 Preparation of Junctions

To artificially increase the junction resistance, a thin film layer of Al_2O_3 was deposited onto the surface of LuPdBi crystals. Although my previous measurements focused on YPtBi, I chose LuPdBi in this case because larger crystals were available and these were better suited for the tunnel junction preparation process. LuPdBi is also predicted to be a topologically non-trivial material according to DFT. Furthermore, with a T_c of 1.7 K, a cryostat with a base temperature of 0.4 K would be capable of reaching well below T_c so that temperature-dependent trends would be more apparent.

Prior to thin film deposition, I polished the samples to create as smooth a surface as possible; if the insulating SiO_2 layer is deposited on a rough surface, it may result in cracks or other defects and compromise the oxide layer′s insulating benefits. Samples were embedded in Stycast 1266 two-part epoxy in order to hold them flat for polishing and make the millimeter-scale crystals easier to manipulate. They were then polished with increasingly fine lapping films containing either Al_2O_3 or diamond particles to achieve smoothness on the scale of less than 1 μm. In between polishing steps, samples were inspected using a differential interference contrast (DIC) microscope to assess the state of the surface and make sure that any scratches had been removed.

Once the surface was sufficiently smooth, I masked each sample with thin strips of aluminum foil so that the edges of the crystal would remain exposed. This was necessary so that the bottom wires could be applied directly to the LuPdBi sample after film deposition. Samples were then loaded into a sputtering chamber and a 70 $\mathring{A}$ Si film was deposited onto the surface. The Si film was then oxidized, either by exposing the sample to O plasma, or simply by filling the chamber with O_2 gas and heating the sample. For some samples, an additional step was taken of masking the sample again and depositing strips of Ag to serve as the top wires in the junction. Figure 5.8 illustrates the general appearance of the sample at different points in the deposition process.

5.3.2 Behavior of dI/dV with Increasing Temperature and Field

Samples were then mounted on measurements pucks and cooled in a PPMS Dynacool cryostat using the external ^{3}He probe. I obtanined conductivity vs. bias voltage data for a for several samples over a range of temperatures and applied magnetic fields.

Figure 5.9 presents my conductivity data for one LuPdBi sample over a range of temperatures. The top figure shows the zero bias conductance as the sample was cooled from 300 K to 0.4 K. As expected, the conductivity changes abruptly at T_c = 1.7 K. This change was an increase in dI/dV suggesting that the junction is in the Andreev reflection regime. This is confirmed by the dI/dV vs. V_{bias} curves in the bottom figure, in which a zero bias enhancement is observed consistently up to T_c.

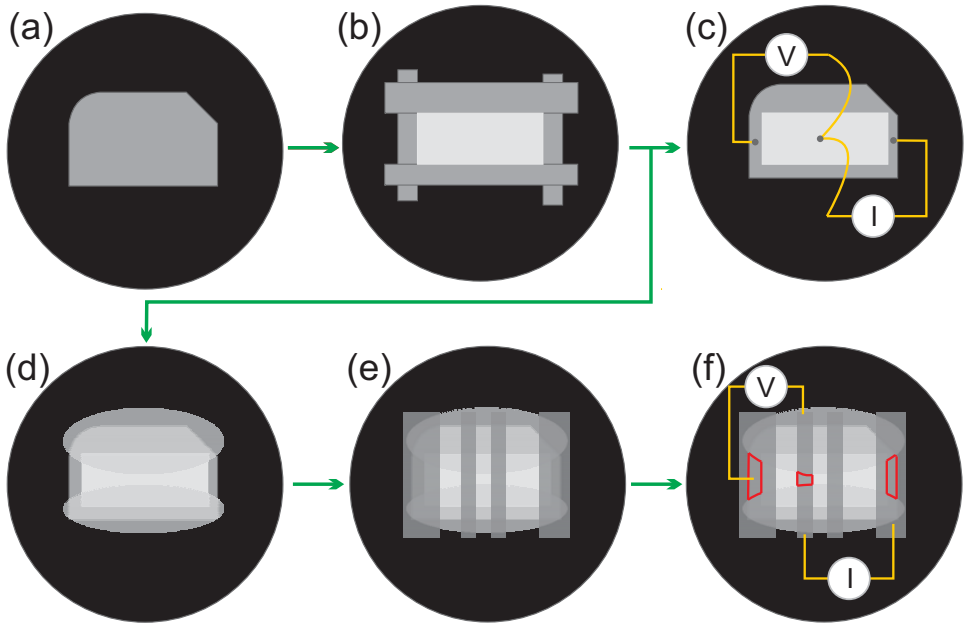

Figure 5.8: Schematic of steps in the process of fabricating LuPdBi tunnel junctions. (a) Sample (gray) is embedded in a disk of Stycast 1266 two-part epoxy (black) and polished to achieve as flat a surface as possible. (b) The sample is masked by covering the edges with strips of Al foil and a 70 $\mathring{A}$ film of Si is sputtered on the surface and oxidized. When the mask is removed the center of the crystal is covered with SiO_2 while the edges are less oxidized. (c) For a quicker measurement, gold wires are simply attached to the sample with silver paint for a soft point contact measurement. (d) Alternatively, the sample is prepared for an additional deposition of Ag strips to create a more stable electrical contact. To make sure the junction is as small as possible, most of the sample is covered with transparent, electrically insulating Duco cement. (e) Next, the sample is masked with Al strips once again and coated with a layer of Ag using an evaporator. (f) Gold wires are applied to the deposited Ag strips to complete the junction. Areas highlighted in red represent the points of contact with the crystal. The two bottom wires connect directly to the crystal through the silver contacts. The junction itself is made at the small section of the middle silver strips in between the spots of Duco cement. With proper masking before Ag deposition and careful application of cement, this junction can be quite small (on the order of 0.1×0.1 mm^2).

A few conclusions can be drawn from my data. First, it is quite apparent that the device was not a tunnel junction. In fact, these dI/dV curves look quite similar to those of YPtBi discussed previously. Each higher temperature dI/dV spectrum has the same single-peak structure, and a slight decrease in conductivity at higher bias, though this dip is not as pronounced as the ones I observed for YPtBi. This suggests possible similarities between YPtBi and LuPdBi and possibly that LuPdBi is a topological superconductor. Another point worth noting is that the dI/dV vs. T plot is roughly linear close to T_c. This is somewhat unexpected as the zero bias conductance should behave like an order parameter in increasing temperature, however the significance of this behavior is unclear.

Similar measurements were performed with applied magnetic fields up to 3 T with the results shown in Fig. 5.10. The upper figure shows that the dI/dV enhancement disappears above $H_{c2} = 2$ T, but with a similarly unusual linear morphology that does not resemble the expected behavior for an order parameter. The enhancement in dI/dV vs. bias voltage, in the lower figure, decreases up to H_{c2} as expected, though the high-field background conductance is not quite as flat as its high-temperature counterpart. These results confirm that the zero bias enhancement represents a true superconducting gap, although the persistence of a zero bias peak height that decreases linearly as the superconducting state is suppressed remains puzzling.

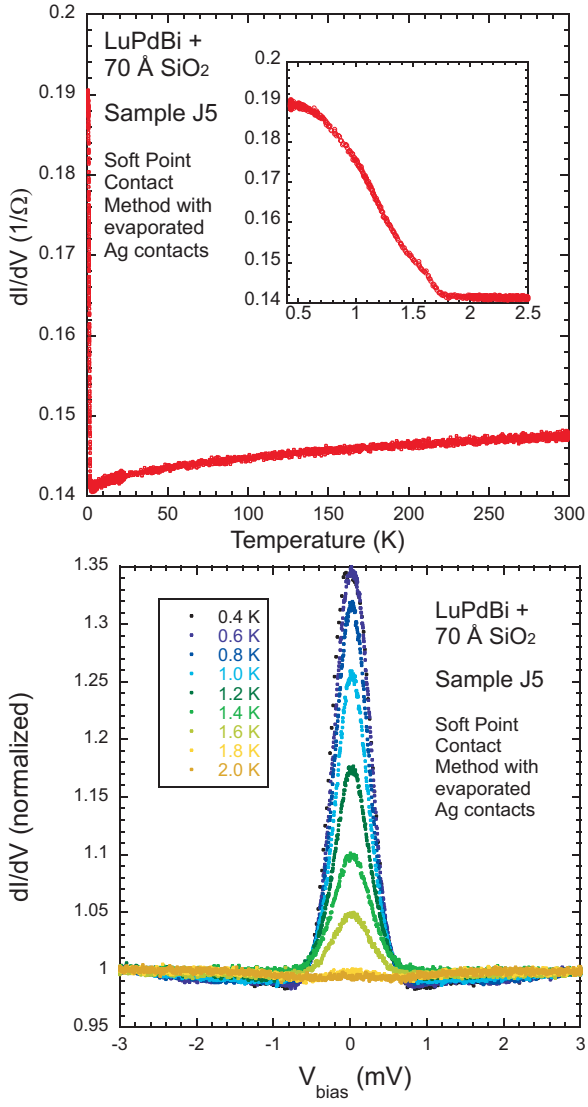

Figure 5.9: Conductivity vs. temperature of a LuPdBi point contact junction. The top figure shows that conductivity is roughly constant down to $T_c = 1.7$ K, at which point it increases abruptly. The inset shows a detailed view of the data below 2.5 K. The bottom plot shows a series of dI/dV vs. V_{bias} curves up to and above T_c. This junction is in the Andreev limit rather than tunneling, and exhibits a strong single-peaked enhancement in dI/dV as well as very small dips at higher bias (not visible at this scale).

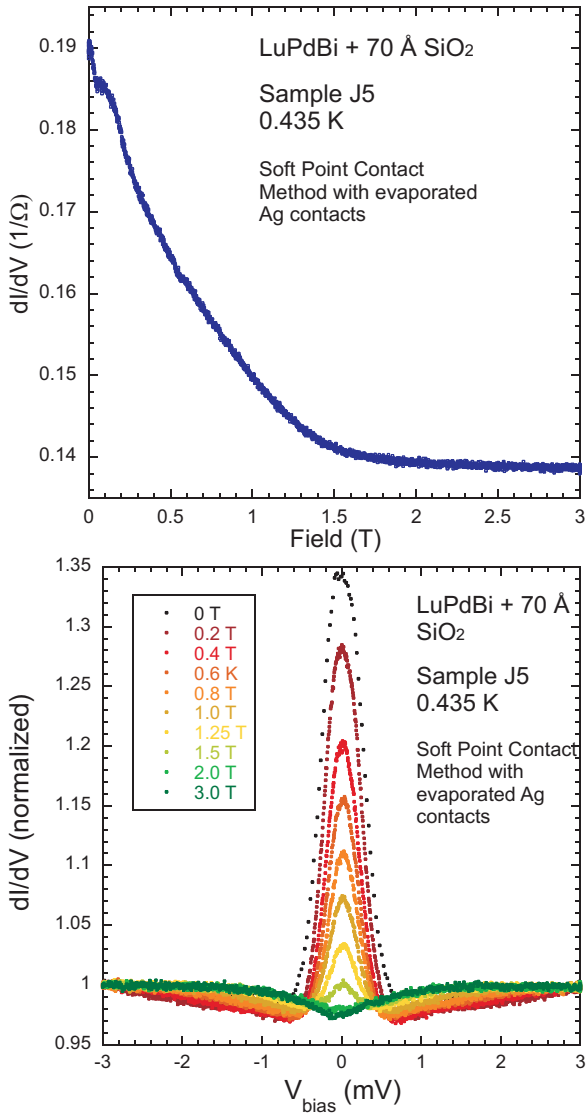

Figure 5.10: Zero bias dI/dV of LuPdBi as a function of magnetic field (above) and dI/dV vs. V_{bias} for a range of applied field values (below). Conductivity decreases and levels off above $H_{c2} = 2$ T, but the roughly linear decrease is unexpected. The zero bias enhancement retains the single-peak shape up to H_c2. Note that these measurements were obtained at at $T = 0.4$ K.

5.3.3 Discussion

My efforts to create well-defined point contact tunnel junctions with LuPdBi ultimately led to mixed results. On the positive side, the process of polishing and oxide deposition were successful in producing junction with somewhat higher resistance. Junctions made without an SiO_2 layer typically had resistances on the order of 0.1 Ω. The addition of the oxide layer increased the resistance by two orders of magnitude - for example, the junction used in the measurements from Figs. 5.9 and 5.10 had a resistance of about 7 Ω.

My results also compare favorably to earlier measurements taken at the University of Maryland. For example, Fig. 5.11 shows the low temperature normalized dI/dV spectrum from Figs. 5.9 and 5.10 compared to similar spectra measured on LuPdBi samples that were not polished and did not have sputtered SiO_2. Both the junction measured at UIUC (J5, in red) and the junctions measured at UMD (R9 and R13, in blue) have similar unsplit peak structures (although the R9 data is too noisy to claim that definitively). Furthermore, the size of the gaps seems to be similar between the three junctions. Although it is not as evident from Fig. 5.11, the dI/dV curve for sample J5 does have a slight dip and a minimum around 0.7 mV, which is clearer in Figs. 5.9 and 5.10. This demonstrates that similar results can be obtained for junctions with a wider range of resistances.

Despite being unable to produce LuPdBi junctions in the tunneling regime, my junctions still yielded some interesting results. The presence of a consistent unsplit zero bias peak in the dI/dV vs. V_{bias} curves is similar to behavior seen in YPtBi,

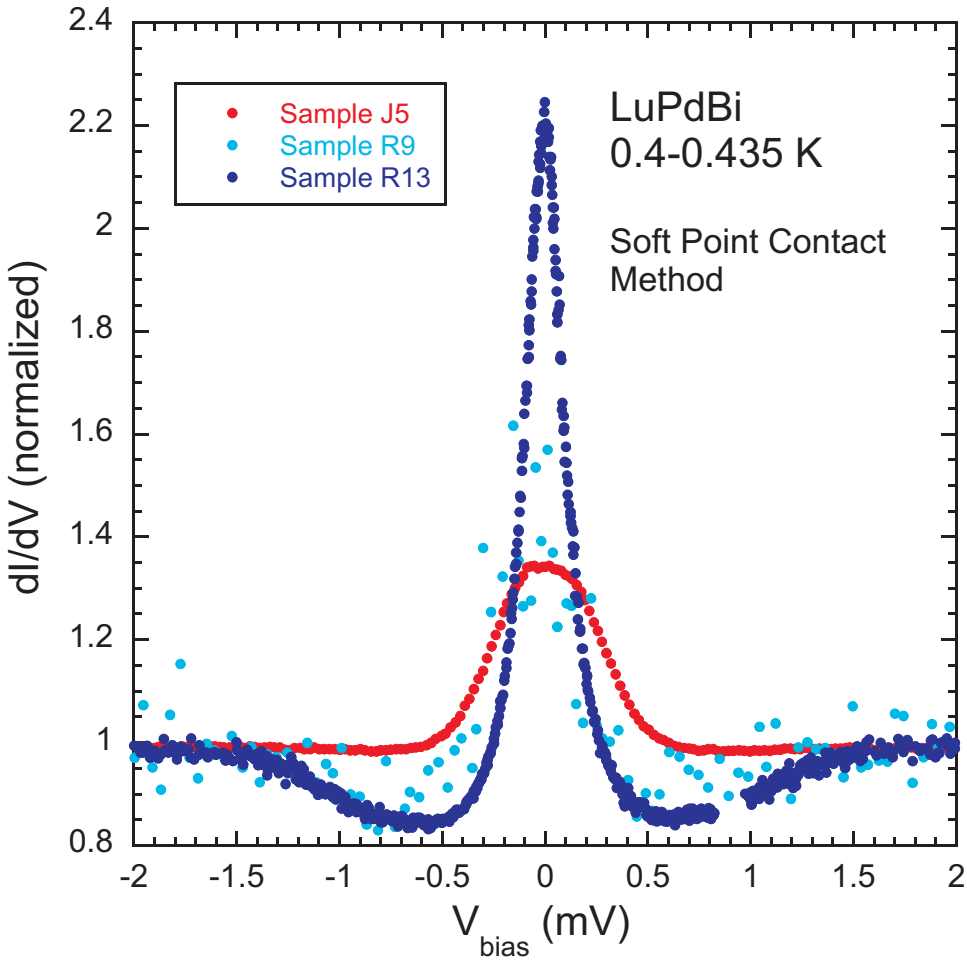

Figure 5.11: Low temperature, zero magnetic field dI/dV spectra for three LuPdBi soft point contact junctions. Sample J5 (red) was polished and sputtered with SiO_2 and was prepared at UIUC. Samples R9 and R13 (blue) did not undergo this polishing and deposition process and were prepared at UMD. The high-bias junction resistances of these samples were 7 Ω, 1.8 Ω, and 1.6 Ω for J5, R9, and R13, respectively.

suggesting LuPdBi might possibly be a topological superconductor. I also note that I did make junctions with even higher junction resistances, one as high as $R_J = 1$ kΩ. Unfortunately, these high resistance junctions resulted in dI/dV data that was extremely noisy to the extent that no discernible features could be extracted. This is still a promising development, as it shows that point contact tunnel junctions with these materials may not be too far off.

5.4 Conclusions

In conclusion, I have performed soft point-contact spectroscopy measurements on the half-Heusler superconductors YPtBi and LuPdBi and observed a consistent single-peak enhancement in dI/dV at zero bias. This result suggests unconventional superconductivity as expected for a noncentrosymmetric and possibly topological superconductor. The unsplit zero bias peak combined with high-bias dips was consistent with theoretical predictions for a superconductor with a triplet pairing state. This behavior was also consistent with previous experimental work on the unconventional triplet p-wave material Sr_2RuO_4. Future work would be needed to verify the possibility of triplet pairing and to positively identify a p-wave or mixed parity order parameter

Chapter 6: Conclusions

In conclusion, I have used point-contact spectroscopy for measurement of the electronic structure of superconductors. My work, in collaboration with other researchers, has expanded knowledge of a variety of unconventional superconductors. My work has yielded positive results, opened more questions about these materials, and suggests many possible future experiments.

I used the needle-anvil point contact method to measure AC conductivity vs. DC bias voltage in the iron pnictide superconductor $BaFe_{1.9}Pt_{0.1}As_2$. dI/dV curves were obtained for several single crystal samples down to 4 K using a probe with an adjustable mechanical stage that was used to create junctions between sharpened Pb or Au tips and the *ab*-plane of the samples. After background subtraction and normalization, the dI/dV data showed a sharp peak at zero bias and sharp decreases in conductivity at higher bias voltages. I fit my results to a two-gap isotropic *s*-wave model using the Blonder- Tinkham-Klapwijk theory and found reasonable agreement.

Analysis of these fit parameters revealed a high-transparency gap of magnitude 3 meV and a 7 meV gap that was closer to the tunneling limit with a high degree of inelastic scattering. This apparent discrepancy in transparency was possibly due to the high scattering rate in the 122 iron pnictides and/or an impedance mismatch

between the normal metal tip and superconductor. My measurements on multiple samples confirmed the consistent presence of two gap-like features at roughly 3 and 7 meV.

I also discussed three other experimental techniques that were applied to crystals from the same growth batch to check the interpretation of my point-contact spectroscopy results. Thermal conductivity revealed no quasiparticle excitations at low temperature, consistent with a nodeless gap structure. Angle-resolved photoemission spectroscopy and Raman spectroscopy confirmed the presence of the smaller 3 meV gap but did not show convincing evidence for the larger 7 meV gap. The ARPES result also showed no evidence for nodes or deep minima in the order parameter.

Overall, this represents consistent evidence of an isotropic 3 meV gap in $BaFe_{1.9}Pt_{0.1}As_2$. This stands in contrast to much other work on similar materials, in which different groups reached different conclusions on gap size and symmetry for seemingly identical materials. The success of our approach, which used crystals from the same growth batch, highlights the importance of crystal quality in studies of superconducting gap structure. Differences in impurity content and/or defect structures seem to be the most likely cause of these inconsistencies.

Finally, I applied the soft point contact technique to single crystal samples of the noncentrosymmetric half-Heusler superconductor YPtBi. Samples were sanded down to reveal flat faces for the application of electrical contacts. I attached gold wire electrodes with conductive silver paste, and used electrically insulating epoxy to reduce contact between the paste and crystal surface and ensure a small contact area for the junction. I measured conductivity vs. bias voltage in a ^{3}He probe capable of

reaching temperatures below 400 mK with applied magnetic fields up to 14 T.

dI/dV measurements on YPtBi samples revealed a consistent peak at zero bias and shallow dips at higher bias. A single peak is inconsistent with the results predicted for soft point contact measurements of an s-wave material, in which case a double-maximum "split peak" structure is typically observed. Conductivity curves measured at higher temperatures and magnetic fields confirmed that the observed peak is from the superconducting state rather than a temperature effect or from anomalous scattering. Repeating the measurement on other samples confirmed the consistency of this single peak structure. Comparison to previous work showed the dI/dV curves resemble those measured for the triplet-pairing p-wave superconductor Sr_2RuO_4 as well as theoretical predictions for a generic noncentrosymmetric superconductor. This suggests that YPtBi may be a triplet p-wave superconductor, or at least has a mixed-parity pairing state with a p-wave component.

My work suggests some possible directions for future studies. I found that a range of experiments performed on iron-based superconductors from the same batch of crystals can yield highly consistent results. Similar studies on different pnictide materials would be interesting. This could help shed light on compounds that have been previously studied but found to give contradictory results, such as $BaFe_{2-x}Co_xAs_2$. It could also be useful for investigating new superconductors or materials for which the gap symmetry has not been decisively settled, such as $Ba_{1-x}K_xFe_2As_2$ compounds on the K-rich end of the phase diagram.

In the realm of topological superconductors, point-contact spectroscopy could be useful for investigating the electronic structure. All of the superconducting half-

Heuslers share the same noncentrosymmetric crystal lattice, but it has yet to be shown whether they also share the p-wave characteristics predicted for chiral materials. Further complicating matters are theoretical models indicating that some half-Heuslers should be topologically trivial while others should exhibit band inversion. The fact that both sides of the topological/non-topological divide feature known superconductors suggests the possibility of using point-contact spectroscopy to separate superconductors with different topologies. Finally, several of the half-Heuslers contain highly magnetic rare earth elements and as a consequence exhibit magnetically ordered states at low temperature. Here, PCS and other spectroscopic techniques could be used to detect changes in gap structure above and below the magnetic transition temperatures to determine what effect, if any, these magnetic interactions have on the topological superconducting state.

Bibliography

[1] A. Cho, "Superconductivity's Smorgasbord of Insights: A Moveable Feast," *Science*, vol. 332, p. 190-192, 2011.

[2] L. N. Cooper, "Bound Electron Pairs in a Degenerate Fermi Gas," *Physical Review*, vol. 104, p. 1189-1190, 1956.

[3] J. Bardeen, L. N. Cooper, and J. R. Schrieffer, "Microscopic Theory of Superconductivity," *Physical Review*, vol. 106, p. 162-164, 1957.

[4] J. Bardeen, L. N. Cooper, and J. R. Schrieffer, "Theory of Superconductivity," *Physical Review*, vol. 108, p. 1175-1204, 1957.

[5] M. Tinkham, *Introduction to Superconductivity*. Dover Publications, 1996.

[6] J. G. Bednorz and K. A. Müller, "Possible High T_c Superconductivity in the Ba-La-Cu-O System," *Zeitschrift für Physik B*, vol. 64, p. 189-193, 1986.

[7] C. W. Chu, L. Gao, F. Chen, Z. J. Huang, R. L. Meng, and Y. Y. Xue, "Superconductivity above 150 K in $HgBa_2Ca_2Cu_3O_{8+\delta}$ at high pressures," *Nature*, vol. 365, p. 323-325, 1993.

[8] L. Gao, Y. Y. Xue, F. Chen, Q. Xiong, R. L. Meng, D. Ramirez, C. W. Chu, J. H. Eggert, and H. K. Mao, "Superconductivity up to 164 K in $HgBa_2Ca_{m-1}Cu_mO_{2m+2+\delta}$ (m=1, 2, and 3) under quasihydrostatic pressures," *Physical Review B*, vol. 50, p. 4260, 1994.

[9] Y. Kamihara, T. Watanabe, M. Hirano, and H. Hosono, "Iron-Based Layered Superconductor $La[O_{1-x}F_x]FeAs$ (x = 0.05-0.12) with T_c = 26 K," *Journal of the American Chemical Society*, vol. 130, p. 3296-3297, 2008.

[10] M. Norman, "The challenge of unconventional superconductivity," *Science*, vol. 332, p. 196-200, 2011.

[11] J. Paglione and R. L. Greene, "High-temperature superconductivity in iron-based materials," *Nature Physics*, vol. 6, p. 645, 2010.

[12] I. I. Mazin, "Superconductivity gets an iron boost," *Nature*, vol. 464, p. 183-186, 2010.

[13] K. Ishida, Y. Nakaii, and H. Hosono, "To What Extent Iron-Pnictide New Superconductors Have Been Clarified: A Progress Report," *Journal of the Physical Society of Japan*, vol. 78, p. 062001, 2009.

[14] S. R. Saha, T. Drye, K. Kirshenbaum, N. P. Butch, P. Y. Zavalij, and J. Paglione, "Uniform chemical pressure effect in solid solutions $Ba_{1-x}Sr_xFe_2As_2$ and $Sr_{1-x}Ca_xFe_2As_2$," *Journal of the Physics of Condensed Matter*, vol. 22, p. 072204, 2010.

[15] K. Kirshenbaum, S. R. Saha, T. Drye, and J. Paglione, "Superconductivity and magnetism in platinum-substituted $SrFe_2As_2$ single crystals," *Physical Review B*, vol. 82, p. 144518, 2010.

[16] S. R. Saha, N. P. Butch, K. Kirshenbaum, and J. Paglione, "Evolution of bulk superconductivity in $SrFe_2As_2$ with Ni substitution," *Physical Review B*, vol. 79, p. 224519, 2009.

[17] S. R. Saha, N. P. Butch, T. Drye, J. Magill, S. Ziemak, K. Kirshenbaum, P. Y. Zavalij, J. W. Lynn, and J. Paglione, "Structural collapse and superconductivity in rare earth-doped $CaFe_2As_2$," *Physical Review B*, vol. 85, p. 024525, 2012.

[18] B. D. Cullity and S. R. Stock, *Elements of X-Ray Diffraction*, Prentice-Hall Inc., 2001.

[19] X. Zhu, F. Han, G. Mu, J. Tang, J. Ju, K. Tanigaki, and H.-H. Wen, "Superconductivity induced by doping platinum in $BaFe_2As_2$," *Physical Review B*, vol. 81, p. 104525, 2010.

[20] M. Rotter, M. Pangerl, M. Tegel, and D. Johrendt, "Superconductivity and Crystal Structures of $(Ba_{1-x}K_x)Fe_2As_2$ (x=0-1)," *Angewandte Chemie International Edition*, vol. 47, p. 7949-7952, 2008.

[21] X. Zhu, F. Han, G. Mu, P. Cheng, J. Tang, J. Ju, K. Tanigaki, and H.-H. Wen, "Superconductivity induced by doping platinum in $BaFe_2As_2$," *Physical Review B*, vol. 81, p. 104525, 2010.

[22] S. Jiang, H. Xing, G. Xuan, C. Wang, Z. Ren, C. Feng, J. Dai, Z. Xu, and G. Cao, "Superconductivity up to 30 K in the vicinity of the quantum critical point in $BaFe_2(As_{1-x}P_x)_2$," *Journal of Physics: Condensed Matter*, vol. 21, p. 382203, 2009

[23] A. Leithe-Jasper, W. Schnelle, C. Geibel, and H. Rosner, "Superconducting State in $SrFe_{2-x}Co_xAs_2$ by Internal Doping of the Iron Arsenide Layers," *Physical Review Letters*, vol. 101, p. 207004, 2008.

[24] F. Han, X. Zhu, P. Cheng, G. Mu, Y. Jia, L. Fang, Y. Wang, H. Luo, B. Zeng, B. Shen, L. Shan, C. Ren, and H.-H. Wen, "Superconductivity and phase diagrams of the 4*d*- and 5*d*-metal-doped iron arsenides $SrFe_{2-x}M_xAs_2$ (M = Rh, Ir, Pd)," *Physical Review B*, vol. 80, p. 024506, 2009.

[25] C. G. Shull and J. S. Smart, "Detection of Antiferromagnetism by Neutron Diffraction," *Physical Review*, vol. 76, p. 1256, 1949.

[26] C. G. Shull, E. O. Wollan, and W. A. Strauser, "Magnetic Structure of Magnetite and Its Use in Studying the Neutron Magnetic Interaction," *Physical Review*, vol. 81, p. 483, 1951.

[27] C. G. Shull, W. A. Strauser, and E. O. Wollan, "Neutron Diffraction by Paramagnetic and Antiferromagnetic Substances," *Physical Review*, vol. 83, p. 333-345, 1951.

[28] J. Zhao, W. Ratcliff, J. W. Lynn, J. Hu, and P. Dai, "Spin and lattice structures of single-crystalline $SrFe_2As_2$," *Physical Review B*, vol. 78, p. 140504, 2008.

[29] W. Ratcliff, P. A. Kienzle, J. W. Lynn, S. Li, P. Dai, G. F. Chen, and N. L. Wang, "Magnetic form factor of $SrFe_2As_2$: Neutron diffraction measurements," *Physical Review B*, vol. 81, p. 140502, 2010.

[30] I. I. Mazin and J. Schmalian, "Pairing symmetry and pairing state in ferropnictides: Theoretical overview," *Physica C: Superconductivity*, vol. 469, p. 614-627, 2009.

[31] H. Ding, P. Richard, K. Nakayama, K. Sugawara, T. Arakane, Y. Sekiba, A. Takayama, S. Souma, T. Sato, T. Takahashi, Z. Wang, X. Dai, Z. Fang, G. F. Chen, J. L. Luo, and N. L. Wang, "Observation of Fermi-surface-dependent nodeless superconducting gaps in $Ba_{0.6}K_{0.4}Fe_2As_2$," *Europhysics Letters*, vol. 83, p. 47001, 2008.

[32] C. Liu, T. Kondo, R. M. Fernandes, A. D. Palczewski, E. D. Mun, N. Ni, A. N. Thaler, A. Bostwick, E. Rotenberg, J. Schmalian, S. L. Bud'ko, P. C. Canfield,

and A. Kaminski, "Evidence for a Lifshitz transition in electron-doped iron arsenic superconductors at the onset of superconductivity," *Nature Physics*, vol. 6, p. 419-423, 2010.

[33] D. V. Evtushinsky, D. S. Inosov, V. B. Zabolotnyy, A. Koitzsch, M. Knupfer, B. Buchner, M. S. Viazovska, G. L. Sun, V. Hinkov, A. V. Boris, C. T. Lin, B. Keimer, A. Varykhalov, A. A. Kordyuk, and S. V. Borisenko, "Momentum dependence of the superconducting gap in $Ba_{1-x}K_xFe_2As_2$," *Physical Review B*, vol. 79, p. 054517, 2009.

[34] M. Yi, D. H. Lu, J. G. Analytis, J.-H. Chu, S.-K. Mo, R.-H. He, M. Hashimoto, R. G. Moore, I. I. Mazin, D. J. Singh, Z. Hussain, I. R. Fisher, and Z.-X. Shen, "Unconventional electronic reconstruction in undoped (Ba, Sr)Fe_2As_2 across the spin density wave transition," *Physical Review B*, vol. 80, p. 174510, 2009.

[35] L. Boeri, M. Calandra, I. I. Mazin, O. V. Dolgov, and F. Mauri, "Effects of magnetism and doping on the electron-phonon coupling in $BaFe_2As_2$," *Physical Review B*, vol. 82, p. 020506, 2010.

[36] R. H. Liu, T. Wu, G. Wu, H. Chen, X. F. Wang, Y. L. Xie, J. J. Ying, Y. J. Yan, Q. J. Li, B. C. Shi, W. S. Chu, Z. Y. Wu, and X. H. Chen, "A large iron isotope effect in $SmFeAsO_{1-x}F_x$ and $Ba_{1-x}K_xFe_2As_2$," *Nature*, vol. 459, p. 64-67, 2009.

[37] H. Wadati, I. Elfimov, and G. A. Sawatzky, "Where Are the Extra d Electrons in Transition-Metal-Substituted Iron Pnictides?," *Physical Review Letters*, vol. 105, p. 157004, 2010.

[38] C.-H. Lee, A. Iyo, H. Eisaki, H. Kito, M. T. Fernandez-Diaz, T. Ito, K. Kihou, H. Matsuhata, M. Braden, and K. Yamada, "Effect of Structural Parameters on Superconductivity in Fluorine-Free $LnFeAsO_{1-y}$ (Ln = La, Nd)," *Journal of the Physical Society of Japan*, vol. 77, p. 083704, 2008.

[39] K. Kuroki, H. Usui, S. Onari, R. Arita, H. Aoki, "Pnictogen height as a possible switch between high-T_c nodeless and low-T_c nodal pairings in the iron-based superconductors," *Physical Review B*, vol. 79, p. 224511, 2009.

[40] G. E. Blonder, M. Tinkham, and T. M. Klapwijk, "Transition from metallic to tunneling regimes in superconducting microconstrictions: Excess current, charge imbalance, and supercurrent conversion," *Physical Review B*, vol. 25, p. 4515, 1982.

[41] D. Daghero, M. Tortello, G. A. Ummarino, and R. S. Gonnelli, "Directional point-contact Andreev-reflection spectroscopy of Fe-based superconduc-

tors: Fermi surface topology, gap symmetry, and electron-boson interaction," *Reports on Progress in Physics*, vol. 74, p. 124509, 2011.

[42] P. Samuely, Z. Pribulova, P. Szabo, G. Pristas, S. L. Bud'ko, and P. C. Canfield, "Point contact Andreev reflection spectroscopy of superconducting energy gaps in 122-type family of iron pnictides," *Physica C*, vol. 469, p. 507-511, 2009.

[43] P. Szabo, Z. Pribulova, G. Pristas, S. L. Bud'ko, P. C. Canfield, and P. Samuely, "Evidence for two-gap superconductivity in $Ba_{0.55}K_{0.45}Fe_2As_2$ from directional point-contact Andreev-reflection spectroscopy," *Physical Review B*, vol. 79, p. 012503, 2009.

[44] C. Ren, Z.-S. Wang, Z.-Y. Wang, H.-Q. Luo, X.-Y. Lu, B. Sheng, C.-H. Li, L. Shan, H. Yang, and H.-H. Wen, "Gap Anisotropy in Iron-Based Superconductors: A Point-Contact Andreev Reflection Study of $BaFe_{2-x}Ni_xAs_2$ Single Crystals, *Physical Review B*, vol. 86, p. 060508, 2012.

[45] L. Taillefer, B. Lussier, R. Gagnon, K. Behnia, and H. Aubin, "Universal Heat Conduction in $YBa_2Cu_3O_{6.9}$," *Physical Review Letters*, vol. 79, p. 483, 1997.

[46] C. Proust, E. Boaknin, R. W. Hill, L. Taillefer, and A. P. Mackenzie, "Heat Transport in a Strongly Overdoped Cuprate: Fermi Liquid and a Pure *d*-Wave BCS Superconductor," *Physical Review Letters*, vol. 89, p. 147003, 2002.

[47] J.-Ph. Reid, M. A. Tanatar, X. G. Luo, H. Shakeripour, N. Doiron-Leyraud, N. Ni, S. L. Bud'ko, P. C. Canfield, R. Prozorov, and L. Taillefer, "Nodes in the gap structure of the iron arsenide superconductor $Ba(Fe_{1-x}Co_x)_2As_2$ from *c*-axis heat transport measurements," *Physical Review B*, vol. 82, p. 064501, 2010.

[48] J.-Ph. Reid, M. A. Tanatar, A. Juneau-Fecteau, R. T. Gordon, S. René de Cotret, N. Doiron-Leyraud, T. Saito, H. Fukuzawa, Y. Kohori, K. Kihou, C. H. Lee, A. Iyo, H. Eisaki, R. Prozorov, and L. Taillefer, "Universal Heat Conduction in the Iron Arsenide Superconductor KFe_2As_2: Evidence of a *d*-Wave State," *Physical Review Letters*, vol. 109, p. 087001, 2012.

[49] M. A. Tanatar, J.-Ph. Reid, S. René de Cotret, N. Doiron-Leyraud, F. Laliberté, E. Hassinger, J. Chang, H. Kim, K. Cho, Y. J. Song, Y. S. Kwon, R. Prozorov, and L. Taillefer, "Isotropic three-dimensional gap in the iron arsenide superconductor LiFeAs from directional heat transport measurements," *Physical Review B*, vol. 84, p. 054507, 2011.

[50] E. Boaknin, M. A. Tanatar, J. Paglione, D. Hawthorn, F. Ronning, R. W. Hill, M. Sutherland, L. Taillefer, J. Sonier, S. M. Hayden, and J. W. Brill, "Heat

Conduction in the Vortex State of $NbSe_2$: Evidence for Multiband Superconductivity," *Physical Review Letters*, vol. 90, p. 117003, 2003.

[51] K. Terashima, Y. Sekiba, J. H. Bowen, K. Nakayama, T. Sato, P. Richard, Y.-M. Xu, L. J. Li, G. H. Cao, Z.-A. Xu, H. Ding, and T. Takahashi, "Fermi surface nesting induced strong pairing in iron-based superconductors," *Proceedings of the National Academy of Sciences of the United States of America*, vol. 106, p. 7330-7333, 2009.

[52] H.Z. Arham and L.H. Greene, "Point contact spectroscopy of Fe pnictides and chalcogenides in the normal state," *Current Opinion in Solid State and Materials Science*, vol. 17, p. 81-88, 2013.

[53] B. Muschler, W. Prestel, R. Hackl, T. P. Devereaux, J. G. Analytis, J.-H. Chu, and I. R. Fisher, "Band- and momentum-dependent electron dynamics in superconducting $Ba(Fe_{1-x}Co_x)_2As_2$ as seen via electronic Raman scattering," *Physical Review B*, vol. 80, p. 180510, 2009.

[54] S. Chadov, X. Qi, J. Kübler, G. H. Fecher, C. Felser, and S. C. Zhang, "Tunable multifunctional topological insulators in ternary Heusler compounds," *Nature Materials*, vol. 9, p. 541-545, 2010.

[55] *Condensed Matter Theory and Simulation Group*, Universidad Autonoma de Madrid, http://www.uam.es/gruposinv/cmpts03/topological.html, 2014.

[56] L. Fu and C. L. Kane, "Superconducting Proximity Effect and Majorana Fermions at the Surface of a Topological Insulator," *Physical Review Letters*, vol. 100, p. 096407, 2008.

[57] K. V. Samokhin, "Spin-orbit coupling and semiclassical electron dynamics in noncentrosymmetric metals," *Annals of Physics*, vol. 324, p. 2385-2407, 2009.

[58] S. Yip, "Noncentrosymmetric Superconductors," *Annual Review of Condensed Matter Physics*, vol. 5, p. 15-33, 2014.

[59] P. A. Frigeri, D. F. Agterberg, I. Milat, and M. Sigrist, "Phenomenological theory of the s-wave state in superconductors without an inversion center," *European Physical Journal B*, vol. 54, p. 435-448, 2006.

[60] M. Sato, "Topological odd-parity superconductors," *Physical Review B*, vol. 81, p. 220504, 2010.

[61] A. P. Schnyder, S. Ryu, A. Furusaki, and A. W. W. Ludwig, "Classification of topological insulators and superconductors in three spatial dimensions," *Physical Review B*, vol. 78, p. 195125, 2008.

[62] X.-L. Qi and S.-C. Zhang, "Topological insulators and superconductors," *Reviews of Modern Physics*, vol. 83, p. 1057, 2011.

[63] K. V. Samokhin and V. P. Mineev, "Gap structure in noncentrosymmetric superconductors," *Physical Review B*, vol. 77, p. 104520, 2008.

[64] E. Bauer, G. Hilscher, H. Michor, C. Paul, E. W. Scheidt, A. Gribanov, Y. Seropegin, H. Noël, M. Sigrist, and P. Rogl, "Heavy Fermion Superconductivity and Magnetic Order in Noncentrosymmetric $CePt_3Si$," *Physical Review Letters*, vol. 92, p. 027003, 2004.

[65] T. Akazawa, H. Hidaka, T. Fujiwara, T. C. Kobayashi, E. Yamamoto, Y. Haga, R. Settai, and Y. Onuki, "Pressure-induced superconductivity in ferromagnetic UIr without inversion symmetry," *Journal of Physics: Condensed Matter*, vol. 16, p. L29, 2004.

[66] N. Kimura, K. Ito, K. Saitoh, Y. Umeda, H. Aoki, and T. Terashima, "Pressure-Induced Superconductivity in Noncentrosymmetric Heavy-Fermion $CeRhSi_3$," *Physical Review Letters*, vol. 95, p. 247004, 2005.

[67] I. Sugitani, Y. Okuda, H. Shishido, T. Yamada, A. Thamizhavel, E. Yamamoto, T. D. Matsuda, Y. Haga, T. Takeuchi, R. Settai, and Y. Onuki, "Pressure-Induced Heavy-Fermion Superconductivity in Antiferromagnet $CeIrSi_3$," *Journal of the Physical Society of Japan*, vol. 75, p. 043703, 2006.

[68] G. Amano, S. Akutagawa, T. Muranaka, Y. Zenitani, and J. Akimitsu, "Superconductivity at 18 K in Yttrium Sesquicarbide System, Y_2C_3," *Journal of the Physical Society of Japan*, vol. 73, p. 530-532, 2004.

[69] K. Togano, P. Badica, Y. Nakamori, S. Orimo, H. Takeya, and K. Hirata, "Superconductivity in the Metal Rich Li-Pd-B Ternary Boride," *Physical Review Letters*, vol. 93, p. 247004, 2004.

[70] G. Schuck, S. M. Kazakov, K. Rogacki, N. D. Zhigadlo, and J. Karpinski, "Crystal growth, structure, and superconducting properties of the β-pyrochlore KOs_2O_6," *Physical Review B*, vol. 73, p. 144506, 2006.

[71] A. P. Mackenzie and Y. Maeno, "The superconductivity of Sr_2RuO_4 and the physics of spin-triplet pairing," *Reviews of Modern Physics*, vol. 75, p. 657-712, 2003.

[72] X. Zhang, N. P. Butch, P. Syers, S. Ziemak, R. L. Greene, and J. Paglione, "Hybridization, Inter-Ion Correlation, and Surface States in the Kondo Insulator SmB_6," *Physical Review X*, vol. 3, p. 011011, 2013.

[73] D. J. Kim, S. Thomas, T. Grant, J. Botimer, Z. Fisk, and J. Xia, "Surface Hall Effect and Nonlocal Transport in SmB_6: Evidence for Surface Conduction," *Scientific Reports*, vol. 3, p. 3150, 2013.

[74] S. Wolgast, C. Kurdak, K. Sun, J. W. Allen, D.-J. Kim, and Z. Fisk, "Low-temperature surface conduction in the Kondo insulator SmB_6.", *Physical Review B*, vol. 88, p. 180405, 2013.

[75] M. König, S. Wiedmann, C. Brüne, A. Roth, H. Buhmann, L. Molenkamp, X.-L. Qi, and S.-C. Zhang, "Quantum Spin Hall Insulator State in HgTe Quantum Wells," *Science*, vol. 318, p. 766-770, 2007.

[76] T. Sato, Y. Tanaka, K. Nakayama, S. Souma, T. Takahashi, S. Sasaki, Z. Ren, A. A. Taskin, K. Segawa, and Y. Ando, "Fermiology of Strongly Spin-Orbit Coupled Superconductor $Sn_{1-x}In_xTe$ and its Implication to Topological Superconductivity," *Physical Review Letters*, vol. 110, p. 206804, 2013.

[77] A. Hirohata, M. Kikuchi, N. Tezuka, K. Inomata, J.S. Claydon, Y.B. Xu, G. van der Laan, "Heusler alloy/semiconductor hybrid structures," *Current Opinion in Solid State and Materials Science*, vol. 10, p. 93-107, 2006.

[78] N. W. Ashcroft and N. D. Mermin, *Solid State Physics*, Brooks/Cole, 1976.

[79] F. F. Tafti, T. Fujii, A. Juneau-Fecteau, S. René de Cotret, N. Doiron-Leyraud, A. Asamitsu, and L. Taillefer, "Superconductivity in the noncentrosymmetric half-Heusler compound LuPtBi: A candidate for topological superconductivity," *Physical Review B*, vol. 87, p. 184504, 2013.

[80] P. C. Canfield, J. D. Thompson, W. P. Beyermann, A. Lacerda, M. F. Hundley, E. Peterson, Z. Fisk, and H. R. Ott, "Magnetism and heavy fermion-like behavior in the RBiPt series," *Journal of Applied Physics*, vol. 70, p. 5800, 1991.

[81] N. P. Butch, P. Syers, K. Kirshenbaum, A. P. Hope, and J. Paglione, "Superconductivity in the topological semimetal YPtBi," *Physical Review B*, vol. 84, p. 220504, 2011.

[82] T. V. Bay, T. Naka, Y. K. Huang, and A. de Visser, "Superconductivity in noncentrosymmetric YPtBi under pressure," *Physical Review B*, vol. 86, p. 064515, 2012.

[83] T. V. Bay, M. Jackson, C. Paulsen, C. Baines, A. Amato, T. Orvis, M. C. Aronson, Y. K. Huang, and A. de Visser, "Low field magnetic response of the non-centrosymmetric superconductor YPtBi," *Solid State Communications*, vol. 183, p. 13-17, 2014.

[84] C. Shi, X. Xi, Z. Hou, X. Zhang, G. Xu, E. Liu, W. Wang, W. Wang, and G. Wu, "NMR evidence for enhanced orbital diamagnetism in topological nontrivial half-Heusler semimetals," arxiv.org/pdf/1408.0078, 2014.

[85] K. Gofryk, D. Kaczorowski, T. Plackowski, A. Leithe-Jasper, and Y. Grin, "Magnetic and transport properties of rare-earth-based half-Heusler phases *R*PdBi: Prospective systems for topological quantum phenomena," *Physical Review B*, vol. 84, p. 035208, 2011.

[86] H. Lin, L. A. Wray, Y. Xia, S. Xu, S. Jia, R. J. Cava, A. Bansil, M. Z. Hasan, "Half-Heusler ternary compounds as new multifunctional experimental platforms for topological quantum phenomena," *Nature Materials*, vol. 9, p. 546-549, 2010.

[87] W. Al-Sawai, H. Lin, R. S. Markiewicz, L. A. Wray, Y. Xia, S.-Y. Xu, M. Z. Hasan, and A. Bansil, "Topological electronic structure in half-Heusler topological insulators," *Physical Review B*, vol. 82, 125208, 2010.

[88] X. T. Wang, X. F. Dai, H. Y. Jia, L. Y. Wang, X. F. Liu, Y. T. Cui, and G. D. Liu, "Topological insulating characteristic in half-Heuslser compounds composed of light elements," *Physics Letters A*, vol. 378, p. 1662-1666, 2014.

[89] C. Honerkamp and M. Sigrist, "Andreev Reflection in Unitary and Non-Unitary Triplet States," *Journal of Low Temperature Physics*, vol. 111, p. 895-915, 1998.

[90] F. Laube, G. Goll, H. v. Löhneysen, M. Fogelström, and F. Lichtenberg, "Spin-Triplet Superconductivity in Sr_2RuO_4 Probed by Andreev Reflection," *Physical Review Letters*, vol. 84, p. 1595-1598, 2000.

[91] S. Sasaki, M. Kriener, K. Segawa, K. Yada, Y. Tanaka, M. Sato, and Y. Ando, "Topological Superconductivity in $Cu_xBi_2Se_3$," *Physical Review Letters*, vol. 107, p. 217001, 2011.

[92] S. Sasaki, Z. Ren, A. A. Taskin, K. Segawa, L. Fu, and Y. Ando, "Odd-Parity Pairing and Topological Superconductivity in a Strongly Spin-Orbit Coupled Semiconductor," *Physical Review Letters*, vol. 109, p. 217004, 2012.

[93] N. Levy, T. Zhang, J. Ha, F. Sharifi, A. A. Talin, Y. Kuk, and J. A. Stroscio, "Local Measurements of the Superconducting Pairing Symmetry in $Cu_xBi_2Se_3$," *Physical Review Letters*, vol. 110, p. 117001, 2013.

[94] K. Ishida, H. Mukuda, Y. Kitaoka, K. Asayama, Z. Q. Mao, Y. Mori, and Y. Maeno, "Spin-triplet superconductivity in Sr_2RuO_4 identified by ^{17}O Knight shift," *Nature*, vol. 396, p. 658-660, 1998.

[95] W. N. Hardy, D. A. Bonn, D. C. Morgan, R. Liang, and K. Zhang, "Precision measurements of the temperature dependence of λ in $YBa_2Cu_3O_{6.95}$: Strong evidence for nodes in the gap function," *Physical Review Letters*, vol. 70, p. 3999-4002, 1993.

[96] I. Bonalde, B. D. Yanoff, M. B. Salamon, D. J. Van Harlingen, E. M. E. Chia, Z. Q. Mao, and Y. Maeno, "Temperature Dependence of the Penetration Depth in Sr_2RuO_4: Evidence for Nodes in the Gap Function," *Physical Review Letters*, vol. 85, p. 4775-4778, 2000.

[97] G. M. Luke, Y. Fudamoto, K. M. Kojima, M. I. Larkin, J. Merrin, B. Nachumi, Y. J. Uemura, Y. Maeno, Z. Q. Mao, Y. Mori, H. Nakamura, and M. Sigrist, "Time-reversal symmetry-breaking superconductivity in Sr_2RuO_4," *Nature*, vol. 394, p. 558-561, 1998.

[98] X. F. Wang, T. Wu, G. Wu, H. Chen, Y. L. Xie, J. J. Ying, Y. J. Yan, R. H. Liu, and X. H. Chen, "Anisotropy in the Electrical Resistivity and Susceptibility of Superconducting $BaFe_2As_2$ Single Crystals," *Physical Review Letters*, vol. 102, p. 117005, 2009.

[99] B. S. Deaver and W. M. Fairbank, "Experimental Evidence for Quantized Flux in Superconducting Cylinders," *Physical Review Letters*, vol. 7, p. 43, 1961.

[100] R. Doll and M. Näbauer, "Experimental Proof of Magnetic Flux Quantization in a Superconducting Ring," *Physical Review Letters*, vol. 7, p. 51, 1961.

[101] D. Daghero and R. S. Gonnelli, "Probing multiband superconductivity by point-contact spectroscopy," *Superconducting Science and Technology*, vol. 23, p. 043001, 2010.

[102] K. A. Yates, L. F. Cohen, Z.-A. Ren, J. Yang, W. Lu, X.-L. Dong, and Z.-X. Zhao, "Point contact Andreev reflection spectroscopy of $NdFeAsO_{0.85}$," *Superconductor Science and Technology*, vol. 21, p. 092003, 2008.

[103] S. R. Saha, N. P. Butch, K. Kirshenbaum, J. Paglione, and P. Y. Zavalij, "Superconducting and Ferromagnetic Phases Induced by Lattice Distortions in Stoichiometric $SrFe_2As_2$ Single Crystals," *Physical Review Letters*, vol. 103, p. 037005, 2009.

[104] K. Kirshenbaum, S. R. Saha, T. Drye, and J. Paglione, "Superconductivity and magnetism in platinum-substituted $SrFe_2As_2$ single crystals," *Physical Review B*, vol. 82, p. 144518, 2010.

[105] N. P. Butch, S. R. Saha, X. H. Zhang, K. Kirshenbaum, R. L. Greene, and J. Paglione, "Effective carrier type and field dependence of the reduced-T_c superconducting state in $SrFe_{2-x}Ni_xAs_2$," *Physical Review B*, vol. 81, p. 024518, 2010.

[106] Features in the conductance spectra associated with the onset of superconductivity in sample S2 appear to emerge only below 18 K, which is lower than the nominal T_c value of 23 K measured by resistivity, susceptibility and heat capacity (Ref. [14]). This may be due to critical current effects or possibly a departure from the diffusive Sharvin regime at higher temperatures. [109]

[107] Y. G. Naidyuk, I. K. Yanson, L. V. Tyutrina, N. L. Bobrov, P. N. Chubov, W. N. Kang, H.-J. Kim, E.-M. Choi, and S.-I. Lee, "Superconducting Energy Gap Distribution in c-Axis Oriented MgB_2 Thin Film from Point Contact Study," *JETP Letters*, vol. 75, p. 238-241, 2002.

[108] K. Kirshenbaum, S. R. Saha, S. Ziemak, T. Drye, and J. Paglione, "Universal pair-breaking in transition-metal-substituted iron-pnictide superconductors," *Physical Review B*, vol. 86, p. 140505, 2012.

[109] G. Sheet, S. Mukhopadhyay, and P. Raychaudhuri, "Role of critical current on the point-contact Andreev reflection spectra between a normal metal and a superconductor," *Physical Review B*, vol. 69, p. 134507, 2004.

[110] X. Lu, W. K. Park, H. Q. Yuan, G. F. Chen, G. L. Luo, N. L. Wang, A. S. Sefat, M. A. McGuire, R. Jin, B. C. Sales, D. Mandrus, J. Gillett, S. E. Sebastian, and L. H. Greene, "Point-contact spectroscopic studies on normal and superconducting AFe_2As_2-type iron-pnictide single crystals," *Superconductor Science and Technology*, vol. 23, p. 054009, 2010.

[111] X. Zhang, Y. S. Oh, Y. Liu, L. Yan, S. R. Saha, N. P. Butch, K. Kirshenbaum, K. H. Kim, J. Paglione, R. L. Greene, and I. Takeuchi, "Evidence of a universal and isotropic $2\Delta/k_BT_C$ ratio in 122-type iron pnictide superconductors over a wide doping range," *Physical Review B*, vol. 82, p. 020515, 2010.

[112] X. Zhang, B. Lee, S. Khim, K. H. Kim, R. L. Greene, and I. Takeuchi, "Probing the order parameter of superconducting LiFeAs using Pb/LiFeAs and Au/LiFeAs point-contact spectroscopy," *Physical Review B*, vol. 85, p. 094521, 2012.

[113] K. Umezawa, Y. Li, H. Miao, K. Nakayama, Z.-H. Liu, P. Richard, T. Sato, J. B. He, D.-M. Wang, G. F. Chen, H. Ding, T. Takahashi, and S.-C. Wang, "Unconventional Anisotropic *s*-Wave Superconducting Gaps of the LiFeAs Iron-Pnictide Superconductor," *Physical Review Letters*, vol. 108, p. 037002, 2012.

[114] M. P. Allan, A. W. Rost, A. P. Mackenzie, Y. Xie, J. C. Davis, K. Kihou, C. H. Lee, A. Iyo, H. Eisaki, and T.-M. Chuang, "Anisotropic Energy Gaps of Iron-based Superconductivity fron Intra-band Quasiparticle Interference in LiFeAs," *Science*, vol. 336, p. 563, 2012.

[115] J. E. Hoffman, "Spectroscopic scanning tunneling microscopy insights into Fe-based superconductors," *Reports on Progress in Physics*, vol. 74, p. 124513, 2011.

[116] Y. Yin, M. Zech, T. L. Williams, X. F. Wang, G. Wu, X. H. Chen, and J. E. Hoffman, "Scanning Tunneling Spectroscopy and Vortex Imaging in the Iron Pnictide Superconductor $BaFe_{1.8}Co_{0.2}As_2$," *Physical Review Letters*, vol. 102, p. 097002, 2009.

[117] J. Lowell and J. B. Sousa, "Mixed-state thermal conductivity of type II superconductors," *Journal of Low Temperature Physics*, vol. 3, p. 65-87, 1970.

[118] J.-Ph. Reid, A. Juneau-Fecteau, R. T. Gordon, S. René de Cotret, N. Doiron-Leyraud, X. G. Luo, H. Shakeripour, J. Chang, M. A. Tanatar, H. Kim, R. Prozorov, T. Saito, H. Fukuzawa, Y. Kohori, K. Kihou, C. H. Lee, A. Iyo, H. Eisaki, B. Shen, H.-H. Wen, and L. Taillefer, "From d-wave to s-wave pairing in the iron-pnictide superconductor $(Ba,K)Fe_2As_2$," *Superconductor Science and Technology*, vol. 25, p. 084013, 2012.

[119] S. V. Borisenko, V. B. Zabolotnyy, D. V. Evtushinsky, T. K. Kim, I. V. Morozov, A. N. Yaresko, A. A. Kordyuk, G. Behr, A. Vasiliev, R. Follath, and B. Büchner, "Superconductivity without Nesting in LiFeAs," *Physical Review Letters*, vol. 105, p. 067002, 2010.

[120] P. Richard, T. Sato, K. Nakayama, T. Takahashi, and H. Ding, "Fe-based superconductors: an angle-resolved photoemission spectroscopy perspective," *Reports on Progress in Physics*, vol. 74, p. 124512, 2011.

[121] K. Nakayama, T. Sato, P. Richard, Y.-M. Xu, T. Kawahara, K. Umezawa, T. Qian, M. Neupane, G. F. Chen, H. Ding, and T. Takahashi, "Universality of superconducting gaps in overdoped $Ba_{0.3}K_{0.7}Fe_2As_2$ observed by angle-resolved photoemission spectroscopy," *Physical Review B*, vol. 83, p. 020501, 2011; K. Nakayama, T. Sato, P. Richard, Y.-M. Xu, Y. Seikaba, S. Souma, G. F. Chen, J. L. Luo, N. L. Wang, H. Ding, and T. Takahashi, "Superconducting gap symme-

try of $Ba_{0.6}K_{0.4}Fe_2As_2$ studied by angle-resolved photoemission spectroscopy," *Europhysics Letters*, vol. 85. p. 67002, 2009.

[122] L. Chauvière, Y. Gallais, M. Cazayous, M. A. Méasson, A. Sacuto, D. Colson, A. Forget, "Impact of the spin-density-wave order on the superconducting gap of $Ba(Fe_{1-x}Co_x)_2As_2$," *Physical Review B*, vol. 82, p. 180521, 2010.

[123] S. Sugai, Y. Mizuno, K. Kiho, M. Nakajima, C. H. Lee, A. Iyo, H. Eisaki, and S. Uchida, "Pairing symmetry of the multiorbital pnictide superconductor $BaFe_{1.84}Co_{0.16}As_2$ from Raman scattering," *Physical Review B*, vol. 82, p. 140504, 2010.

[124] S. Nadj-Perge, I. K. Drozdov, J. Li, H. Chen, S. Jeon, J. Seo, A. H. MacDonald, B. A. Bernevig, and A. Yazdani, "Observation of Majorana fermions in ferromagnetic atomic chains on a superconductor," *Science* vol. 346, p. 602-607, 2014.